

Universidade de São Paulo
Instituto de Astronomia, Geofísica e Ciências Atmosféricas
Departamento de Ciências Atmosféricas

Danilo Couto de Souza

Cyclones in Southwestern Atlantic: Life Cycle and Energetics

São Paulo

2024

Danilo Couto de Souza

Cyclones in Southwestern Atlantic: Life Cycle and Energetics

Tese apresentada ao Programa de Meteorologia do Instituto de Astronomia, Geofísica e Ciências Atmosféricas da Universidade de São Paulo como requisito parcial para a obtenção do título de Doutor em Ciências.

Área de Concentração: Meteorologia

Orientador: Prof. Dr. Pedro Leite da Silva
Dias

Coorientador: Prof. Dr. Ricardo de Camargo

São Paulo

2024

O que há de melhor tá na vida, na transformação da natureza.

Acknowledgements

- Mulher;
- Família;
- Orientadores Pedro Dias e Ricardo de Camargo
- Ex-orientadores: Renato Ramos da Silva, Roberto Carelli Fontes e John Beardall;
- Pesquisadores e professores: Carolina Gramcianinov, Pedro Peixoto, Felipe Bragança Alves;
- Colegas: Matheus Bonjour, Renan Godoy, Maria Luiza Kovalski, e toda equipe do MASTER;
- Suporte técnico: Jean Peres, Djalma, Sebastião e Samuca;
- LNCC: rodadas com SDumont;
- Alexandra Elbakyan, Aaron Swartz e toda comunidade *open source*

“一、努力の精神を養うこと”

“First, foster the spirit of effort”

“Primeiro, criar o intuito do esforço”

Kanga Sakukawa

Resumo

Resumo

Abstract

Abstract

List of Figures

2.1	Air masses	27
2.2	Phase Diagram - Hart	29
2.3	Bjerknes Cyclone Model	30
2.4	Bjerknes' and Shapiro-Keyser's Cyclonic Models	32
2.5	Tropical Cyclone - Cross Section	34
2.6	Phase Diagram - Hart	35
2.7	Extratropical Cyclone - Cross Section	37
2.8	Model of development of cyclones types A and B.	40
2.9	Comparison - CISK vs. WISHE	42
2.10	Conceptual Model: Instabilities and Types of Cyclones	47
2.11	Global Circulation	49
2.12	Tropical Cyclone as a Carnot Cycle	50
2.13	Cyclogenesis regions in the South Atlantic	54
2.14	Extratropical Cyclone Life Cycle	62
2.15	Effects of Heating and Cooling on Potential Energy	64
2.16	Available Potential Energy	65
2.17	Energy Cycle - Lorenz	67
2.18	Energy Cycle - Muench	68
2.19	Energy Cycle - Brennan	70
2.20	Energy Cycle - Michaelides	72
2.21	Eulerian LEC - Issues	73
2.22	LEC - discussion	75
2.23	C_Z - representation	80

2.24	C_A - representation	81
2.25	Zonal and meridional jets	82
2.26	Meridional jet - eddy	83
2.27	LEC - chains	89
3.1	Cyclophaser - logo	101
3.2	Cyclophaser - methodological steps	102
3.3	Residual stage - study case	106
3.4	Impact of Varying Threshold Values for Intensification Phase	108
3.5	Impact of Varying Threshold Values for Decay Phase	108
3.6	Variations in Threshold Values for Mature Phase	109
3.7	Impact of Varying Threshold Values for Incipient Phase	109
4.1	Cyclogenesis Climatology in the SESA Region	115
4.2	Life Cycle Configurations	116
4.3	Filtered Life Cycle Configurations	117
4.4	Cyclone Life Cycles - Representative Examples	117
4.5	Life cycle configurations by regions and season	118
4.6	PDF - Metrics for Each Region and Season	119
4.7	PDF - Total Time	122
4.8	PDF - Total Distance	123
4.9	PDF - Mean Speed	124
4.10	PDF - Mean Vorticity	125
4.11	PDF - Mean Growth Rate	127
4.12	Mature Phase - Center of Mass	127
4.13	Track Density - Incipient Phase	129
4.14	Track Density - Intensification Phase	131
4.15	Track Density - Mature Phase	133
4.16	Track Density - Decay Phase	135
4.17	Track Density - Secondary Development Stages	137
4.18	Track Density - Intensification 2	139
4.19	Track Density - Mature 2	140
4.20	Track Density - Decay 2	141

4.21	Track Density - Residual Phase	143
4.22	Illustrative Representation of Cyclone Life Cycle	146
5.1	Box plots - Complete Lifecycle	151
5.2	Density Plots - Energy Terms	152
5.3	Density Plots - Conversion Terms	155
5.4	Density Plots - Boundary Terms	156
5.5	Density Plots - Generation Terms	158
5.6	Density Plots - Budget Terms	159
5.7	EOF Analysis - Total Lifecycle	161

List of Tables

5.1 Summary Statistics of Lorenz Energetics Components	153
--	-----

Contents

1. <i>Introduction</i>	23
1.1 Objetivo e pergunta de pesquisa	23
1.2 Objetivos específicos	23
2. <i>Theoretical Background</i>	25
2.1 Cyclones: Categories and Definitions	25
2.1.1 Material Causes	26
2.1.2 Formal Causes	30
2.1.3 Efficient Causes	35
2.1.4 Final Causes	47
2.1.5 Summary	51
2.2 Cyclones in South America	52
2.2.1 Climatological aspects	53
2.2.2 Genesis mechanisms	54
2.2.3 Subtropical cyclones	56
2.2.4 Tropical cyclones	57
2.3 Life cycle of extratropical cyclones: objective classification procedures	59
2.4 Atmosphere Energetics	63
2.4.1 Lorenz Energy Cycle: Historical Background	63
2.4.2 Lorenz Energy Cycle: Mathematical expressions and physical interpretation	76
2.4.3 Lorenz Energy Cycle applied to cyclonic systems	89

3.	<i>Data & Methods</i>	99
3.1	Fluxograma de atividades	99
3.2	Databases	99
3.2.1	Cyclone tracks in the South Atlantic	99
3.3	Cyclone's Life Cycle Detection	100
3.3.1	Cyclophaser program description	100
3.3.2	Cyclophaser settings	107
3.4	Cálculo do ciclo energético	110
3.5	Determinação dos padrões energéticos	110
3.6	Descrição do MPAS-A	110
3.7	Desenho experimental das simulações	110
3.7.1	Testes de sensibilidade: Furacão Catarina	110
3.7.2	Experimentos com SST	111
4.	<i>Life Cycle of Cyclones in the Southwestern Atlantic</i>	113
4.1	Climatology and Statistics	113
4.1.1	Climatological Aspects and Life Cycle Configurations	114
4.1.2	Mean Cyclone Statistics	116
4.1.3	Life Cycle Phase Statistics	121
4.2	Spatial Distribution of Cyclone Life Cycle Phases	128
4.2.1	Incipient Phase	128
4.2.2	Intensification Phase	130
4.2.3	Mature Phase	132
4.2.4	Decay Phase	134
4.2.5	Secondary Development Phases	136
4.2.6	Residual Phase	142
4.3	Summary and Concluding Remarks	144
5.	<i>Southwestern Atlantic Cyclones Energetics</i>	149
5.1	LEC Climatology	150
5.1.1	Descriptive Statistics: Complete Life Cycle	150
5.1.2	EOFs	159

6. Modelagem numérica	163
6.1 Testes de sensibilidade: estudo de caso com Furacão Catarina	163
6.1.1 Comparação da pressão mínima em superfície e posição do sistema	163
6.1.2 Precipitação acumulada	163
6.1.3 Ventos em superfície	163
6.1.4 Energética	163
6.2 Experimentos com perturbações no campo de SST	163
6.2.1 Interação oceano-atmosfera	163
6.2.2 Ciclo energético	163
7. Conclusões	165
<i>Bibliography</i>	167
<i>Appendix</i>	185
A. <i>título do apêndice 01</i>	187
A.1 <i>subtítulo 01</i>	187
B. <i>título do apêndice 02</i>	189

Chapter 1

Introduction

1.1 *Objetivo e pergunta de pesquisa*

- Como a interação oceano-atmosfera afeta a energética de sistemas ciclônicos no Atlântico Sul?

1.2 *Objetivos específicos*

- Determinar padrões, através do Ciclo Energético de Lorenz, para os ciclones atuantes no Atlântico Sul dentre o período 1979-2020;
- Avaliar qual o conjunto de parametrizações microfísicas e de convecção propiciam que o modelo MPAS-A apresente simulações mais realistas do Furacão Catarina, em diferentes estágios de desenvolvimento do sistema;
- Determinar o impacto das diferentes configurações do modelo na energética do sistema;
- Avaliar o impacto da perturbação da temperatura da superfície do mar na energética de sistemas ciclônicos atuantes no Atlântico Sul, através do estudo de casos representativos.

Chapter 2

Theoretical Background

2.1 Cyclones: Categories and Definitions

For an effective analysis and study, a phenomenon must first be accurately defined. The Glossary of Meteorology by American Meteorological Society (2012) characterizes a "cyclone" as "An atmospheric cyclonic circulation, a closed circulation. A cyclone's direction of rotation (counterclockwise in the Northern Hemisphere) is opposite to that of an anticyclone. (...) Because cyclonic circulation and relative low atmospheric pressure usually coexist, in common practice the terms cyclone and low are used interchangeably. Also, because cyclones are nearly always accompanied by inclement (often destructive) weather, they are frequently referred to simply as storms". This definition categorizes cyclones into sub-types based on their occurrence location: tropical, extratropical, and subtropical cyclones (Reboita et al., 2017, e.g.). This classification is supported by the assumption that cyclones within the same latitude bands share genesis environments and dynamic maintenance processes. There are also cyclones whose genesis is found in high latitudes, called polar lows (Emanuel and Rotunno, 1989; Harrold and Browning, 1969, e.g.). These will not be discussed in depth as the focus of the present study is on the systems generated in the adjacent regions to the South American coast.

The aforementioned definition, while broad, lacks precise criteria. Thus, subsequent sections will employ the Aristotelian approach to elucidate physical phenomena (Aristotle and Aristotle, 1933). Aristotelian causes, foundational to Aristotle's philosophy, offer a comprehensive explanation for an object or phenomenon's existence through four types: material, formal, efficient, and final causes. The ensuing subsections will detail each cause, enhancing the understanding of related phenomena. For each cyclone type — extratropical

and tropical — a discussion of the causes will facilitate a direct comparison between the systems.

It is important to note that the structure and mechanisms underlying the genesis and development of cyclones have been well-documented since the mid-twentieth century, leading to the inclusion of many historical references. The aim is to highlight distinctions between cyclone types, a comparison not commonly made in literature. Meteorologists often specialize as "tropical meteorologists" or "mid-latitude meteorologists", a division reflected in educational materials. Some texts focus exclusively on mid-latitude or tropical dynamics (Chan and Kepert, 2010; Bluestein, 1992, e.g.), while others that address both, treat them separately (Holton, 1973; Donald Ahrens and Henson, 2015, e.g.). Although this separation is customary and beneficial, juxtaposing the two offers novel insights, as explored in the following sections.

2.1.1 Material Causes

Material cause, within the Aristotelian framework, denotes the substance or constituents that form an object. It encompasses the matter or physical elements constituting an entity, serving as the foundation for its existence. For instance, wood acts as the material cause for a table, just as water serves as the material cause for a river. Applied to cyclonic systems, the material cause encompasses the air masses forming these systems, particularly emphasizing their thermal structure. This section elaborates on this concept, showcasing its relevance in defining and categorizing cyclonic systems.

The concept of an air mass, as introduced by Swedish meteorologist Tor Bergeron in 1928, describes a large body of air characterized by uniform temperature, moisture, and other properties, extending over 500 to 5000 km and encompassing the troposphere's full height (Stull, 2015). Air masses are classified based on their temperature, moisture content, stratification, and turbidity levels. Additionally, air masses originate from specific source regions, areas conducive to their formation. The characteristics of an air mass are significantly influenced by its source region's surface conditions, necessitating a flat terrain and mild winds for its development (Donald Ahrens and Henson, 2015). Heat transfer between the surface and the air is gradual, requiring the air mass to remain over its source region for an extended period to assimilate its properties (Spiridonov and Ćurić, 2021). Therefore, mid-latitudes, characterized by variable meteorological conditions and strong

winds, are generally unsuitable for air mass formation.

Bergeron's classification system is the most widely accepted methodology for categorizing air masses. It utilizes letters to denote the moisture content and the origin of air masses (Spiridonov and Ćurić, 2021). The initial letter signifies the air mass's moisture source—continental (dry) or maritime (moist)—while the subsequent letter indicates the geographical origin of the air mass, whether it be tropical (T), polar (P), arctic/antarctic (A), equatorial (E), or monsoonal (M). Figure 2.1 illustrates the spatial distribution of air masses according to Bergeron's scheme. Upon the encounter of two distinct air masses, immediate mixing does not occur, resulting in a temporary discontinuity at their intersection, known as fronts (Spiridonov and Ćurić, 2021; Donald Ahrens and Henson, 2015).

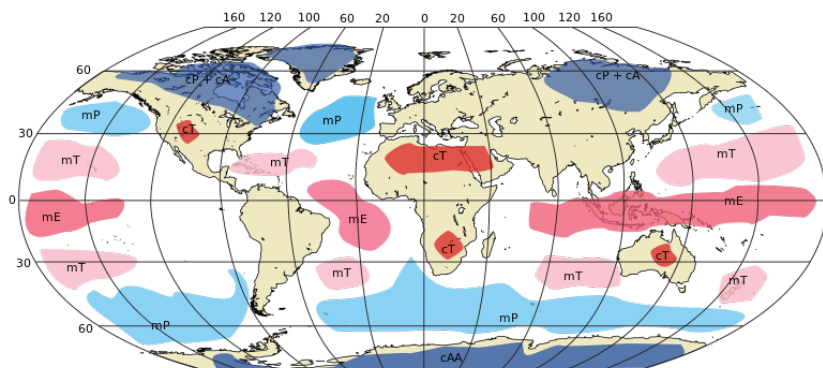


Figure 2.1: Spatial distribution of air masses according to Bergeron's classification. Credit: public domain (<https://commons.wikimedia.org/w/index.php?curid=12526643>).

Therefore, the validity of the traditional cyclone classification—tropical, extratropical, and subtropical—relies on the premise that different types of cyclones are initiated by distinct air masses. Specifically, tropical cyclones originate from warm, moist air masses that span the entire troposphere and form over warm tropical waters (Gray, 1968; Frank, 1977a; Ramage, 1959; Riehl, 1948). In contrast, extratropical cyclones are associated with frontal zones at mid-latitudes, where two different air masses meet, and are typically linked to cold cores (Bjerknes and Holmboe, 1944; Shapiro and Keyser, 1990; Hart, 2003). However, intense marine extratropical cyclones can experience warm seclusion, resulting in a warm core at the system's center (Hart, 2003; Shapiro and Keyser, 1990). Subtropical cyclones feature a hybrid structure between tropical and extratropical systems, with warm, moist cores that are less pronounced and shallower than those in tropical cyclones (Hart, 2003).

Hart (2003) offers an objective methodology for identifying the thermal structure of cyclonic systems. This analysis focuses solely on tropospheric levels (up to 300 hPa) because cyclones display an opposing thermal signal in the stratosphere. The study examines layers between 900 and 600 hPa and between 600 and 300 hPa, which have comparable masses. Levels below 900 hPa are excluded to prevent extrapolation below the ground or into the boundary layer, which may not accurately represent the cyclone's structure in the free atmosphere. Consequently, the variable corresponding to the cyclonic perturbation in height is defined as follows:

$$\Delta Z = Z_{MAX} - Z_{MIN} \quad (2.1)$$

Where Z_{MAX} and Z_{MIN} represent the maximum and minimum geopotential heights at a specific isobaric level, measured within a 500 km radius from the cyclone's center. Following this definition:

$$\Delta Z = \frac{dg|V_g|}{f} \quad (2.2)$$

Here, d denotes the distance between the geopotential height extremes, g is the acceleration due to gravity, f represents the Coriolis parameter, and V_g is the geostrophic wind speed. Consequently, the cyclone's vertical structure (indicative of a cold or warm core) is determined by the vertical gradient of ΔZ , which is proportional to the magnitude of the scaled thermal wind (V_T) for a constant d , applied across two tropospheric layers of equal mass:

$$\left. \frac{\partial(\Delta Z)}{\partial \ln p} \right|_{600hPa}^{300hPa} = -|V_T^U| \quad (2.3)$$

$$\left. \frac{\partial(\Delta Z)}{\partial \ln p} \right|_{900hPa}^{600hPa} = -|V_T^L| \quad (2.4)$$

where V_T^U and V_T^L symbolize the thermal winds at upper and lower levels, respectively. As such, positive values of $-V_T$ signify a warm core within the respective layer, whereas negative values indicate a cold core.

The relationship between the temperature and depth of the core within cyclonic systems is detailed through a phase diagram by Hart (2003), depicted in Figure 2.2. This diagram utilizes the abscissas to represent the parameter $-V_T^L$, illustrating the low-level core's

thermal structure. The ordinates display $-V_T^U$, portraying the high-level core's thermal structure. Integrating these metrics allows for discerning whether a system possesses a warm or cold core, and if it is shallow or deep. Figure 2.2 includes typical positions representative of different cyclonic types within the phase space. As noted by Hart (2003), a system may shift within this diagram throughout its lifecycle, making the depiction general for each cyclone category. Additionally, Hart proposes a diagram for the horizontal structure of these systems, related to their formal causes, which is addressed in Section 2.1.2.

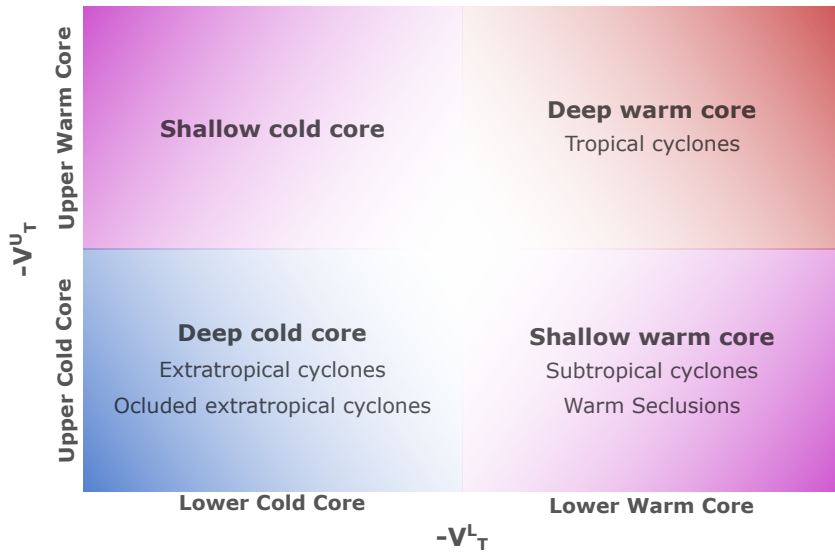


Figure 2.2: Phase diagram showing the relationship between the core temperature of cyclonic systems and their classification. Adapted from Hart (2003).

Thus, material causes, tied to the thermal structure of cyclonic systems, offer a foundational method for classifying and differentiating cyclone types. This classification leverages the phase diagram by Hart (2003) for an objective categorization. Accordingly, extratropical cyclones are characterized by cold, deep cores, whereas tropical cyclones feature warm, deep cores. This spectrum isn't binary; there exists a gradient of thermal structures with systems exhibiting intermediate features classified as subtropical cyclones. Nevertheless, relying solely on thermal attributes for classification is insufficient. For instance, extratropical cyclones, through the warm seclusion process (Shapiro and Keyser, 1990, e.g.), can develop warm, shallow cores (Hart, 2003), indicating the necessity for a broader analysis incorporating additional Aristotelian causes for a comprehensive classification.

2.1.2 Formal Causes

The formal cause concerns the essence or identity that defines a thing, essentially its design, structure, or conceptual blueprint that marks it as a particular type. To revisit the earlier example of a table from Section 2.1.1, its formal cause is the design that qualifies it as a table rather than a chair. In the context of cyclones, the formal cause refers to the system's organizational structure, such as the configuration of convection bands and/or fronts, along with the low-pressure pattern.

Extratropical cyclones, typically associated with mid-latitudes and frontal structures, exhibit an average diameter between 1200 and 1800 km. This size fluctuates over their lifecycle, with the cyclone's diameter expanding by up to 150% during its intensification phase (Simmonds, 2000; Rudeva and Gulev, 2007). However, the spatial complexity and variability of these systems throughout their lifecycle pose methodological challenges for accurately estimating their dimensions and comparing findings across different studies.

The seminal model describing the formation and horizontal structure of extratropical cyclones was introduced by Bjerknes (1919), illustrated in Figure 2.3. This model showcases the cyclone's movement along a central horizontal line, with the "steer line" demarcating the boundary that influences the cyclone's trajectory, characterized by warm air masses to its left. The "squall line" indicates a zone of intense meteorological activity, marked by strong winds and often heavy precipitation, with cold air masses located to its left. The "fore runner" represents a region of diverging airflow.

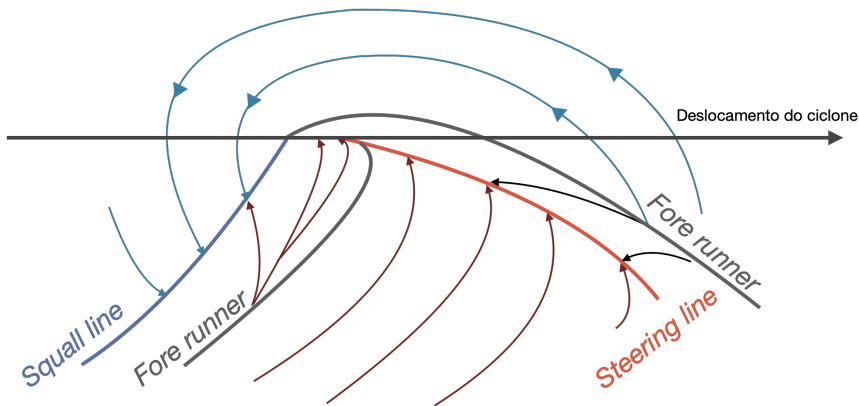


Figure 2.3: Representation of the Bjerknes model for the extratropical cyclone formation process and its horizontal structure. Cold air regions are illustrated with blue lines, while warm air regions with red lines. Adapted from Bjerknes (1919).

Bjerknes and Solberg (1922) realized that the model proposed in Bjerknes (1919) repre-

sented just one phase in the life cycle of cyclones, indicating that there are several stages of development. Bjerknes and Solberg (1922) established the Polar Front Theory, which is the foundation of the so-called Norwegian cyclone model. Schultz et al. (1998) synthesizes and describes the development of extratropical cyclones according to this theory, so that a visual representation of the horizontal structure at the surface during different stages of cyclone evolution is found in Figure 2.4a. In the first stage, the incipient cyclone presents a narrow and long cold front, and a wide and short warm front (Figure 2.4aI). After this, the cyclone deepens, with a narrowing of the warm section of the cyclone through the rotation of the cold front towards the warm front (Figure 2.4aII). As cold air is denser and, therefore, facilitates more intense horizontal pressure gradients, it moves faster than the warm air. As the cold air at the front of the cyclone approaches the cold air at the rear of the system (Figure 2.4aIII), the warm air is trapped in the center of the system, a phenomenon called warm seclusion. As the cold front continues to move, the warm air at the surface is overtaken by the cold air and is forced to ascend to upper levels. This process is called occlusion, being responsible for trapping the cold air in the core of the system (Figure 2.4aIV). With the continuation of occlusion, the baroclinicity along the warm front can become so diffuse that the cyclone appears not to have a well-defined warm front.

Bjerknes and Solberg (1922) acknowledged that the model presented in Bjerknes (1919) captured only a singular phase in the life cycle of cyclones, leading to the development of the Polar Front Theory. This theory defines what is known as the Norwegian cyclone model. Schultz et al. (1998) provides a synthesis of extratropical cyclone development according to this theory, including a depiction of the surface horizontal structure at various stages of cyclone evolution in Figure 2.4a. Initially, the nascent cyclone features a narrow, elongated cold front and a broader, shorter warm front (Figure 2.4aI). Subsequently, the cyclone deepens as the cold front rotates toward the warm front, narrowing the cyclone's warm sector (Figure 2.4aII). Given the greater density of cold air, which generates stronger horizontal pressure gradients and moves more swiftly than warm air, the cold front eventually encroaches on the system's rear cold air (Figure 2.4aIII), trapping warm air at the system's center—a process known as warm seclusion. As the cold front progresses, the surface-level warm air is displaced by cold air and forced upward, a phenomenon termed occlusion, which entraps cold air at the system's core (Figure 2.4aIV). The occlusion process may eventually diffuse the baroclinicity along the warm front to such an extent that

the cyclone seems to lack a distinct warm front.

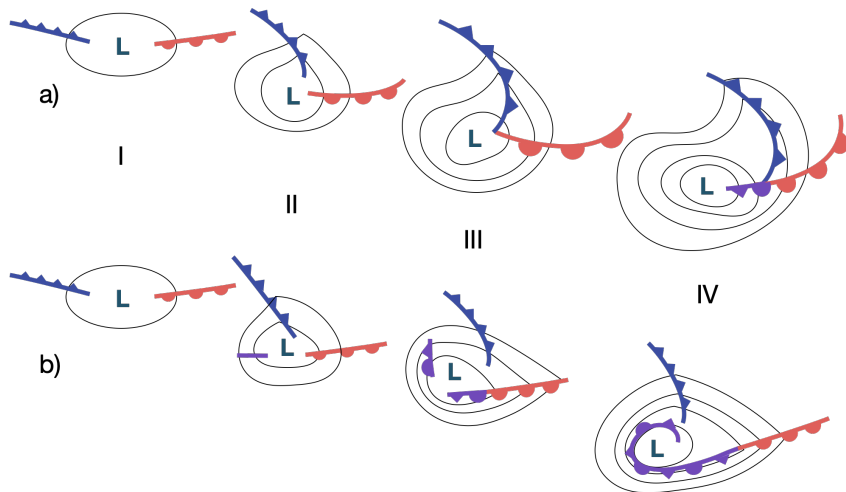


Figure 2.4: Cyclonic models by Bjerknes (1919) (a) and Shapiro and Keyser (1990) (b), illustrating the systems' horizontal structure across different developmental stages (I to IV). Adapted from Schultz et al. (1998).

From the advancements enabled by the satellite era, Shapiro and Keyser (1990) introduced a revised cyclonic model, acknowledging that not all observed cyclones conformed to the Norwegian model. Termed the Shapiro-Keyser model, it is also summarized by Schultz et al. (1998), with its visualization in (Figure 2.4b). Initially mirroring the development outlined by Bjerknes and Solberg (1922) (Figure 2.4bI), this model diverges as the cold front extends perpendicularly to the warm front instead of encircling the system (Figure 2.4bII). As the system strengthens, the polar side of the cold front weakens, allowing the warm front to encircle the system's western sector (Figure 2.4bIII). At peak intensity, cold air encases the warm air near the cyclone's center, creating a warm seclusion (Figure 2.4bIV).

Schultz et al. (1998) emphasizes that these models are complementary rather than mutually exclusive, suggesting that the Norwegian model is more applicable to systems forming under diffluent flow with significant amplitude, often at the terminal end of storm tracks and on western continental edges, characterized by a meridional elongation of the cyclone and its fronts. Conversely, the Shapiro-Keyser model is more suited to systems emerging under confluent, low amplitude base flow, typically exhibiting east-west elongation. However, these models alone do not fully account for the formal causes of extratropical cyclones, indicating a continuum where different systems may align more closely with one

model or the other (Schultz et al., 1998).

Tropical cyclones, unlike their extratropical counterparts, lack frontal structures and exhibit organized, symmetric circulation near the surface, forming over warm tropical or subtropical waters with intense winds below the surface (Frank, 1977a; Gray, 1968). Their diameters vary, ranging from 100 to 1000 km at maturity, expanding up to 2000 km during intensification. However, the area of intense convection and stronger winds typically spans a radius of about 100 km (Holton, 1973).

Characterized by a central cyclonic circulation at lower tropospheric levels and anticyclonic circulation in the upper troposphere, tropical cyclones are associated with intense precipitation and horizontal pressure gradients, leading to spiraled winds near the surface that become increasingly circular towards the system's center, or eye (Frank, 1977a,b; Terry, 2007; Weatherford and Gray, 1988). These systems exhibit more intense pressure gradients—and consequently stronger winds—than extratropical cyclones (Spiridonov and Ćurić, 2021). Based on wind speed, they are classified into tropical depressions (maximum winds less than 60 km/h), tropical storms (winds between 60 and 110 km/h), and tropical cyclones (winds exceeding 110 km/h) (Spiridonov and Ćurić, 2021). Their nomenclature varies by region: "hurricanes" in the North Atlantic and North Pacific, "typhoons" in the Northwest Pacific, and "cyclones" in the Indian Ocean (Donald Ahrens and Henson, 2015).

The structure of tropical cyclones comprises three main components: the eye, the eye wall, and surrounding convection bands (Figure 2.5). The eye is the calm, warm central region, with a radius of 5 to 50 km, encircled by the eye wall—a cloud ring about 10 to 20 km wide where intense upward vertical movements occur, facilitating mass transport to higher levels (Shea and Gray, 1973; Jorgensen et al., 1985). Although these vertical movements are typically less vigorous than those in extratropical cyclones (Jorgensen et al., 1985), the inner core, consisting of the eye and eye wall, hosts the most intense winds and lowest atmospheric pressures (Weatherford and Gray, 1988). The primary convection band, a nearly stationary feature, spirals inward from the system's outer edges towards the eye wall, where it becomes roughly tangent (Willoughby et al., 1984).

Given the delineated formal causes (organizational structure) for both extratropical and tropical cyclones, it's evident that their structures diverge significantly. Simplified, extratropical cyclones, forming at the interface between distinct air masses, are associated with frontal systems, providing them an asymmetric feature. Conversely, tropical cyclones

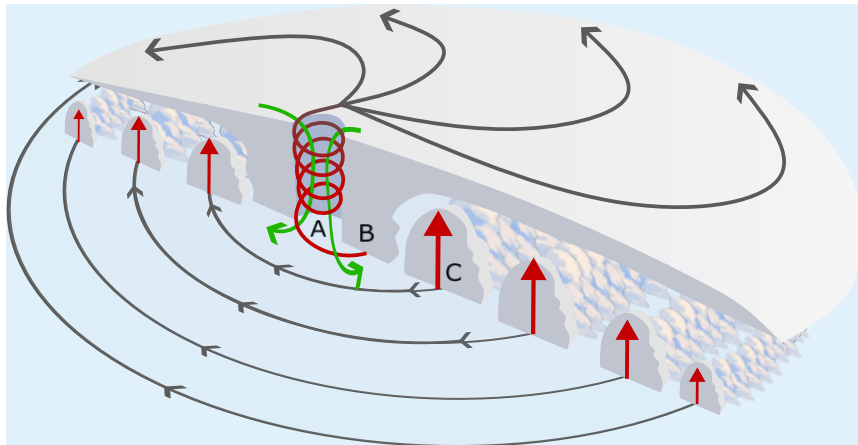


Figure 2.5: Cross-sectional view of a mature tropical cyclone in the Southern Hemisphere, illustrating the eye (A), eye walls (B), and convection bands (C), along with upward (red arrows) and downward (green arrows) vertical movements, horizontal wind movement (grey arrows), and sea-level pressure contours. Inspired from: Bluestein (1992).

exhibit symmetry, characterized by a circular eye and spiraled convection bands extending from the eye wall. Addressing this distinction, Hart (2003) introduces a metric assessing the relative thickness asymmetry between the 900 and 600 hPa levels, termed the B parameter:

$$B = h \left(\overline{Z}_{600hPa} - \overline{Z}_{900hPa} \right)_R - \left(\overline{Z}_{600hPa} - \overline{Z}_{900hPa} \right)_L \quad (2.5)$$

where Z represents the isobaric height, R and L denote the right and left sides relative to the system's motion, the overbar signifies an average over a 500 km semicircle, as defined in Equation 2.1, and h is a constant set to +1 or -1 for the northern and southern hemispheres, respectively. Mature tropical cyclones exhibit a B value near zero, indicating thermal symmetry (non-frontal), while extratropical cyclones show significant B values, signaling thermal asymmetry (frontal). Positive B values suggest the presence of warm air to the right of the cyclone in the southern hemisphere (and vice versa in the northern hemisphere), aligning with the thermal wind relationship from quasi-geostrophic theory (Sutcliffe, 1947; Trenberth, 1978).

Hart (2003) proposed a diagram correlating symmetry with V_T^L (Equation 2.4), depicted in Figure 2.6, offering a supplementary classification to that shown in Figure 2.2. Here, extratropical cyclones are categorized as cold and asymmetric (frontal), whereas tropical cyclones are warm and symmetric (non-frontal). Like the earlier diagram, this classification suggests a continuum, with systems displaying intermediate features labeled as subtropical.

Unlike solely thermal-based classifications, this model allows for differentiation of extra-tropical cyclones undergoing occlusion, as these systems begin to exhibit symmetry during this phase. Hence, the diagram involving the B parameter and V_T^L presents an objective methodology to classify cyclones' formal causes.

While the phase diagrams by Hart (2003) facilitate objective classification criteria for cyclonic systems, gaps remain. For instance, warm seclusions share formal and material causes with hybrid systems, leading to potential misclassification by forecasters and climate data analysis algorithms using these diagrams exclusively. Additionally, polar lows, characterized by both a warm core and symmetric structure, were initially likened to hurricanes (Rasmussen, 1989; Emanuel and Rotunno, 1989; Nordeng and Rasmussen, 1992; Rasmussen, 1985, 1979). However, recent studies, such as Stoll et al. (2021), suggest their spiral bands and thermal core may result from the warm seclusion process, as per the Shapiro-Keyser cyclone development model. These discussions underscore that material and formal causes alone do not suffice for a comprehensive cyclone classification, necessitating further analysis.

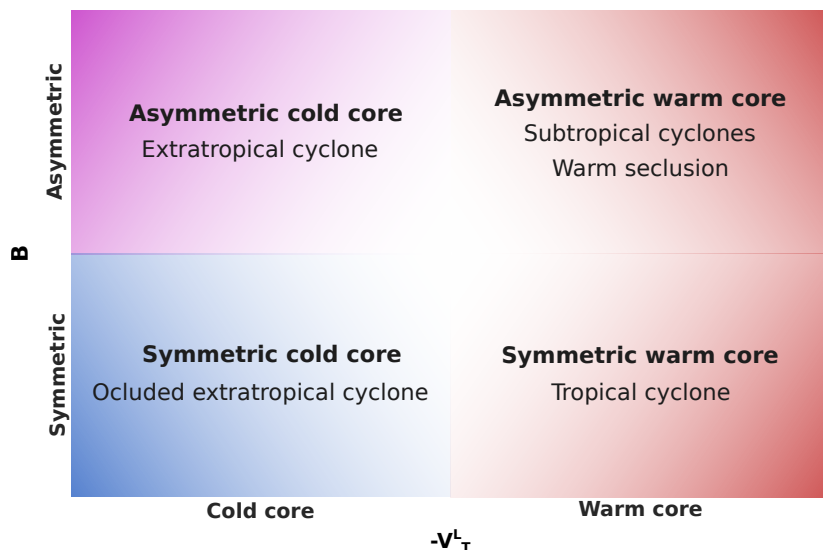


Figure 2.6: Phase diagram illustrating the relationship between cyclonic systems' core temperature and symmetry, offering a distinct classification procedure. Adapted from Hart (2003).

2.1.3 Efficient Causes

The efficient cause represents the agent or process that leads to the creation or transformation of something, answering the "how" or "why" behind an occurrence. It encompasses

the actions or processes that result in the existence of an entity. For example, in the creation of a table, the carpenter serves as the efficient cause. In the context of cyclones, the efficient cause includes the physical and dynamic processes responsible for their formation and intensification. These processes essentially act as destabilization mechanisms, triggering atmospheric disturbances that evolve into a cyclonic configuration.

While the polar front theory offers a descriptive perspective, it falls short of providing a comprehensive theoretical model for the physical processes involved in system formation. Still, it related these processes with thermal contrasts in the atmosphere, or baroclinic zones (Bjerknes, 1919; Bjerknes and Solberg, 1922), describing cyclones as emergent phenomena arising at the boundary of two distinct air currents—polar and tropical—flowing in opposite directions (east-west and west-east, respectively), differentiated by thermal contrasts (cold and warm, respectively). A destabilization of the flow occurs when the velocity difference between these currents surpasses a critical threshold, generating a frontal wave that intertwines the currents and reduces their velocity contrast. Some of these frontal waves are unstable and can spontaneously amplify, representing the genesis mechanism of cyclones according to this theory.

The Polar Front Theory provides a detailed account of the structure and formation processes of extratropical cyclones, as shown in Figure 2.7, depicting a transverse model of a developing cyclone (Bjerknes and Solberg, 1922). This model features horizontal isotherms indicative of temperature variations parallel to the ground, with warm air central to the model, characteristic of the warm front, and cold air on the edges. Initially (Figure 2.7a), the isotherms of cold air extend horizontally until convergence forces the ascent of warm air to higher atmospheric levels. This conversion of potential to kinetic energy continues as the cold air from both sides of the cyclone advances to mid-atmospheric levels, further driving the ascent of warm air. The adiabatic cooling of ascending warm air leads to temperature equalization and depletion of the system's potential energy reserve, while the air mass movement is then sustained by inertia. After occlusion (Figure 2.7b and c), inertia maintains the ascent of cold air, which cools adiabatically, utilizing the system's kinetic energy to counteract gravity. Initially, there is still kinetic energy production at high levels and its consumption at low levels. However, as the elevated warm sector cools and temperatures equalize (Figure 2.7d), kinetic energy production halts. Eventually, friction outweighs kinetic energy production, leading to its dissipation.

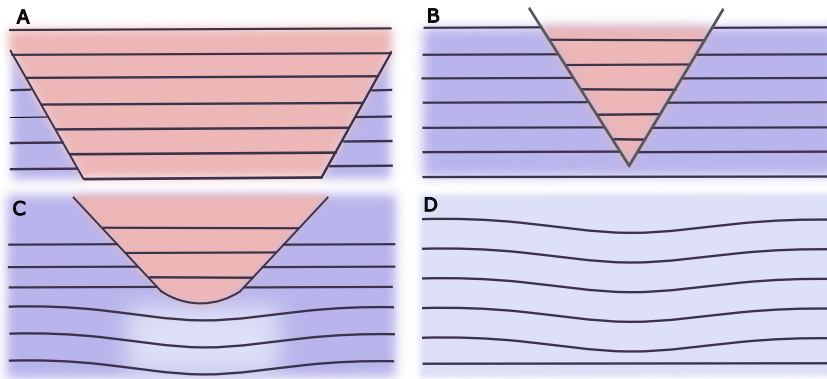


Figure 2.7: Cross-sectional depiction of an extratropical cyclone's development through its various stages, adapted from Bjerknes and Solberg (1922). Stage A shows horizontal isotherms where cold air converges, leading to the ascent of warm air. In Stage B, the system begins occlusion as cold air advances to mid-atmospheric levels, further promoting the ascent of warm air. Stage C continues the occlusion, with sustained ascent of cold air by inertia and kinetic energy consumption. Stage D represents the cessation of kinetic energy production as temperatures equalize and friction begins to dominate, leading to energy dissipation. Warm (red) and cold (blue) sectors are indicated alongside the isotherm lines.

Since the advent of the polar front theory, our comprehension of atmospheric dynamics has evolved significantly, incorporating new concepts into the understanding of extratropical cyclones. This evolution has led to a diverse array of approaches aimed at describing the dynamic and thermodynamic processes underlying the genesis and development of these systems. Consequently, there is no singular, unified theory regarding extratropical cyclogenesis. For instance, Bjerknes and Holmboe (1944) identified the formation regions of extratropical cyclones as zones of dynamic instability associated with the westward-flowing jet stream, employing the tendency equation to analyze atmospheric instability. Other studies have approached cyclogenesis through various lenses, including slantwise convection, the omega equation, potential vorticity, primitive equations, and diabatic processes (Hoskins, 1990, e.g.). Additionally, Schultz et al. (1998)'s work categorizes cyclones into those aligning with the Norwegian model versus the Shapiro-Keyser model, differentiating them based on environmental conditions related to the base state flow (diffluent for the former and confluent for the latter). This section will primarily focus on the development of these systems from the perspective of dynamic destabilization mechanisms in the atmosphere, linking these mechanisms to the energetics of transient atmospheric systems, further explored in Section 2.4.

Baroclinic instability (I_{BC}) is identified as the principal mechanism behind the deve-

lopment of typical extratropical cyclones (Charney, 1947; Bjerknes and Solberg, 1922). As Holton (1973) explains, I_{BC} involves the amplification of small disturbances in areas with strong velocity shears, such as jet streams, where the disturbances extract energy from the jet and grow in size and intensity. In the Earth's atmosphere, I_{BC} is primarily driven by the meridional temperature gradient, especially at lower levels, and is linked to vertical shear via the thermal wind (V_T) relationship, frequently occurring in the polar frontal zone. Baroclinic disturbances can also intensify existing temperature gradients, leading to the formation of frontal zones.

Charney (1947)'s seminal study on I_{BC} sheds light on the intricate mechanisms behind the formation and evolution of weather patterns, including cyclones and long waves in middle and high latitudes. Employing a simplified model that allows for analytical solutions, Charney not only corroborated previously theorized concepts about atmospheric behavior but also deepened the understanding of how wind shear and temperature variations vertically contribute to atmospheric instability. His analysis indicates that mid-latitude westward-flowing currents are inherently dynamically unstable. This insight elucidates how specific disturbances can exponentially grow within a large-scale atmospheric flow field, explicating the process through which such disturbances can amplify and culminate in the characteristic weather systems observed in middle and high latitudes.

Eady (1949) made significant advancements in the understanding of I_{BC} in the atmosphere, building on the work of Charney (1947). Eady's research, which employed a solvable simplified model, delved into the atmospheric instability arising from disturbances that exponentially grow within a large-scale atmospheric motion context. His analysis elucidated how specific conditions of stability, wind shear, and vertical temperature variations contribute to I_{BC} , proposing a mechanism for the formation and evolution of weather patterns such as cyclones and long waves in middle and high latitudes. Eady highlighted that certain disturbances grow exponentially faster than others, akin to a process of natural selection in the atmosphere, leading to the emergence of predominant weather patterns observed in middle latitudes, including cyclonic systems.

Following the seminal works of Charney (1947) and Eady (1949), Palmén and Newton (1969) synthesized the main findings from the subsequent extensive literature on I_{BC} . Firstly, it is noted that the amplification of atmospheric disturbances is wavelength-dependent, with disturbances below a critical length never amplifying. The optimal growth occurs

in intermediate wavelengths (between 2500 and 5000 km), with an inverse relationship between this optimum and latitude—the closer to the Equator, the larger the critical size below which all waves are unstable. Additionally, there exists a proportional relationship between the intensification rate and vertical wind shear for wavelengths of maximum instability, and for longer waves, an increase in wavelength necessitates stronger shear to maintain equivalent growth rates.

In his analysis, Petterssen and Smebye (1971) categorizes extratropical cyclones into types based on the dynamic processes driving their development. Type A cyclones follow the Polar Front Theory model, with the initial disturbance arising at low levels within a maximal baroclinic zone (frontal), beneath a nearly zonal upper-level jet (Figure 2.8iA). As these cyclones develop, a cold trough forms at high levels (Figure 2.8iB), remaining inclined to the cyclone's axis until occlusion occurs and surface baroclinicity diminishes (Figure 2.8iC). Conversely, type B cyclones initiate from high-level forcing, as an upper-level trough moves over an area not necessarily featuring a frontal zone (Figure 2.8iiA). As these systems mature, the gap between the high-level trough and the surface system narrows, with an increase in surface baroclinicity relative to the initial stage (Figure 2.8iiB), culminating in the alignment of the high-level cyclonic vortex with the surface low, leading to system occlusion (Figure 2.8iiC).

Just as Hart (2003)'s classification presents a continuum, so too does Petterssen and Smebye (1971)'s delineation of cyclone types, with A and B not being distinct categories due to the existence of systems displaying hybrid characteristics. Petterssen and Smebye (1971) observed that purely type A cyclones are more common, whereas purely type B cyclones are rare, attributing this to the fact that some type of baroclinicity is often present in the mid-latitudes. However, Petterssen noted a tendency for type A cyclones to develop over oceans and type B cyclones over continents, though subsequent research, such as by McLennan (1988) and Deveson et al. (2002), has identified type B systems forming over oceanic regions as well. Furthermore, Deveson et al. (2002) introduced a new classification, type C cyclones, found in high latitudes with similarities to polar lows, characterized by an even stronger high-level forcing related to the movement of a broad trough over oceanic regions. This study also highlighted the potential for cyclones to transition between types throughout their lifecycle.

The central role of baroclinic instability (I_{BC}) in the development of extratropical cy-

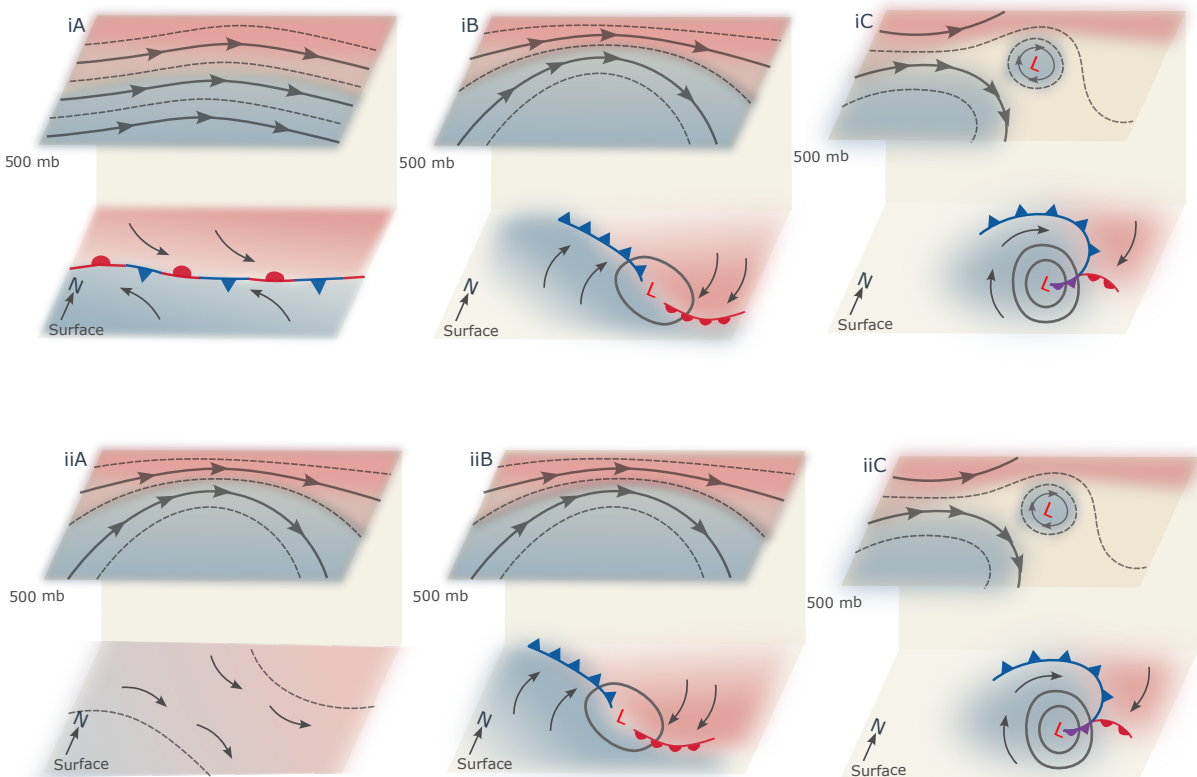


Figure 2.8: Illustration of the development model for cyclones types A (i) and B (ii), depicting the stages of formation (A), intensification (B), and maturity (C), as proposed by Petterssen and Smebye (1971). Inspired by Donald Ahrens and Henson (2015).

clones is well-established, yet the significance of heat flows and diabatic heating cannot be overstated. Diabatic heating involves heat exchanges between a system and its surroundings through processes such as condensation, evaporation, or radiation. Convective activities leading to upward atmospheric movements cause diabatic expansion and thus cooling in air parcels, leading to saturation and the release of latent heat. Such mechanisms provide an additional energy source for the development of extratropical cyclones, as documented in the literature (Chang et al., 2002, e.g.). Numerical models incorporating I_{BC} alongside heat flows have shown that instabilities generated under these conditions yield more intense cyclones with faster development rates (Gall, 1976; Whitaker and Davis, 1994; Gutowski et al., 1992), a phenomenon referred to as moist baroclinic instability.

A pivotal study by Hoskins and Valdes (1990) underscores the importance of diabatic fluxes in the development of extratropical cyclones, demonstrating that cyclonic development is preferentially located in regions of maximal baroclinicity over the oceans. However,

the heat transport facilitated by these systems tends to mitigate the baroclinicity. The study suggests that diabatic heating, through the latent heat release from individual systems, contributes to sustaining regional baroclinicity. It also highlights the role of sensible heat exchanges between the cold air associated with these systems and the warm ocean currents along the eastern coastlines of continents.

Tropical cyclone formation, a topic of ongoing discussion among meteorologists, typically occurs over tropical or subtropical oceans, a region where the scarcity of in situ observations challenges the validation of theoretical models for formation and intensification. During World War II, data collected from the military base in Guam facilitated Riehl (1948) in proposing that the instability necessary for typhoon formation originates within the trade winds, contradicting the then-prevailing belief of inter-hemispheric air mass interactions being the primary cause. Subsequently, Yanai (1961)'s study on Typhoon Doris furthered the understanding of typhoon genesis, highlighting the significant role of latent heat released by convection. Yanai suggested a model for typhoon development, beginning with a disturbance in the trade winds and culminating in the formation of a typhoon characterized by a stabilized warm core.

Charney and Eliassen (1964) detailed the process of tropical cyclone intensification known as conditional instability of the second kind (CISK), which was the most accepted theory at the time (Figure 2.9i). According to CISK, the condensation of water vapor within convective areas releases latent heat, which can amplify pre-existing atmospheric vortices given an adequate moisture supply. This release of heat not only promotes further convection but also lowers sea-level pressure, thereby strengthening surface winds, enhancing moisture influx, and establishing a positive feedback loop. Charney underscored the ocean's surface role in providing the moisture necessary for sustaining convection, as well as the importance of surface friction in dissipating kinetic energy and fostering wind convergence within the moist surface boundary layer, thereby fueling the system with thermal energy from latent heat. This mechanism emphasizes the pivotal role of latent heat release at the cyclone's center as a disturbance amplification factor, leading to the intensification of the tropical depression.

However, it is important to note that the work of Charney and Eliassen (1964) consists of formulating a mathematical model and, therefore, does not offer a direct and didactic explanation of the processes involved. Thus, the interpretation of the proposed mecha-

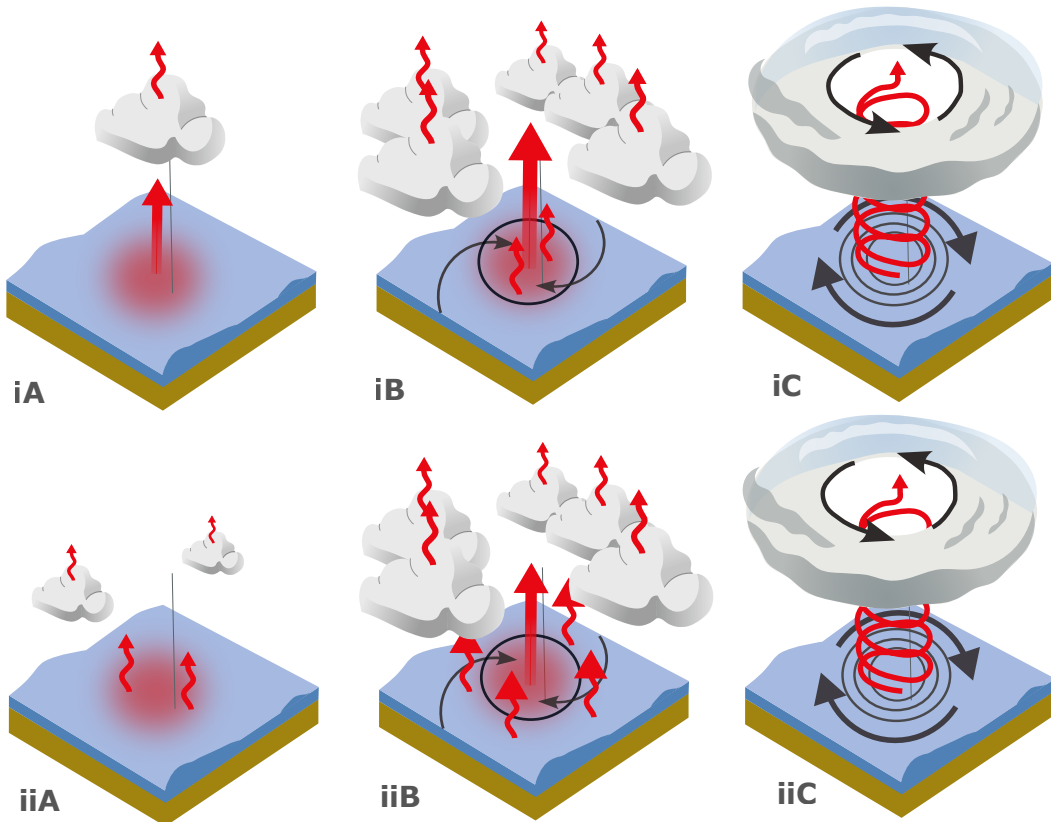


Figure 2.9: Comparative illustration of the CISK (i) and WISHE (ii) theories. A depicts the initial disturbance over warm ocean temperatures. Under CISK, the disturbance is initially fueled by latent heat from convection, whereas WISHE attributes the initial energy source to latent heat transfer from the ocean to the atmosphere. In the early development stage (B), both theories observe an increase in convection. CISK suggests this leads to reduced central pressure, drawing in more moisture and enhancing convection, which releases additional heat. WISHE proposes that surface wind interaction with the sea surface at low central pressure enhances heat release from surface water evaporation, further driving convection and subsequent latent heat release. By the tropical storm phase (C), the theories align on the feedback mechanisms fueling system intensification.

nisms is largely left as an exercise for the reader, which has resulted, over the years, in multiple interpretations, not all of them correct (Ooyama, 1982). Therefore, the explanation provided above seeks only to simplify the main processes proposed by Charney and Eliassen (1964).

While Charney and Eliassen (1964)'s work introduces a mathematical model for understanding tropical cyclone intensification through the CISK process, it doesn't offer a straightforward, didactic explanation of the involved mechanisms. This has left room for various interpretations over the years, not all of which have been accurate, as noted by Ooyama (1982). The explanation provided here aims to simplify the main processes

proposed by Charney's for clarity.

Challenging the CISK theory, Emanuel (1986), later refined by Yano and Emanuel (1991), introduced the Wind-Induced Surface Heat Exchange (WISHE) theory, emphasizing ocean-atmosphere interaction as the primary intensification mechanism for tropical cyclones (Figure 2.9ii). WISHE posits that the development of these systems depends on the thermal contrast between the atmosphere and the sea surface, mediated by latent heat transfer from the ocean to the atmosphere. This transfer is significantly amplified by surface wind speeds, with intense winds elevating evaporation rates and thus, moisture transfer. An initial atmospheric disturbance that promotes wind convergence toward its center can enhance this moisture transfer and convection intensity, fostering a positive feedback cycle. WISHE theory emphasizes the necessity of ocean temperatures exceeding 26°C for sufficient boundary layer convergence, vital for maintaining the system. Similar to CISK, interpretations of WISHE vary, with not all encapsulating the theory's full scope or accuracy (Montgomery and Smith, 2014); thus, the provided explanation concentrates on fundamental aspects for comparative purposes with CISK.

Despite advancements in identifying the prerequisites for tropical cyclone development—such as requisite sea surface temperatures, minimal vertical wind shear, and specific atmospheric conditions—consensus on the precise dynamic processes driving both formation and intensification remains elusive. This ongoing debate in meteorology is exemplified by the contrasting theories of CISK and WISHE, each proposing different intensification mechanisms for tropical cyclones (Craig and Gray, 1996; Gray, 1998; Montgomery et al., 2015; Ooyama, 1982; Montgomery and Smith, 2014, e.g.). Nonetheless, a common point between them is the acknowledgment that diabatic processes, fueled by ocean-atmosphere interactions and given an initial disturbance, are critical for providing energy and further intensifying the system. This section's goal is to delineate the development mechanisms of tropical versus extratropical cyclones, for which the simplified descriptions provided herein offer an adequate overview.

The role of diabatic heating in the intensification of tropical cyclones is underscored by the need for an initial atmospheric disturbance. Frank (1970) conducted an analysis of systems in the North Atlantic that give rise to disturbances capable of developing into tropical cyclones. He identified several sources of these disturbances, including those originating from the Intertropical Convergence Zone (ITCZ) and convection zones within

the Caribbean Sea. However, the majority are associated with tropical waves primarily emanating from the African continent. Frank also highlighted the process whereby baroclinic systems transition into warm-core structures through the convection-driven release of latent heat, effectively diminishing the system's original baroclinicity. This phenomenon is now recognized as the tropical transition of extratropical cyclones, a process further explored and detailed in works such as those by Hart (2003).

The genesis of tropical cyclones in the North Atlantic is intricately linked to the formation and development of African easterly waves, with the thermal contrast between the Sahara Desert and cooler southern regions playing a pivotal role in creating the African Easterly Jet (AEJ)—a key factor in generating these waves (Holton, 1973). The foundation for understanding such phenomena was laid by Kuo (1949), who pinpointed barotropic instability in zonal atmospheric flows as a vital mechanism. This instability, marked by a change in the sign of absolute vorticity, involves horizontal wind shear and allows vortexes to extract kinetic energy from the zonal wind flow (Holton, 1973).

Burpee (1972) initially connected African easterly wave development with the instability of the AEJ, due to both horizontal and vertical shears, pointing to the complex interaction between barotropic and baroclinic instabilities in the region. Following this, Rennick (1976) applied a linear pseudo-spectral model based on primitive equations, deducing that barotropic instability acts as a primary catalyst for wave development, while downplaying the roles of vertical shear and latent heat release in the early stages. This assertion was supported by Reed et al. (1977) through observational data, demonstrating that medium and low-level easterly waves meet the criteria for barotropic instability.

An energetic analysis by Norquist et al. (1977) differentiated the destabilization processes over land and ocean, with baroclinic conversion dominating over the continent and barotropic instability gaining importance over oceanic regions—where tropical cyclones predominantly form. More recently, Wu et al. (2012) employed reanalysis data to establish a geographical link between the AEJ's barotropic instability and the origination points of North Atlantic tropical cyclones, affirming the significance of the AEJ's barotropic instability in relation to tropical cyclogenesis.

The exploration of barotropic instability's role in tropical cyclone genesis extends beyond the North Atlantic, encompassing various global regions where similar dynamics foster local tropical cyclogenesis. While initial studies illuminated the significance of ba-

rotropic instability in the genesis of African easterly waves and their impact on North Atlantic tropical cyclone formation, subsequent research has broadened our understanding to include other tropical areas. For instance, Zehr (1992) discovered that most tropical cyclogenesis events in the North Pacific are associated with a monsoon trough that encourages local convection.

In addition to easterly waves, different types of tropical disturbances can also disrupt the base state and instigate tropical cyclogenesis. Ferreira and Schubert (1997) used a shallow water model to show how barotropic instability related to the ITCZ's collapse can initiate a series of tropical disturbances, with some progressing to become tropical cyclones. Further, Bembene et al. (2021) employed a global aquaplanet circulation model to illustrate the significant roles played by the ITCZ's latitudinal position and moisture effects in modulating barotropic instability and, consequently, tropical cyclone genesis, indicating the global influence of barotropic instability on tropical cyclogenesis through theoretical studies.

Observational evidence supports these theoretical insights. Maloney and Hartmann (2001) observed that the Madden-Julian Oscillation (MJO) phases conducive to westerly winds along the Pacific enhance barotropic conversions at low levels, thereby aiding tropical cyclone formation in both the Western and Eastern Pacific. Molinari et al. (1997) noted that temporal variations in the MJO can create conditions favorable for easterly wave growth, thereby affecting tropical cyclogenesis in the Eastern Pacific. Molinari et al. (2000) identified a link between the barotropic instability of the base state, associated with easterly wave occurrence, topographical effects, and the monsoon trough in fostering tropical cyclogenesis in the Eastern Pacific. Lastly, Cao et al. (2012) found that enhanced ITCZ convection during active phases of the Intraseasonal Oscillation generates a mean flow state conducive to barotropic instability, promoting tropical cyclogenesis in the Northwest Pacific.

While subtropical cyclones were identified in earlier works (Simpson, 1952), it wasn't until the study by Hart (2003) that they began receiving significant attention. The body of literature on these systems is still developing, with the processes behind subtropical cyclogenesis and development remaining an active area of research. Yanase et al. (2014) advanced the understanding of cyclone genesis by developing an Environmental Parameter Space, analyzing how cyclone genesis latitude correlates with factors like baroclinicity,

relative humidity, vertical velocity, and potential intensity. This last metric predicts a tropical cyclone's maximum possible strength based on environmental conditions such as sea surface temperature and atmospheric temperature profiles. The study found a clear correlation: extratropical cyclones are closely linked to baroclinicity, while tropical cyclones are associated with potential intensity. Conversely, an inverse relationship was noted—extratropical cyclones inversely relate to potential intensity and tropical cyclones to baroclinicity. Subtropical cyclones emerged in a transitional space, influenced by both baroclinicity and potential intensity, which supports the notion of these systems as hybrids between tropical and extratropical cyclones (Hart, 2003, e.g.). Additionally, da Rocha et al. (2019) suggested that subtropical cyclogenesis could be linked to various synoptic patterns, such as a shallow trough at mid-upper levels, a mid-upper level cutoff low, or a Rex blocking pattern. However, a comprehensive discussion delineating the principal environmental dynamics associated with subtropical cyclone development remains elusive, indicating a need for further investigation in this area.

The discussion provided thus far can be synthesized by comparing the efficient causes related to the development of both extratropical and tropical cyclones. Extratropical systems primarily develop through baroclinic instability, which may be initiated by disruptions in the surface meridional temperature gradient or by the influence of an upper-level trough, linking to baroclinic regions via the thermal wind relationship (Holton, 1973; Spilidonov and Ćurić, 2021). In contrast, tropical cyclone genesis is largely influenced by barotropic instability within the base state atmosphere, with subsequent disturbances intensifying through processes related to latent heat release, as explained by either CISK or WISHE theories.

This comparison illustrates that extratropical cyclone formation is closely tied to thermal variance driving baroclinic instability, whereas tropical cyclone genesis hinges on barotropic instability, succeeded by a reinforcing latent heat release feedback mechanism. Despite the absence of a unified diagram akin to Hart (2003)'s material and formal causes of cyclones, Silva Dias et al. (2004) proposed a conceptual model potentially bridging this gap (Figure 2.10). This model situates extratropical cyclones within the domain of baroclinic instability; tropical cyclones under barotropic instability; and subtropical cyclones where both instabilities might coexist or compete. The model also distinguishes systems by their reliance on diabatic processes, particularly latent heat release.

The viewpoint of Silva Dias et al. (2004) gains partial validation through Yanase et al. (2014)'s analysis, which linked different cyclone types to specific environmental parameters. Furthermore, Yanase et al. (2014) emphasized the critical role of relative humidity across all cyclone categories, supporting Silva Dias et al. (2004)'s emphasis on the essential role of latent heat release in cyclone dynamics. The current study will introduce a conceptual model, detailed in Chapter 5, aiming to synthesize the primary mechanisms driving cyclonic development and explore their broader implications.

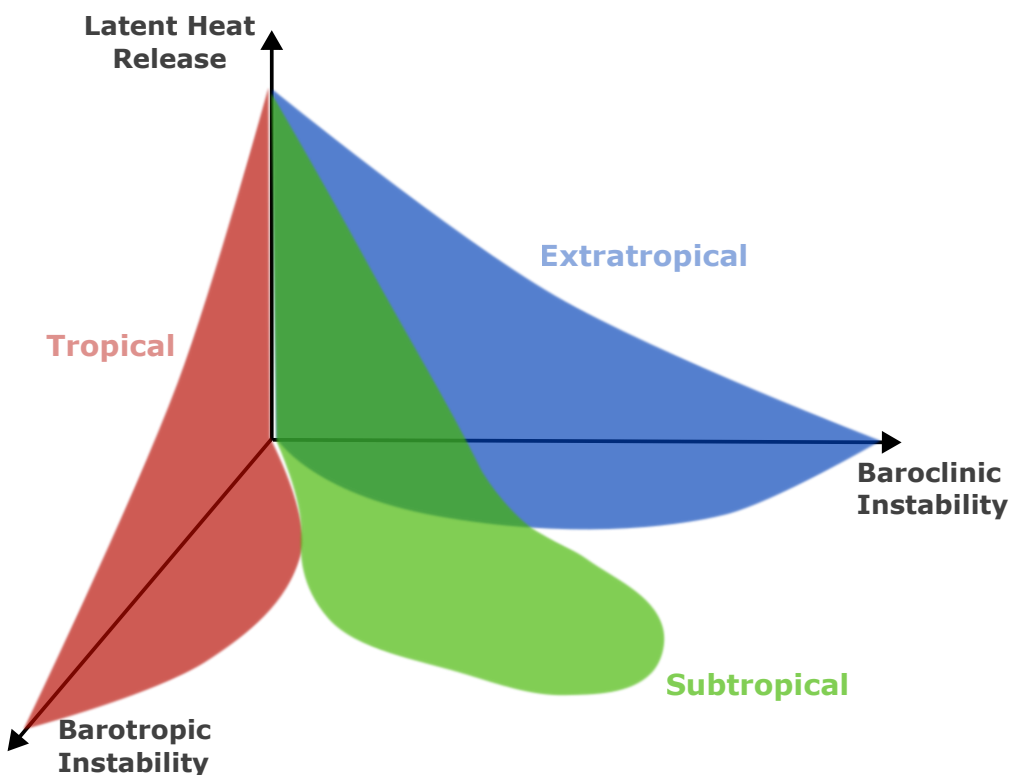


Figure 2.10: Proposed conceptual model correlating atmospheric destabilization mechanisms with cyclone types. Each axis within the three-dimensional schema represents a different process of atmospheric destabilization, allowing the categorization of cyclone types across the spectrum. Adapted from Silva Dias et al. (2004).

2.1.4 Final Causes

Final causes delve into the purpose or ultimate reason for the existence of something, offering insights into the "why" behind its occurrence. For instance, the final cause of a table is to serve as a platform for activities such as writing, eating, or working. When considering cyclones, their final cause could be viewed as the facilitation of heat and

moisture redistribution within the atmosphere, thus playing a crucial role in maintaining global climatic equilibrium and acting as a mechanism for dissipating excess heat.

The Earth's climate system is fundamentally driven by solar radiation, while simultaneously losing heat through infrared radiation emitted into space. The unequal distribution of solar radiation, exacerbated by the tilt of the Earth's axis, results in energy surpluses in equatorial regions and deficits in polar areas. This differential heating prompts the formation of warm air masses near the equator and cold air masses in polar regions, instigating atmospheric circulation as an effort to achieve thermal equilibrium, a state that remains elusive due to ongoing differential heating between tropical and polar zones.

Historical and recent advancements in atmospheric science have underscored the significance of general atmospheric circulation in climate dynamics (Lorenz, 1967; Hadley, 1735; Stull, 2015; Schneider, 2006). The Hadley Cell emerges as a critical response to the disparity in solar radiation received at the equator compared to the poles (Figure 2.11). Warmed air rises near the equator, creating low-pressure zones at the surface and high pressure aloft. This ascending air, replaced by cooler air from higher latitudes, moves poleward at elevated altitudes due to mass conservation. The conservation of angular momentum is crucial as this air, moving away from the equator (where surface rotational speed is maximum), must increase its eastward velocity as it approaches the poles. This dynamic leads to the formation of subtropical jet streams around 30° latitude. The Polar Cell, integral to high-latitude atmospheric circulation, is driven by the thermal contrast between the poles and regions at 60° latitude. This temperature difference induces opposing north-south pressure gradients, generating equatorward winds that, due to the Coriolis force, become polar easterlies. At higher levels, winds flow poleward but are deflected eastward, forming an upper-level westerly flow around the polar low, thus completing the Polar Cell circulation.

Together, the Hadley and Polar Cells underscore a comprehensive circulation pattern that transports warm air and angular momentum from the equator towards the poles and vice versa, facilitating Earth's energy balance. Although initially conceptualized as symmetrical circulations extending from the equator to the poles, subsequent research has emphasized the pivotal role of large-scale eddies in heat and angular momentum transfer (Schneider, 2006). These eddies, critical to atmospheric dynamics, emerge due to baroclinic zones in mid-latitudes and are intrinsic to the structure and function of the Ferrel Cell in

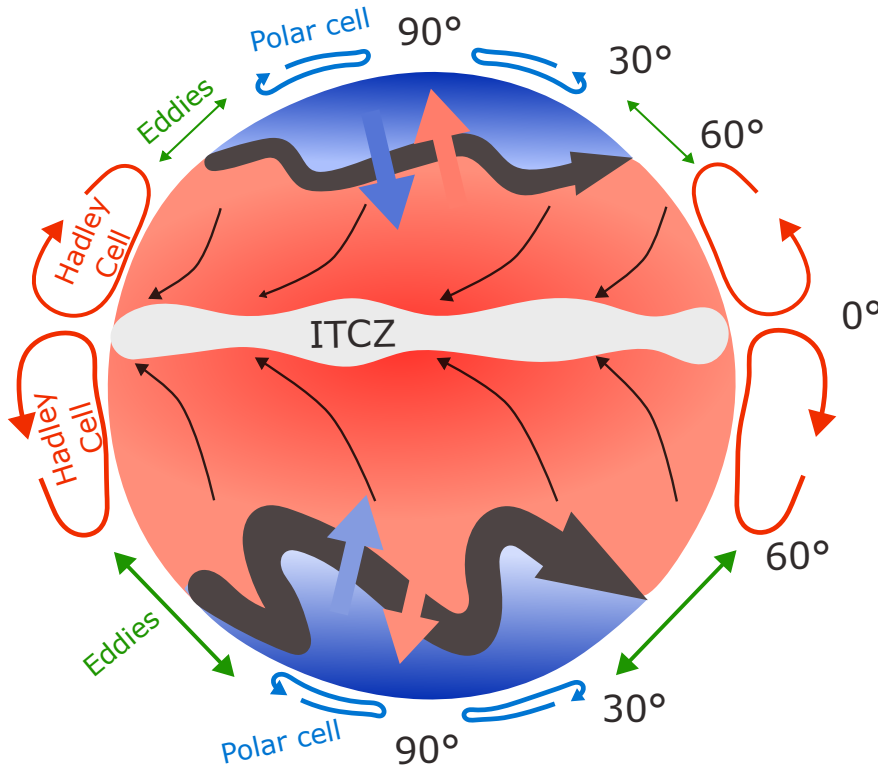


Figure 2.11: Representation of the global circulation pattern, showing the Hadley Cell circulation prominent at low latitudes, the transport of momentum and heat by eddies at mid-latitudes, and the polar cell circulation at high latitudes. Inspired by Stull (2015).

mid-latitudes(Held, 1999; Schneider, 2006). Arising from mid-latitude baroclinic zones, they are indispensable to the Ferrel Cell’s operation, influencing wind patterns across latitudes and enhancing heat transfer between the tropics and poles (Stull, 2015; Held, 1999).

Due to their relatively small scale compared to extratropical cyclones, tropical cyclones are not directly associated with the three-cell model of global circulation. They arise in regions of low baroclinicity, where thermal contrasts are minimal, relying instead on the atmosphere’s ability to generate energy from internal heat sources. These sources are largely the warm temperatures of tropical oceans and the air above them (Palmén and Newton, 1969). Often conceptualized as a Carnot heat engine (Figure 2.12), tropical cyclones draw heat from the ocean surface—primarily through the latent heat of vaporization—and release it into space via longwave radiation (Emanuel, 1987; Ozawa and Shimokawa, 2015; Wang et al., 2022, e.g.,). The cyclone’s intensity depends on the efficiency of this heat engine, which is determined by the temperature difference between the heat source (ocean)

and sink (upper atmosphere). Friction, especially near the ocean surface within the boundary layer, plays a crucial role by causing energy loss that can lessen wind speeds and alter angular momentum, impacting the cyclone's energy conversion efficiency.

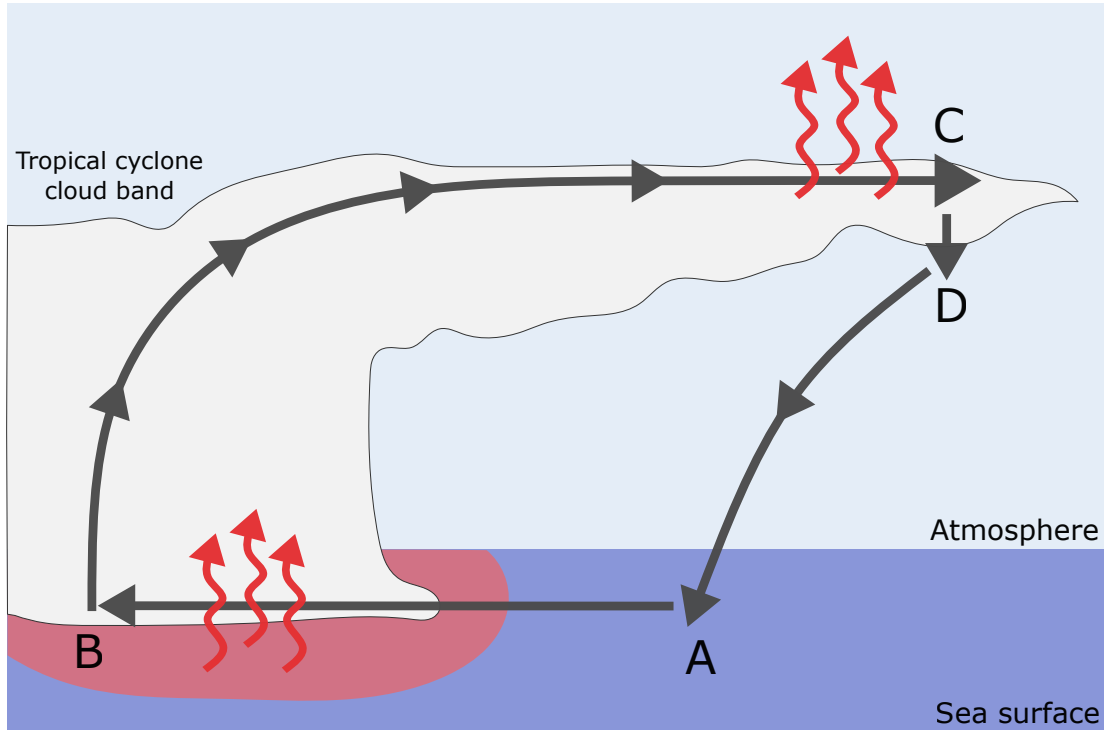


Figure 2.12: Diagrammatic Representation of a Tropical Cyclone as a Carnot Heat Engine. The process begins with isothermal inflow (A-B) at the surface, drawing energy from warm ocean waters into the cyclone's core. This stage is succeeded by the upward movement of air (convection) and outward flow just below the tropopause, characterized by radiative cooling and energy loss (B-C). Subsequently, cooled air descends away from the cyclone's center (C-D) and cycles back towards the cyclone, completing the circuit (D-A). Adaptation based on the COMET Program.

We can see then that tropical cyclones serve to dissipate excess heat in the tropics, utilizing oceanic heat to fuel the system while dissipating energy through radiation at the upper levels or friction at the surface. Given this model's applicability, Emanuel (1987) predicted that rising atmospheric CO_2 levels would lead to more intense tropical cyclones in the future. Recent climate models suggest an increase in tropical cyclone intensity, though there's no global consensus on frequency changes (Knutson et al., 2010; Walsh, 2004; Walsh et al., 2016, 2019). As discussed in Section 2.1.3, understanding tropical cyclone development remains a significant scientific endeavor, complicating precise predictions of their response to climate change and their regulatory effect on climate.

In exploring subtropical cyclones, much remains to be discovered. The global distribu-

tion of cyclonic activity exhibits a bimodal pattern, with tropical cyclones forming in tropical regions and extratropical cyclones in mid-latitudes, leaving subtropical areas relatively calm in terms of cyclonic development (Yanase et al., 2014). It's speculative—emphasis on "speculate"—to suggest that subtropical systems share the final causes of their tropical and extratropical counterparts, acting to erase thermal gradients by redistributing heat globally or dissipating excess heat. However, subtropical cyclones might perform these functions under hybrid environmental conditions, possibly moderating gradients in regions with an abundance of heat. Ongoing research into subtropical cyclones promises to provide further clarity on their impact on global circulation patterns and their role within the broader climatic system.

2.1.5 Summary

This section has explored the Aristotelian causes as they pertain to cyclones, comparing the various types—extratropical, tropical, and subtropical—while also acknowledging the existence of other cyclonic phenomena like warm seclusions and polar lows. For succinctness, the discussion primarily centered on the main types, suggesting that cyclonic systems form a continuum: extratropical systems at one end, tropical cyclones at the other, and subtropical systems exhibiting hybrid characteristics.

Initially, we discussed that cyclones' material causes are linked to the air masses constituting them. Extratropical cyclones are associated with cold cores throughout the troposphere, whereas tropical cyclones are characterized by warm cores. Subtropical cyclones, however, display warm cores at the surface and cold cores at higher tropospheric levels.

Regarding formal causes, the cyclones differ in structure. Extratropical cyclones, identified by their frontal features, show asymmetry. Tropical cyclones, described as symmetric, feature convection bands spiraling the central eye. Subtropical cyclones, meanwhile, may present a range of spatial configurations, neither fully asymmetric nor symmetric.

Efficient causes, the dynamic mechanisms behind cyclone development, vary. Extratropical cyclones are primarily driven by baroclinic instability, a comprehensive mechanism underlying their formation. Tropical cyclone genesis and intensification lack a unified theoretical model, with current theories suggesting that barotropic instability in tropical waves—coupled with diabatic processes like latent heat release—might describe their development. Subtropical systems, given the incipient state of research, are speculatively

linked by the author to both baroclinic and barotropic instabilities, with diabatic heat playing a role.

The final causes reflect cyclones' contributions to global circulation. Extratropical cyclones are recognized for redistributing heat, mitigating temperature gradients in mid-latitudes. Tropical cyclones, functioning as thermal engines, dissipate excess heat in tropical regions. The role of subtropical cyclones in the climate system remains speculative; they are hypothesized to simultaneously embody the functions of the other two types.

One important feature noted is that most classifications adopted for cyclone classification are based on Hart (2003) diagrams that objectively distinguishes these systems based on their material and formal causes. Although much knowledge exists regarding the efficient and final causes of tropical and especially extratropical systems, such objective criterion for these causes is still lacking. The current research proposes such objective classification procedure in the hopes of aiding the investigation of such causes related to cyclonic systems.

A notable point is the reliance on Hart (2003)'s diagrams for cyclone classification, objectively differentiating systems by their material and formal causes. While extensive knowledge exists on the efficient and final causes of tropical and particularly extratropical systems, a clear criterion for these causes is absent. This work proposes an objective classification procedure to aid in investigating cyclonic systems' related causes.

2.2 *Cyclones in South America*

This section transitions to examining cyclonic phenomena within South America, with a particular emphasis on systems originating in or adjacent to this region. While previous sections have provided a comprehensive overview of various cyclone categories, their structures, formation mechanisms, and roles in atmospheric circulation, here we delve into cyclonic systems that have genesis in South America or its neighboring oceanic regions. Although systems originating along the western coast of South America are noted (Crespo et al., 2023, e.g.), our primary focus is on cyclones forming in the southern and eastern sectors of South America and the Southeastern Atlantic region. These systems significantly influence the regional climate, particularly in South and Southeastern Brazil (de Souza et al., 2022; Reboita et al., 2010, e.g.), and can cause extreme weather events (Cardoso

et al., 2022; de Souza and da Silva, 2021; Gramcianinov et al., 2020, e.g.). From this point on, we refer to this region encompassing the Southeastern Atlantic and the adjacent South American region as SESA.

2.2.1 Climatological aspects

The first cyclone climatology for SESA region was performed by Gan and Rao (1991), utilizing sea level pressure data from surface charts spanning a decade. Despite methodological constraints, the authors identified two primary cyclogenesis regions: one over Uruguay and another in Southeast Argentina, with the latter being more active in austral summer and the former in winter. They hypothesized that the cyclogenesis in these regions was driven by baroclinic instability of the westerlies and lee cyclogenesis—cyclogenesis influenced by the interaction between baroclinic disturbances and topography (Gan and Rao, 1994; Tibaldi et al., 1980).

Later studies, employing automated techniques to detect cyclones' minimum central pressure, validated the cyclogenesis regions identified by Gan and Rao (1991) (Simmonds and Murray, 1999; Simmonds and Keay, 2000; Mendes et al., 2010). Meanwhile, analyses based on relative vorticity fields, as opposed to minimum central pressure, found a third significant cyclogenesis area near Southeast Brazil (Hoskins and Hodges, 2005; Sinclair, 1995; Reboita et al., 2010; Gramcianinov et al., 2019). The shift towards relative vorticity for cyclone tracking, as discussed by Hoskins and Hodges (2002); Sinclair (1994), offers several technical advantages. In mid-latitudes, the background pressure gradient's intensity can foreshadow closed isobars in developing cyclones, making it challenging to detect cyclones until they intensify or reach higher latitudes. Thus, employing relative vorticity enables the identification of weaker and faster-moving systems, as well as cyclones in their nascent stages, when closed isobars might not yet be evident.

In the SESA region, previous research has successfully identified three key areas of cyclogenesis, and this current study will adopt the nomenclature established by Gramcianinov et al. (2019) for consistency and clarity. The ARG region, situated in Southeast Argentina, emerges as the most active, with a relatively steady cyclogenesis rate throughout the year, though it peaks during the austral summer (Crespo et al., 2021; Gramcianinov et al., 2019; Reboita et al., 2010). The LA-PLATA region, over the La Plata River basin, ranks second in genesis density, displaying heightened activity in the austral winter (Crespo et al., 2021;

Gramcianinov et al., 2019; Reboita et al., 2010). It's noteworthy that Reboita et al. (2010) identified the LA-PLATA region along the Uruguayan coast rather than over the continent, influenced by the application of a continental mask in cyclone tracking, which biases detection towards maritime regions. The final region, SE-BR, located near the Southeastern Brazilian coast, records the fewest genesis events, with a significant increase in activity during the austral summer compared to winter (Reboita et al., 2010; Gramcianinov et al., 2019; Crespo et al., 2021). Figure 2.13 summarises these findings.

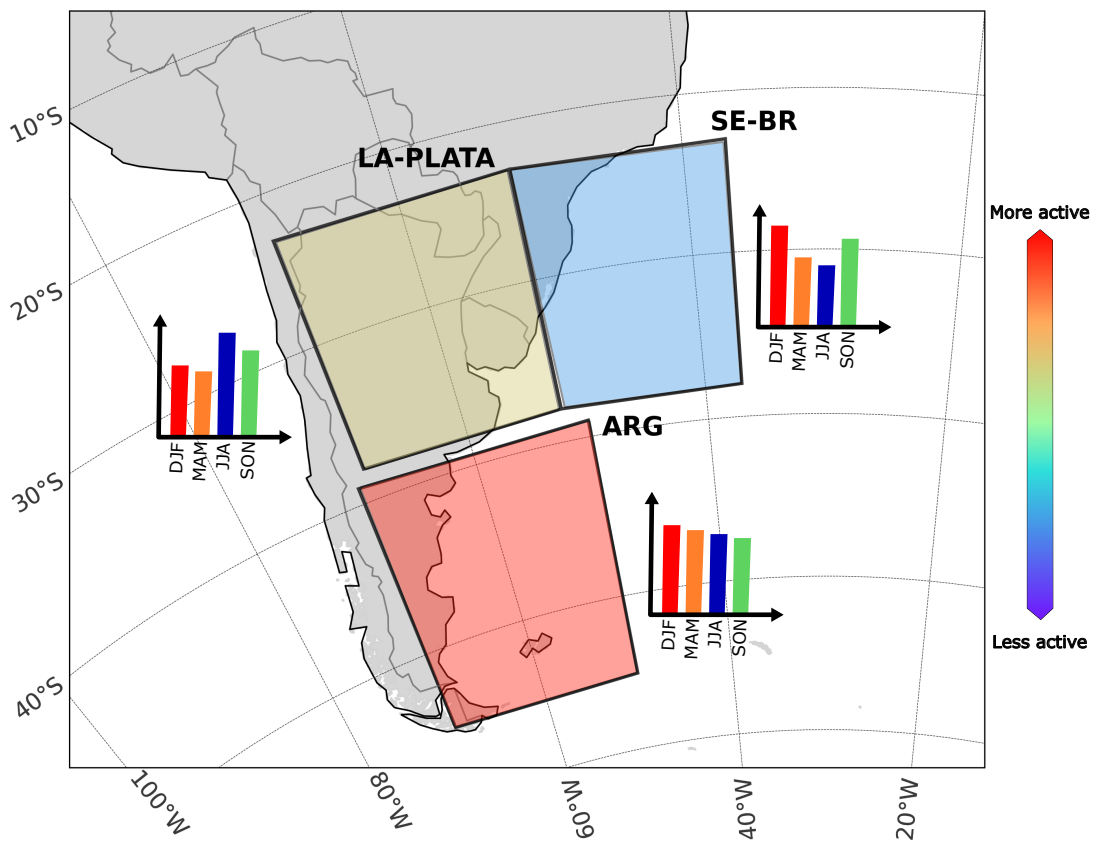


Figure 2.13: Illustrative mapping of cyclogenesis activity within the South American/Southeastern Atlantic (SESA) region, categorized into three primary genesis areas: ARG (Southeast Argentina), LA-PLATA (La Plata River basin), and SE-BR (Southeastern Brazilian coast). The diagram highlights the cyclogenesis frequency and seasonal patterns in each region, with a visual scale indicating activity levels from more active to less active.

2.2.2 Genesis mechanisms

The majority of systems in SESA region are extratropical (Marrafon et al., 2022), thus baroclinic instability serves as the primary genesis mechanism across all regions, as

discussed in Section 2.1.3. However, each region is also influenced by secondary mechanisms. Notably, all regions lie on the lee side of the Andes, where baroclinic development of troughs crossing the mountain range can prompt surface cyclogenesis (Gan and Rao, 1994; Vera et al., 2002; Hoskins and Hodges, 2005; Gramcianinov et al., 2019). Additionally, downstream development, marked by system decay on the Andes' upslope and regeneration on the downslope facilitated by vortex stretching over the mountain barrier, is observed (Hoskins and Hodges, 2005).

Subsequent analyses by Gramcianinov et al. (2019) and Crespo et al. (2021) delve into the specific genesis mechanisms for each cyclogenesis region. Their findings, synthesized in this section, compare summer and winter mechanisms, as transitional seasons typically exhibit intermediate characteristics (Gan and Rao, 1991; Hoskins and Hodges, 2005; Gramcianinov et al., 2019; Crespo et al., 2021).

In both seasons, cyclones in ARG region tend to follow a traditional baroclinic development pathway, heavily influenced by low level cold advection (Gramcianinov et al., 2019). This advection is crucial in reducing static stability, due to the contrast between the warmer surface and cold air aloft, thereby facilitating cyclogenesis. The cyclogenesis position relative to the jet stream provides upper-level support, either at the poleward exit during summer or the equatorward entrance during winter (Crespo et al., 2021). During summer, a slightly more baroclinic environment and more pronounced potential vorticity anomalies promote conditions favorable for ascending vertical movements (Crespo et al., 2021).

Cyclone development in the LA-PLATA region is initially driven by moisture transport from the South American low-level jet on the eastern slope of the Andes and from the South Atlantic Subtropical High towards the southeastern coast (Gramcianinov et al., 2019). This transport feeds cyclone development with warm, moist air, promoting low-level instability. Furthermore, cyclogenesis in this region is influenced by potential vorticity anomalies in both summer and winter (Crespo et al., 2021). The area is positioned beneath the equatorial entrance of a jet streak in both seasons, with a slightly more pronounced baroclinic environment in winter (Crespo et al., 2021).

During summer, cyclogenesis in the SE-BR region is significantly influenced by the transport of warm and moist air from the tropics, associated with the South Atlantic Convergence Zone (SACZ) (Gramcianinov et al., 2019). This process contributes to cyclo-

genesis through diabatic heating and convective processes. In winter, upper-level forcing becomes more prominent, with baroclinic conditions intensified by the presence of strong temperature gradients and jet stream dynamics (Gramcianinov et al., 2019). Moreover, during summer, cyclogenesis occurs in a more barotropic environment, with the jet stream significantly displaced from the genesis region, and is highly influenced by high-level potential vorticity anomalies (Crespo et al., 2021). Conversely, in winter, cyclogenesis occurs beneath the equatorial entrance of a jet streak in a more baroclinic environment compared to summer, influenced by low-level potential vorticity anomalies (Crespo et al., 2021).

2.2.3 Subtropical cyclones

It was only after Hart (2003) work that the scientific community started to take a closer look to subtropical cyclones. It wasn't until about 20 years ago that the first detailed climatology for subtropical cyclones in the South Atlantic was conducted by Evans and Hart (2003). This study uncovered an average occurrence of roughly one subtropical cyclone per year in the region, with a relatively uniform distribution across seasons. Notably, subtropical cyclogenesis was found to occur in diverse environments: genesis in the open ocean primarily involves Rossby wave breaking, similar to systems in the North Atlantic, whereas coastal genesis is often related to lee cyclogenesis, influenced by the warmer sea surface temperatures of the Brazilian Current, which create conducive conditions for subtropical cyclone formation.

More recently, Gozzo et al. (2014) introduced modifications to the criteria used by Evans and Hart (2003), aiming to capture weaker and shallower systems in their analysis. This adjustment led to the identification of an average of 7 cyclones per year, a significant increase from the findings of the previous study. Gozzo et al. (2014) emphasized the subtropical cyclones' lower traveled distance and displacement speed compared to their extratropical counterparts, allowing them more time to interact with the unstable conditions that facilitated their genesis and to exert greater impact on the South American coastal zone.

Moreover, Gozzo et al. (2014) noted distinctions in seasonal activity, with a peak during summer but stronger systems occurring in autumn. The Southeastern Brazil region (SE-BR) emerged as the predominant genesis area, with over a third of the cyclones developing there exhibiting hybrid characteristics. These systems typically originate from upper-level

potential vorticity anomalies and divergence within a low-shear environment. At lower levels, warm and moist air advection, primarily from the subtropical high, is crucial for their formation. During summer, an additional moisture source from the tropics is also significant. Also, the authors used numerical simulation for demonstrating the importance of local latent heat fluxes for the systems development.

Gozzo et al. (2017) reinforced the findings of Gozzo et al. (2014), confirming the role of moisture fluxes in the formation of subtropical cyclones in the SE-BR region. They highlighted that moisture transport from the subtropical high is particularly crucial during the summer months when it shifts closer to the Brazilian southeastern coast. The reduced number of genesis events observed in the winter can be attributed to the diminished strength of this moisture transport. In contrast, during autumn, transient high-pressure systems serve as the primary source of moisture. Moreover, through numerical simulations, the authors demonstrated the significance of local latent heat fluxes in the development of these systems.

Subtropical cyclones in the South Atlantic remain an area ripe for exploration due to their relatively sparse coverage in scientific literature. From the limited climatologies available, and the few study cases (Reboita et al., 2018, 2022; Dias Pinto and Rocha, 2011, e.g.) it is evident that the formation of these systems is closely linked to Rossby wave breaking and are fueled by both local and non-local latent heat fluxes. However, the door remains open for more comprehensive studies to explore the their dynamics, climatological impacts, and the potential influence of broader atmospheric and oceanic processes on their formation.

2.2.4 Tropical cyclones

Historically, it was believed that the SESA was not conducive to Tropical Cyclone formation due to insufficiently high sea-surface temperatures and relatively strong vertical wind shear, a perspective dating back to Gray (1968), which identified the South Atlantic as the sole oceanic basin without such systems. This view was upended by Hurricane Catarina in 2004, the first recorded hurricane in the South Atlantic, challenging previous assumptions despite some evidence of weak tropical cyclones in the region before the satellite era (da Silva Dias et al., 2004).

Catarina, which originated from an extratropical system near the southeastern Brazi-

lian coast, underwent a tropical transition and made landfall in Southern Brazil (Pezza and Simmonds, 2005). The system's trajectory and development were significantly influenced by unique environmental conditions, including a dipole-blocking pattern in the upper atmosphere, guiding the system back toward Brazil over relatively cool sea surface temperatures (SSTs) of around 25°C (McTaggart-Cowan et al., 2006). This development over cooler SSTs was facilitated by a unique combination of extreme blocking conditions, low wind shear favored by an extreme positive phase of the Southern Annular Mode (Pezza and Simmonds, 2005; Pezza et al., 2009), and latent heat release from air-sea interactions. Strong interactions with sub-superficial warm waters by Ekman pumping led to the upwelling of isotherms and mixed layer waters, allowing for a significant air-sea temperature gradient and vigorous heat exchange between the ocean and atmosphere, fueling the system through latent heat release (Vianna et al., 2010; Pereira Filho et al., 2010).

Hurricane Catarina, while a landmark event, did not originate from a purely tropical process; it was a baroclinic cyclone that underwent tropical transition. This distinction was pivotal until the emergence of a system near Brazil's Northeast oceanic region in 2019, reported as the first instance of pure tropical cyclogenesis in the South Atlantic. This system, named Iba, marked a significant departure from previous understandings of cyclonic activity in the region (Reboita et al., 2021). Additionally, research on subtropical cyclone Anita in March 2010 suggested its potential for tropical transition under warmer sea surface conditions and without interference from a neighboring extratropical cyclone (Dias Pinto and Rocha, 2011; Reboita et al., 2019). In March 2024, another system named Akará, originating near Southeastern Brazil and featuring eye-like characteristics and a symmetric form, ignited discussions regarding its potential classification as a tropical cyclone, although a detailed examination of its characteristics is pending.

The sporadic nature of these systems in the SESA region precludes the formation of a comprehensive tropical cyclone climatology. While there is some conjecture about the influence of climate change on the emergence of these systems (Pezza and Simmonds, 2005; McTaggart-Cowan et al., 2006; Pezza et al., 2009; Pereira Filho et al., 2010, e.g.), establishing a direct connection between recent tropical cyclone occurrences in SESA and global climatic shifts remains elusive. The rarity of such events continues to challenge researchers, suggesting a complex interaction between regional climatic conditions and broader atmospheric patterns influenced by climate change.

2.3 Life cycle of extratropical cyclones: objective classification procedures

This section explores lifecycle and classification procedures for extratropical cyclones, building upon conceptual models and evolution patterns discussed in Sections 2.1.2 and 2.1.3. These models, derived from case studies and numerical simulations, seek to generalize cyclone development phases due to the absence of standardized methods for analyzing distinct lifecycle stages across extensive datasets. Herein, we introduce an automated approach for detecting the lifecycle of cyclones, thereby advancing the discussion on objective classification methodologies for these atmospheric phenomena.

The Polar Front Theory, as detailed by Bjerknes and Solberg (1922), was among the first to describe the lifecycle of extratropical cyclones, delineating distinct phases based on structural transformations and large-scale dynamics. Nonetheless, Shapiro and Keyser (1990) later argued that not all cyclones adhere strictly to the progression outlined by Bjerknes, proposing an alternative model that complements the original theory. These developmental models, including their respective stages, are elaborated in Section 2.1.2 and illustrated in Figure 2.4. While these descriptions offer detailed insights into the structural changes cyclones undergo, they fall short of directly associating each phase with specific atmospheric variables in a way that allows for algorithmic detection and statistical and/or spatial analysis.

Whittaker and Horn (1984) conducted one of the earliest cyclone climatology studies, identifying cyclogenesis regions based on the formation of the first closed isobar. This definition has been widely used since (Gramcianinov et al., 2019; Trigo, 2006; Hoskins and Hodges, 2005; Simmonds and Keay, 2000, e.g.). Whittaker and Horn (1984) also defined cyclone intensification as the rate of sea level pressure deepening, a definition echoed and expanded upon by later studies through metrics like relative vorticity growth rate (Grise et al., 2013; Gramcianinov et al., 2019; Hoskins and Hodges, 2005) and the baroclinic Eady growth rate (Pinto et al., 2005). However, Whittaker's study lacked a comprehensive method for classifying cyclone evolution.

A classification of the developmental phases throughout the life cycle of cyclones was conducted by Evans and Hart (2003), with a particular focus on tropical cyclones undergoing extratropical transition. This study explored the structural evolution of such

systems, employing a classification framework grounded in the environmental parameters outlined by Hart (2003). The authors partitioned the life cycle of the cyclones into two main phases: one preceding and the other following the peak intensity of the tropical cyclone. This demarcation enabled a detailed analysis of the transformation these cyclones undergo from their genesis as tropical entities to their eventual extratropical characteristics.

Gray and Dacre (2006) implemented the classification scheme originally proposed by Deveson et al. (2002), as detailed in Section 2.1.3, to study the climatology of Northern Atlantic extratropical cyclones. Their analysis focused on the separation between the upper-level trough and the lower-level cyclone throughout the cyclones' intensification periods, which were identified when the cyclones' central relative vorticity surpassed a specified threshold. While this approach proved beneficial for classification purposes, it overlooked the exploration of dynamical forcing during the development of cyclones. Furthermore, the rationale behind the selected threshold value, including its potential applicability across various scenarios, remained unexplored.

Building upon the foundation laid by Gray and Dacre (2006), Dacre and Gray (2009) delved into the environmental forces influencing the evolution of different types of cyclones. To achieve a granular understanding of variations throughout the cyclones' life cycle, they segmented the cycle at the juncture of maximum relative vorticity. This segmentation delineated the period leading up to this juncture as the intensification stage and the subsequent period as the decaying stage. Additionally, by categorizing cyclones based on their overall lifespan, the study facilitated the identification of specific areas prone to cyclone intensification and the environmental characteristics predominant in those regions.

Rudeva and Gulev (2007) delved into the study of changes in the radius of cyclones throughout their life cycle, introducing the concept of "nondimensional cyclone lifetime." This methodology facilitates the comparison of different stages of cyclone development by normalizing their lifespan to a uniform scale, achieved by dividing the current time step within the system's life cycle by its total duration. Similar approaches were employed by Booth et al. (2018) and Schemm et al. (2018). Specifically, Booth et al. (2018) focused on analyzing precipitation rates through the cyclone life cycle, identifying the cyclones' peak dynamical strength with the point of maximum relative vorticity. Concurrently, Schemm et al. (2018) applied normalization to the cyclone life cycles using the duration from genesis to lysis, thereby examining the periods when the systems were associated with frontal

structures.

Trigo (2006) explored the spatial distribution of cyclogenesis (i.e., the initial detection point of each low-pressure system), cyclolysis (the final detected position), and the locations where these systems attained their minimum central pressure. Similarly, Bengtsson et al. (2009), albeit not explicitly defining developmental stages, observed distinguishable phases centered around the maximum intensity of the system, characterized as the period when maximum central relative vorticity is reached. Meanwhile, Azad and Sorteberg (2014a,b) dissected the cyclone life cycle into distinct stages, identifying the mature phase as the period during which geostrophic vorticity experiences its most rapid increase, with the incipient stage occurring beforehand. Moreover, they categorized the life cycle of a cyclone based on the maximum geostrophic vorticity attained; the time leading up to this peak is labeled as the intensification stage, while the subsequent period is known as the decaying stage.

The diverse methodologies highlighted in the literature offer a range of objective criteria for delineating the lifecycle of extratropical cyclones, each linked to the temporal dynamics of specific atmospheric variables. Commonly, cyclone genesis is identified at the algorithm's first detection, with intensification and decay phases typically defined by changes in central pressure or, when using relative vorticity for tracking, by the increase (intensification) or decrease (decay) of vorticity in the Northern Hemisphere. The peak of the system's intensity is often marked as the point of maturity, while lysis is recognized at the algorithm's final detection of the system. A schematic illustration of this lifecycle, emphasizing the use of relative vorticity at the 850 hPa isobaric level (ζ_{850}) for cyclone detection, is depicted in Figure 2.14.

Despite these advancements, several limitations persist in current approaches. First, the initial phase of cyclone development, where the system is present but not yet fully formed, is often overlooked. In such instances, a cyclone may exhibit closed central relative vorticity without corresponding closed isobars at sea level pressure (Sinclair, 1995, e.g.). Second, defining cyclone maturity as merely the point of maximum intensity overlooks the broader period during which atmospheric dynamics illustrates the cyclone's evolution. Finally, characterizing all stages between genesis and maturity as intensification, and those between maturity and lysis as decay, presupposes a singular, linear progression of these stages. This assumption fails to account for the potential complexity of cyclone lifecycle

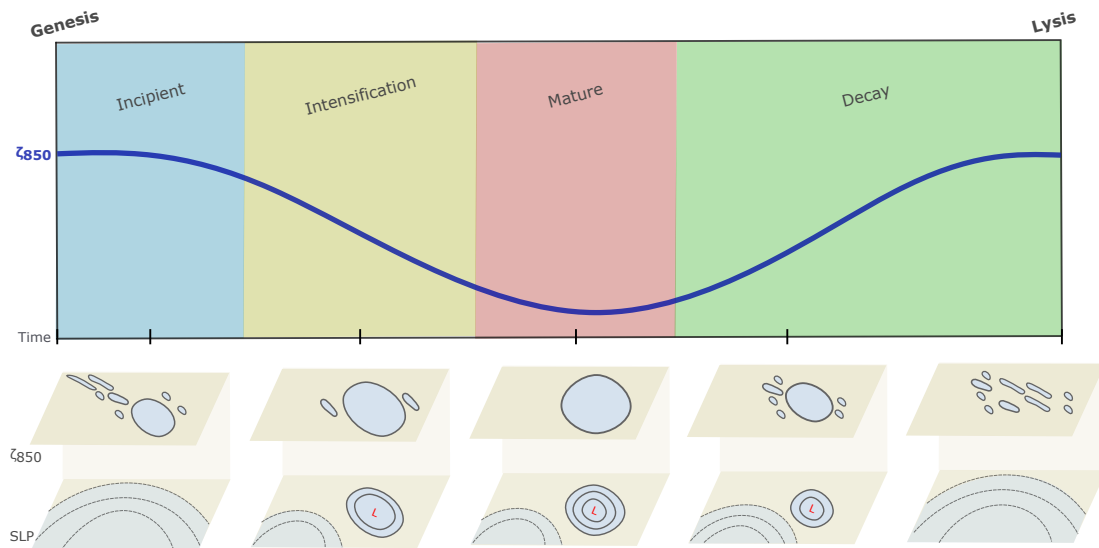


Figure 2.14: Schematic representation of an extratropical cyclone’s life cycle, depicted through the relative vorticity field at the 850 hPa isobaric level (ζ_{850}). The central figure displays the temporal progression of central ζ_{850} at the cyclone’s core across various phases. The bottom figures illustrate the evolution of the ζ_{850} field and sea level pressure (SLP) spatial distributions during each phase.

stages, including the possibility of multiple intensification and decay phases.

The ability to discern the distinct life cycle phases of cyclones is crucial for several reasons. As highlighted in Section 2.2, most climatologies currently focus on either the entirety of a cyclone’s life cycle or specific points, such as its genesis or lysis. Enhanced techniques for dissecting a cyclone’s life cycle could unlock the potential for more granular analyses of the processes and environmental dynamics associated with different stages of cyclone development. For example, while the initial baroclinicity associated with extratropical cyclones is well-documented, the environmental shifts that trigger their cessation of intensification remain less understood. Case studies have shed light on these aspects, but comprehensive testing under climatological conditions is yet to be conducted.

By identifying the environmental conditions pertinent to various stages of cyclone development, researchers can leverage climate change projections to assess potential future shifts in these conditions. Moreover, given the absence of a universally recognized conceptual model for tropical cyclone development, detailed climatological analyses of environmental parameters across distinct life cycle phases could offer critical insights toward establishing such a model. Thus, the potential applications of a refined procedure for analyzing cyclone life cycle phases are vast, limited only by the creativity and curiosity of

the research community. Such advancements would not only enhance our understanding of cyclone dynamics but also improve our ability to predict and respond to these powerful weather systems in the context of a changing climate.

2.4 Atmosphere Energetics

Solar radiation serves as the primary energy source within the Earth's system. Concurrently, the atmosphere globally dissipates heat by emitting infrared radiation into space. The tilt of the Earth's axis causes a significant variation in radiative incidence between the tropical and polar regions: tropical areas receive more solar energy than they emit, creating an energy surplus, whereas polar regions experience an energy deficit, losing more energy to space than they absorb. This differential heating leads to the formation of warm air masses in tropical regions and cold air masses in polar regions. The resulting heat imbalance drives atmospheric circulation, an ongoing process attempting to balance these temperature disparities. However, this equilibrium is never fully achieved due to the constant differential heating between the tropical and polar regions (Stull, 2015).

2.4.1 Lorenz Energy Cycle: Historical Background

The Lorenz Energy Cycle, introduced by Lorenz (1955), is a framework for understanding how energy is distributed and transformed within the atmosphere. This framework offers insights into the general circulation that shapes the dynamic and thermodynamic structures of the atmosphere, influencing atmospheric flows and the transport of heat, moisture, and angular momentum. In his groundbreaking work, Lorenz delineated a method to analyze atmospheric energetics by focusing on two primary forms of energy: kinetic energy (K) and available potential energy (APE), each further divided into zonal and eddy (turbulent) components. This section explores these energy forms and their interactions.

Lorenz argued that the total potential energy (P) of the atmosphere does not effectively represent the energy available for conversion into K to drive global circulation. To illustrate this concept, Lorenz proposed a thought experiment: Imagine the atmosphere is uniformly horizontally stratified; in such a scenario, despite the presence of P , the lack of horizontal gradients precludes air mass movement, resulting in no generation of K (Figure 2.15a). However, if part of the atmosphere is heated, it triggers vertical upward move-

ments, establishing pressure gradients and disrupting the horizontal stratification (Figure 2.15b). Conversely, cooling in a region induces similar effects but with vertical downward movements (Figure 2.15c). Both scenarios alter the P of the system, converting it into K. Yet, in the first case, P increases, while in the second, it decreases; that is, both increases and decreases of P are responsible for making energy available for atmospheric circulation.

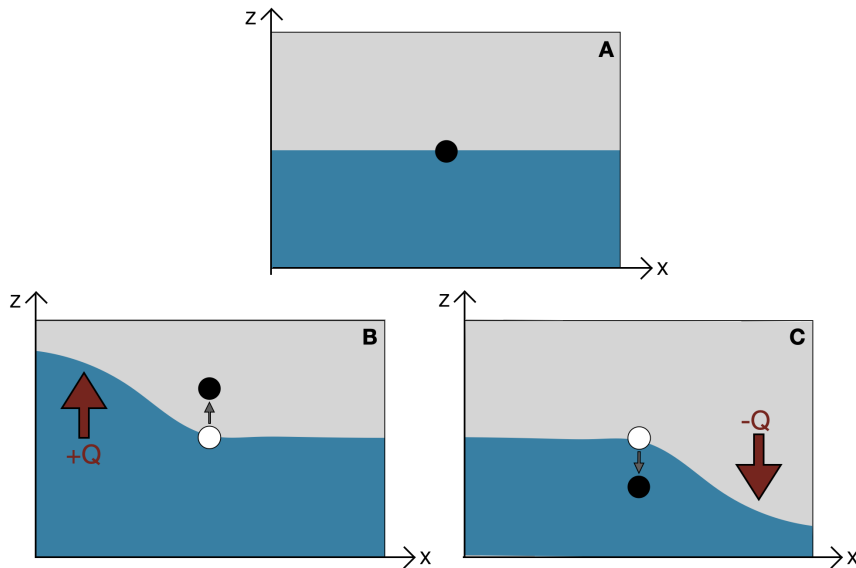


Figure 2.15: Mental experiment proposed by Lorenz (1955) to illustrate the relationship between total P and K, depicted through a two-layer atmospheric model: (A) Initially horizontally stratified atmosphere. (B) Perturbation caused by localized heating ($+Q$) leading to vertical upward movements. (C) Similar perturbation caused by cooling ($-Q$) resulting in vertical downward movements. Black circles represent the atmosphere's center of mass post-perturbation, and white circles indicate the center of mass prior to perturbation.

The concept of Available Potential Energy (APE) was initially proposed by Margules (1903), who was interested in the processes that generate kinetic energy (K) in storms (Marquet, 2017). To understand this concept, we can start from the same situation proposed by Lorenz (1955), where differential heating results in ascending movements and a heterogeneous distribution of mass in the atmosphere (Figure 2.16a). In this case, the resulting pressure gradients cause acceleration of the wind field (Figure 2.16b), redistributing the mass in the atmosphere. Assuming this flow is adiabatic, the final result is a horizontally stratified atmosphere (Figure 2.16c). In the first step, both forms of potential energy (total and available) are at their maximum. With the redistribution of mass, there is an increase in K, while the total and available potential energy decreases. In the final stage, P is minimal, yet not zero, while the APE is zero. Thus, APE can be defined as the

amount of potential energy available for conversion into K under an adiabatic distribution of mass.

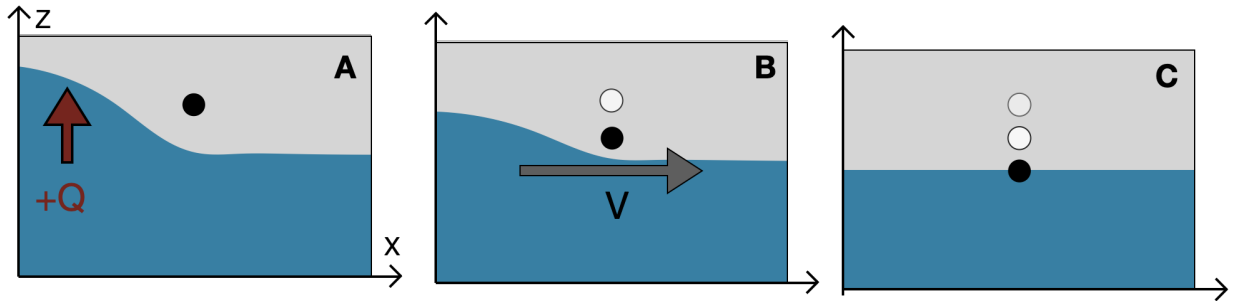


Figure 2.16: Depiction of Available Potential Energy (APE) transformations in response to atmospheric heating and cooling. (A) Initial state with differential heating causing heterogeneous mass distribution. (B) Redistribution of mass via wind fields leading to homogenization. (C) Final state of horizontal atmospheric stratification. Black circles indicate the center of mass at each stage, with white circles showing previous positions.

According to Lorenz (1955), APE serves as the primary source of K in the atmosphere, fundamentally driving the general circulation. While APE and K dominantly shape atmospheric dynamics, Lorenz acknowledged that diabatic processes and friction also play critical roles, though these elements were less detailed in his work due to their complex nature and the challenges associated with their quantification. In his theoretical framework, Lorenz treated the atmosphere as a closed system, distinguishing between the zonal and eddy (turbulent) components of APE and K to clarify the energetics involved in atmospheric processes.

This distinction is crucial as it aligns with earlier observations by Starr (1953), who emphasized the significance of eddies in maintaining atmospheric circulation, particularly their role in transferring K from turbulent to zonal flows. This perspective challenged earlier assumptions and highlighted the necessity of including eddy dynamics in any comprehensive atmospheric circulation theory. Subsequent research by Wiin-Nielsen et al. (1963) demonstrated the importance of eddies in global heat and momentum transport, illustrating how different wave numbers contribute to these processes. Through these insights, Lorenz's separation of energy components facilitates a deeper understanding of how meteorological systems, such as cyclones, develop and influence broader atmospheric circulation patterns.

The energy cycle can be represented by the following equations, which represent the

energy balance for each component of the cycle:

$$\frac{\partial A_Z}{\partial t} = -C_Z - C_A + G_Z \quad (2.6)$$

$$\frac{\partial A_E}{\partial t} = -C_E + C_A + G_E \quad (2.7)$$

$$\frac{\partial K_Z}{\partial t} = C_Z - C_K - D_Z \quad (2.8)$$

$$\frac{\partial K_E}{\partial t} = C_E + C_K - D_E \quad (2.9)$$

In these equations, available potential energy (APE) is divided into zonal (A_Z) and eddy (A_E) components, as is kinetic energy (K_Z and K_E , respectively). The transformations between these forms of energy are denoted by C , with subscripts Z and E for conversions between zonal and eddy forms, and A and K indicating conversions between APE and kinetic energy, respectively. Thus, C_A represents the conversion between A_Z and A_E , C_E denotes the conversion from A_E to K_E , C_K signifies the transformation from K_E to K_Z , and C_Z describes the conversion from A_Z to K_Z . Generation of APE and dissipation of kinetic energy are indicated by G and D , with G_Z and G_E marking the generation of A_Z and A_E , and D_Z and D_E representing the dissipation of K_Z and K_E , respectively. Full mathematical formulations for these processes are discussed in Section 2.4.2.

After the seminal work by Lorenz (1955) on the global energy cycle, numerous subsequent studies aimed to quantify this cycle, primarily focusing on the Northern Hemisphere due to observational constraints at the time (Starr, 1959; Saltzman and Fleisher, 1961; Holopainen, 1964; Jensen, 1961; Brown Jr, 1964; Wiin-Nielsen, 1959, e.g.). Oort (1964) synthesized these results to depict the annual energy cycle of the Northern Hemisphere. He innovatively categorized the energy analysis into distinct domains: the spatial domain, where variables are analyzed based on spatial averages, aiding in the understanding of large-scale zonal patterns such as jet streams and westerlies; the temporal domain, focusing on averages and deviations over time, which facilitates insights into long-term trends and transient disturbances; and the mixed space-time domain, which offers an integrated perspective on how average states and disturbances, both transient and stationary, interact and are sustained. Oort noted that while there was considerable focus on spatial domain analyses, studies addressing the mixed domain were scarce, and those considering the temporal domain were virtually absent.

From these estimates, Oort (1964) presented a diagram that visually encapsulates the energy cycle (Figure 2.17). This diagram illustrates the generation, conversion, and dissipation of different energy forms, providing a dynamic overview in a graphical format. Notably, the diagram allows for straightforward comparisons of diverse study results. It is important to mention, as Oort (1964) did, that friction terms are typically calculated as residuals due to the challenges in direct computation, balancing the zonal and turbulent terms of kinetic energy.

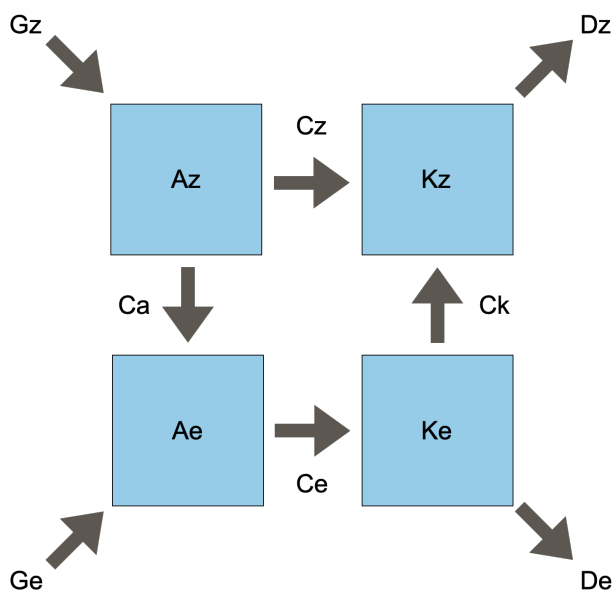


Figure 2.17: Representation of the energy cycle as formulated by Lorenz (1955) and schematized by Oort (1964). This diagram displays the interplay among the four forms of energy (zonal and turbulent terms of K and APE), illustrating their conversions, generation, and dissipation.

As previously mentioned, the formulation proposed by Lorenz (1955) estimates the energetics of the atmosphere assuming a closed system, that is, without energy exchanges at the boundaries. The first study to consider energetics for an open system was by Reed et al. (1963), which analyzed a sudden stratospheric warming event in the Northern Hemisphere. This study treated the stratosphere as an open system, permitting energy exchanges with other atmospheric layers, such as the troposphere. Building on this, Muench (1965), who was interested in stratospheric dynamics, refined Lorenz (1955)'s theory and proposed a new representation of the energy cycle.

Muench's model adds boundary flow terms (BA_Z , BA_E , BK_Z , and BK_E) to the original Lorenz equations, representing respectively the zonal and eddy flows of APE and K

across the system boundaries (Figure 2.18). The updated energy balance equations are:

$$\frac{\partial A_Z}{\partial t} = BA_Z - C_Z - C_A + G_Z \quad (2.10)$$

$$\frac{\partial A_E}{\partial t} = BA_E - C_E + C_A + G_E \quad (2.11)$$

$$\frac{\partial K_Z}{\partial t} = BK_Z + C_Z - C_K + B\Phi_Z - D_Z \quad (2.12)$$

$$\frac{\partial K_E}{\partial t} = BK_E + C_E + C_K + B\Phi_E - D_E \quad (2.13)$$

Where BA_Z , BA_E , BK_Z , and BK_E represent, respectively, the flows of zonal and eddy APE and K across the boundaries. The terms $B\Phi_Z$ and $B\Phi_E$ are represented together with the terms C_Z and C_E , respectively, because both arise from the same process of deriving the balances of K_Z and K_E . Muench (1965) recognizes the difficulty in interpreting the terms $B\Phi_Z$ and $B\Phi_E$, indicating that they are related to the flow of kinetic energy towards lower altitudes, representing the emergence of kinetic energy at the boundaries of the computational domain.

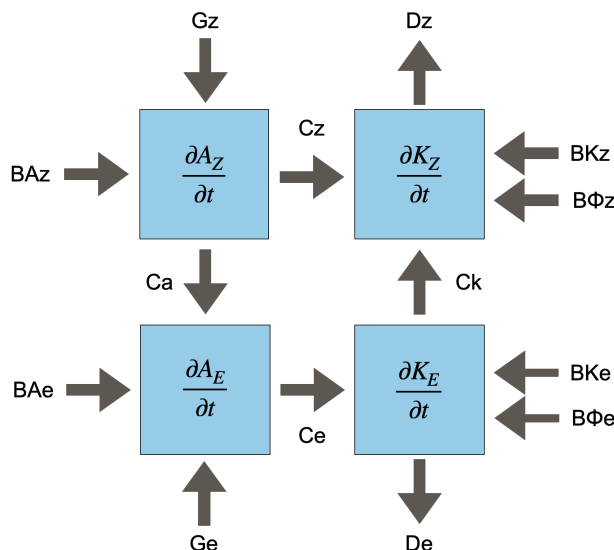


Figure 2.18: Energy cycle as formulated by Lorenz (1955) and updated by Muench (1965). This diagram includes additional terms representing energy flows across boundaries, illustrating both the local derivatives of the zonal and eddy partitions of APE and K and the interactions at the system edges.

Although Muench's model considers boundary flows, his domain was partially open, extending up to the polar regions and encompassing the entire Northern Hemisphere longitudinally, with the only boundary at the southern part of the domain at 30°N. The notion

of a fully regional energy cycle was later approached by Smith (1969), who aimed to assess the contribution of a limited region to global energetics. Smith clarified that while his work presented a framework for regional analysis, an exact computation of local energetics was outside its scope, and his model did not differentiate between zonal and eddy components of APE and K.

Parallel to the work by Smith (1969), Johnson (1970), following the theoretical framework proposed by Dutton and Johnson (1967), introduced a semi-Lagrangian framework for analyzing the energy cycle of limited areas. In this formulation, the delineated area for performing energetic calculations moves with the meteorological system of interest, spanning N fixed regions that shift in space. This analysis highlights that global Available Potential Energy (APE) is the aggregate of all possible open atmospheric regions, plus a term representing the thermodynamic contrast among these regions. It's crucial to note that Smith (1969) and Dutton and Johnson (1967) argued that the APE of a limited region should be viewed as its contribution to the global energetics rather than a standalone quantity. This perspective stems from the interconnected nature of the atmosphere, where local and global energetics are mutually influential.

Dutton and Johnson (1967) also critiqued Lorenz (1955)'s formulation, pointing out its underestimation of APE, particularly during the winter months. The alternative set of equations introduced by Johnson (1970), which utilizes isentropic coordinates, however, included simplifications that were seen as limitations by Vincent and Chang (1973), such as neglecting the impact of diabatic heating, rendering it impractical for diagnostic applications. Following this rationale, Vincent and Chang (1973) developed a system of equations in isobaric coordinates that account for the balances of APE and Kinetic Energy (K) in an open atmospheric system from a semi-Lagrangian perspective.

This formulation partitions APE into the reference state APE of the region and two components representing barotropic and baroclinic contributions to the APE of the delineated area. The balance equations for APE now included terms for boundary movement in the semi-Lagrangian frame and the advection of air masses with varying properties across these boundaries. This formulation was first applied by Edmon and Vincent (1979) in an energy cycle analysis of Hurricane Carmen (1974). Building on this, Brennan and Vincent (1980) adapted Vincent's approach to incorporate zonal and eddy components of APE and K, marking the first instance of such a detailed and realistic equation set being applied

to a limited area within the troposphere. However, Brennan and Vincent (1980) utilized a traditional Eulerian approach for their energy analysis.

Furthermore, Brennan and Vincent (1980) reinterpreted the boundary terms $B\Phi_Z$ and $B\Phi_E$ as the work done by zonal and meridional wind components against atmospheric pressure at the computational domain boundaries. However, they noted that these terms, as calculated, were unrealistically large due to minor errors in the geopotential height field, which could escalate in major errors and significantly skew the results. Consequently, these terms were combined with the dissipation terms (D_Z and D_E) and treated as residuals in the balance equations for K_Z and K_E , resulting in new terms RK_Z and RK_E . This approach and the updated energy cycle are depicted in Figure 2.19.

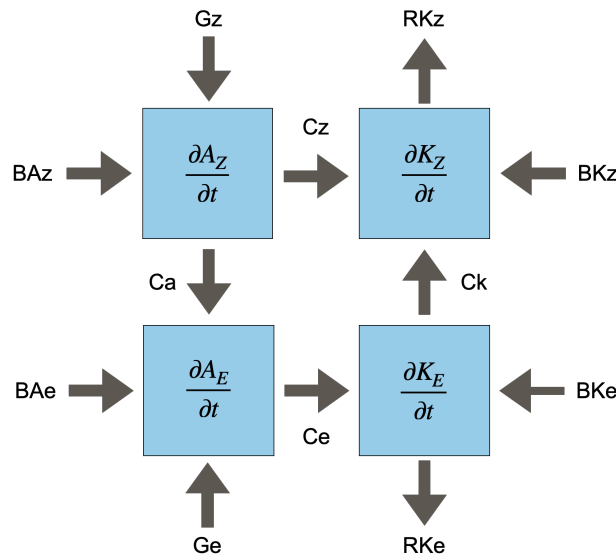


Figure 2.19: Updated energy cycle as reformulated by Brennan and Vincent (1980). This diagram includes the integrated terms for boundary energy flows ($B\Phi_Z$ and $B\Phi_E$) merged with dissipation processes (D_Z and D_E), represented as residual terms RK_Z and RK_E .

The modified energy balance equations are as follows:

$$\frac{\partial A_Z}{\partial t} = -C_A - C_Z + G_Z + BA_Z \quad (2.14)$$

$$\frac{\partial A_E}{\partial t} = C_A - C_E + G_E + BA_E \quad (2.15)$$

$$\frac{\partial K_Z}{\partial t} = C_K + C_Z + BK_Z + RK_Z \quad (2.16)$$

$$\frac{\partial K_E}{\partial t} = -C_K + C_E + BK_E + RK_E \quad (2.17)$$

And the residual terms are defined as:

$$RK_Z = B\Phi_Z + D_Z \quad (2.18)$$

$$RK_E = B\Phi_E + D_E \quad (2.19)$$

Robertson and Smith (1983) adapted the formulation presented by Brennan and Vincent (1980) for limited area domains, particularly revising the term A_E . Building upon the framework of APE for limited domains outlined by Smith et al. (1977), Robertson integrates the first law of thermodynamics into the Eulerian derivatives of the APE and A_Z formulations. This results in a significantly different balance equation for A_E , introducing a novel term associated with variations in the reference pressure field, which alters the computation of the conversion term C_A . This approach was driven by the goal of evaluating, through numerical modeling, the influence of moist processes on the energetics of extratropical cyclones. However, the adaptation necessitated computations over isentropic coordinates, introducing complexities in the numerical implementation.

In an effort to analyze the energetics of cyclogenesis in the Gulf of Genoa within the Mediterranean Sea, Michaelides (1987) advanced the energy cycle formulation further. Echoing concerns from Brennan and Vincent (1980) regarding unrealistic results for the terms $B\Phi_Z$ and $B\Phi_E$, Michaelides introduced additional residual terms RK_Z and RK_E , and a correction factor (ϵ) to account for numerical errors in the estimation of these terms, as shown in the equations and Figure 2.20. The modified set of equations is as follows:

$$\frac{\partial A_Z}{\partial t} = C_K - C_A + BA_Z + \Delta G_Z \quad (2.20)$$

$$\frac{\partial A_E}{\partial t} = C_A - C_E + BA_E + \Delta G_E \quad (2.21)$$

$$\frac{\partial K_Z}{\partial t} = C_K - C_Z + BK_Z - \Delta R_Z \quad (2.22)$$

$$\frac{\partial K_E}{\partial t} = C_E - C_K + BK_E - \Delta R_E \quad (2.23)$$

Where the residual terms are defined as:

$$\Delta R_Z = B\Phi_Z - D_Z + \epsilon_{KZ} \quad (2.24)$$

$$\Delta R_E = B\Phi_E - D_E + \epsilon_{KE} \quad (2.25)$$

$$\Delta G_Z = G_Z + \epsilon_{GZ} \quad (2.26)$$

$$\Delta G_E = G_E + \epsilon_{GE} \quad (2.27)$$

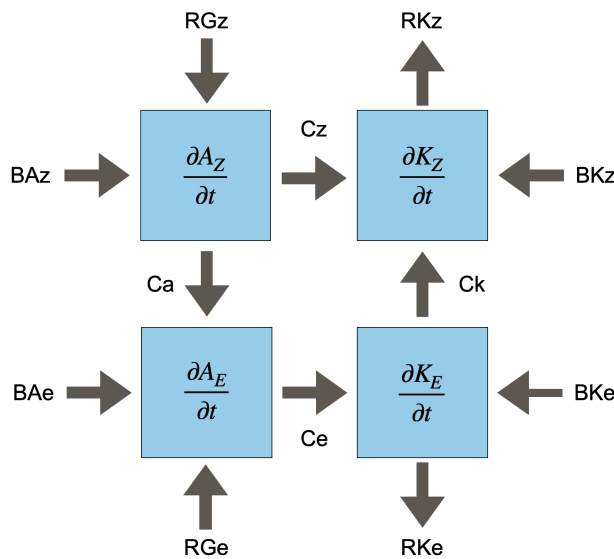


Figure 2.20: Refined depiction of the energy cycle incorporating modifications by Michaelides (1987). This representation includes error correction terms within the residual balances, addressing previous challenges with the quantification of boundary terms and dissipation factors.

In Michaelides et al. (1999), the author extends the energetic formulations presented in Michaelides (1987), exploring calculations for limited areas using both Eulerian and semi-Lagrangian reference frames. This study evaluates the energy cycle during a cyclogenesis event in the Mediterranean from these two perspectives, providing a nuanced discussion on the methodological implications of each. It highlights that the Eulerian approach is commonly preferred for energy analysis in limited atmospheric areas. This method necessitates defining a sufficiently large spatial domain to encapsulate all developmental stages of the system, including its movement and size changes. However, this approach has interpretative limitations; a broad spatial domain may inadvertently include adjacent synoptic circulations, thus diluting the specific energetics of the primary system under study.

Figure 2.21 illustrates this issue with a scenario akin to cyclogenesis in the coastal region of Southeast Brazil (Reboita et al., 2010; Gramcianinov et al., 2019, e.g.). Here,

the computational domain must encompass both the initial coastal genesis area and the subsequent oceanic trajectory of the cyclone. As the cyclone progresses to the ocean in its later stages, mesoscale circulations near the coast, such as updrafts due to surface heating and convection from sea breeze interactions with local topography, emerge. These processes can significantly alter the computed values of APE and K within the domain, affecting the energy conversion, boundary, dissipation, and generation terms, thereby complicating the interpretation of the cyclone's energy dynamics.

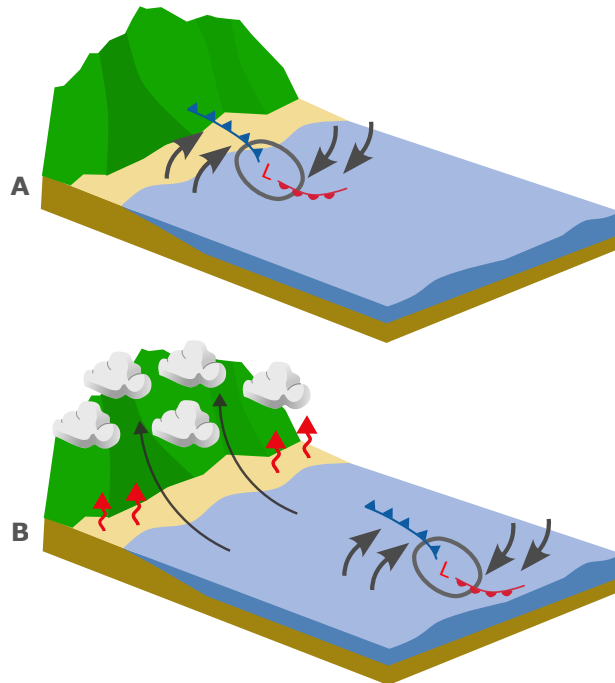


Figure 2.21: Illustration of challenges in using an Eulerian reference frame for energy cycle analysis. A) A cyclone forming near the continent, where the newly developed cyclonic system is the main meteorological feature inside the domain. B) The system is in its later oceanic phase, while meso-scale circulations develop in the coastal region, such sea-breeze and, consequently, orographic ascent over the mountain range near the coast.

Despite the inherent limitations associated with the Eulerian approach, Michaelides et al. (1999) discusses the methodological challenges of employing a purely Lagrangian framework to study extratropical cyclones. Such a study would require tracking the system in a three-dimensional space, isolated from external influences, using specific conservative variables for the encapsulated air masses. This is complicated by the diverse origins of the air masses involved in extratropical cyclones, which include both polar and tropical sources, affecting their conservative properties. Additionally, the system must be isolated from any spurious external circulations.

Consequently, Michaelides et al. (1999) advocates for a quasi-Lagrangian approach as a practical solution that minimizes the impact of neighboring circulations on the system's energy dynamics. This approach, similar to that proposed by Vincent and Chang (1973), utilizes multiple fixed domains at different temporal intervals to effectively track the cyclonic system. However, unlike Vincent and Chang (1973), Michaelides et al. (1999)'s formulation does not include terms for the displacement of computational domain boundaries. The author conducts a comparative analysis between the Eulerian and quasi-Lagrangian methods, revealing that they can yield significantly different results depending on the specific energetic terms analyzed. This highlights the complications in using the Eulerian method for comparative studies, as it can incorporate the energetic contributions of adjacent systems. Michaelides et al. (1999) concludes that the semi-Lagrangian method offers a more robust framework for analyzing the energetics of cyclonic systems.

Nevertheless, critiques of the quasi-Lagrangian approach exist (Dias Pinto and Rocha, 2011, e.g.). One major criticism is that this method does not allow for the local time derivatives of energy terms due to the absence of a fixed computational volume, which impedes a complete closure of the energy balance — a limitation acknowledged by Michaelides et al. (1999). Additionally, there is debate over whether changes in the energetics through the cyclone lifecycle can be attributed to the system's dynamics or to the fact that the tracking box may capture varying environmental conditions. However, these perceived limitations can be addressed by understanding that the distinct boxes used at each time-step through the cyclone's lifecycle are effectively "snapshots" of its dynamics. Consider the following thought experiment: we compute the LEC using both quasi-Lagrangian and Eulerian frameworks. The quasi-Lagrangian experiment tracks the trajectory of an extra-tropical cyclone, using a distinct $15^\circ \times 15^\circ$ domain for each hourly time step. Meanwhile, the Eulerian experiment employs a fixed $15^\circ \times 15^\circ$ domain in a specific location, which will coincide with the cyclone's trajectory at a given time step, thereby exactly matching the domain used in the quasi-Lagrangian framework. As demonstrated in Section 2.4.2, the equations used in LEC computation do not have temporal dependencies; therefore, for this specific time where the domains of both frameworks overlap, the results will be identical. At this time step, the quasi-Lagrangian domain likely contains only the cyclonic system, thus the computed energetics are indisputably linked to its development at that moment — or, using Smith (1969)'s interpretation: the system's contribution to global energetics.

Following this reasoning, it is logical to assume that each domain in the quasi-Lagrangian approach represents the cyclone energetics for each specific time step, effectively providing snapshots of the energetics.

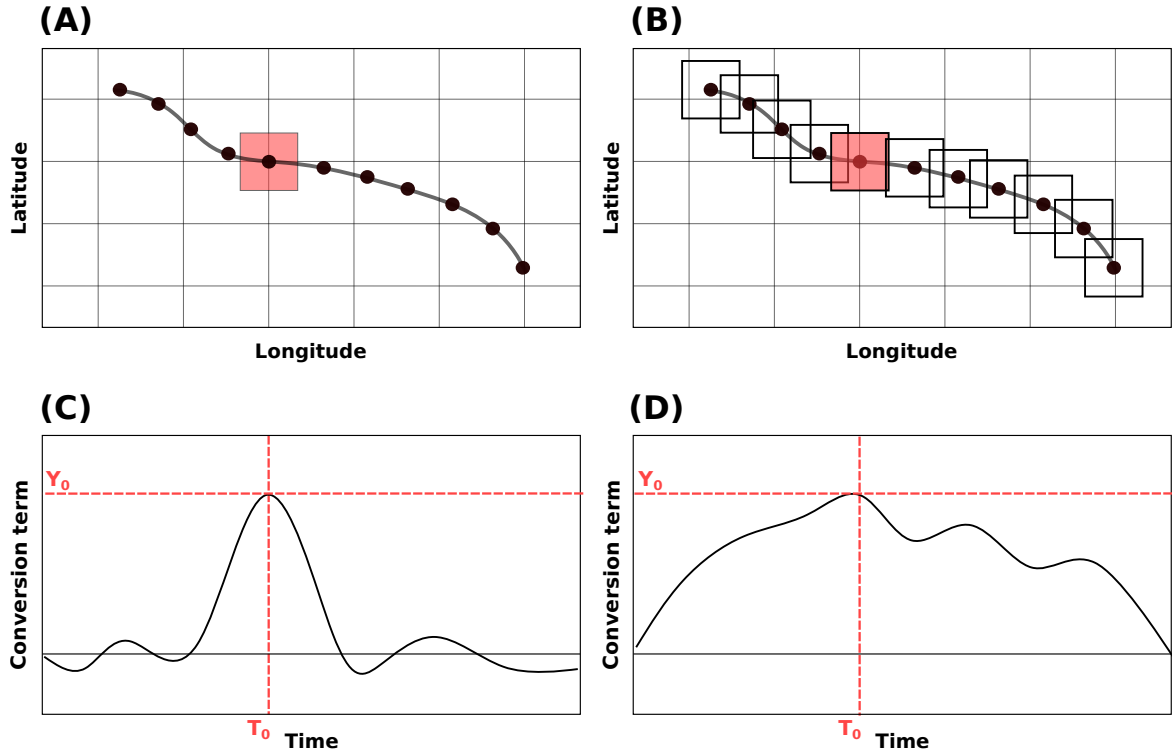


Figure 2.22: Illustration of the quasi-Lagrangian and Eulerian frameworks employed in the LEC computation for analyzing cyclonic energetics. Panel (A) shows the Eulerian approach with a fixed $15^\circ \times 15^\circ$ domain, overlapping with the cyclone's trajectory at a specific time step (T_0). Panel (B) depicts the quasi-Lagrangian approach, tracking a $15^\circ \times 15^\circ$ domain that moves with the cyclone, providing hourly snapshots. The highlighted domain in Panel (B) indicates the domain at T_0 that overlaps with the Eulerian domain from Panel (A). Panels (C) and (D) display a hypothetical conversion term used solely for demonstrating that both frameworks yield identical results (Y_0) when the domains coincide. This alignment supports the argument that each quasi-Lagrangian domain snapshot accurately reflects the system's energetics at each respective time step.

Several methodologies have been developed to refine diagnostic equations for atmospheric energetics, each offering unique advancements. The approach introduced by Plumb (1983) critiques traditional energy formulations for wave propagation and employs transformed Eulerian-mean equations to enhance the physical accuracy of eddy-mean flow interactions. Similarly, Marquet (1991)'s redefinition of exergy and available enthalpy provides a more complete analysis of atmospheric dynamics, accommodating factors such as static

instabilities and topographical variations often oversimplified in previous models. The local APE density framework proposed by Novak and Tailleux (2018), on the other hand, introduces a positive-definite local form of potential energy, akin to kinetic energy, which can be transported, converted, and dissipated locally. Unlike the global and volume-integrated nature of Lorenz's APE, this local APE density theory adapts potential energy calculations to specific atmospheric conditions, enhancing diagnostic precision in regional climate studies. However, these methods significantly complicate the mathematical formulations, requiring increased computational resources and extending computation times, which pose substantial limitations, especially for operational purposes. Additionally, each of these frameworks introduces new challenges in the physical interpretation of the terms.

The present work adopts the formulation presented by Michaelides et al. (1999), which offers a balance between computational feasibility and physical accuracy. This framework provides results that serve as a useful diagnostic tool, facilitating an understanding of the dynamical mechanisms involved in cyclone development without requiring extensive computational resources. While the primary goal of this thesis is scientific, there is significant interest in developing an operational tool for diagnosing the energy cycle of cyclones that can be made available to the scientific community. This tool is envisioned to function similarly to the Hart phase diagrams, which are accessible online (<https://moe.met.fsu.edu/cyclonephase/ecmwf/fcst/index.html>) and widely used for real-time cyclone analysis. The complete mathematical formulation and physical interpretation of each term in the Lorenz Energy Cycle (LEC) are detailed in Section 2.4.2. Additionally, Section 3.4 describes the computational methods used to calculate the LEC.

2.4.2 Lorenz Energy Cycle: Mathematical expressions and physical interpretation

This section provides a detailed description of the symbols and expressions used for the calculation of the Lorenz Energy Cycle (LEC), adopting the notation from Michaelides (1987).

Firstly, we define the zonal mean of a variable X , between longitudes λ_1 and λ_2 :

$$[X]_\lambda = \frac{1}{\lambda_2 - \lambda_1} \int_{\lambda_2}^{\lambda_1} X d\lambda \quad (2.28)$$

The eddy component of this variable is its deviation from the zonal mean:

$$(X)_\lambda = X - [X]_\lambda \quad (2.29)$$

The domain mean of the variable X , defined over the computational domain bounded by longitudes λ_1 and λ_2 , and latitudes ϕ_1 and ϕ_2 , is given by:

$$[X]_{\lambda\phi} = \left(\frac{1}{\lambda_2 - \lambda_1} \right) \left(\frac{1}{\sin \phi_2 - \sin \phi_1} \right) \int_{\lambda_2}^{\lambda_1} X \cos \phi d\lambda d\phi \quad (2.30)$$

Similarly, we define the deviation of the zonal mean from the domain mean:

$$([X]_\lambda)_\phi = [X]_\lambda - [X]_{\lambda\phi} \quad (2.31)$$

From the definitions above, the four energy components used in the LEC computation are defined as follows:

$$A_Z = \int_{p_t}^{p_b} \frac{[(T)_\lambda]_\phi^2}_{2[\sigma]_{\lambda\phi}} dp \quad (2.32)$$

$$A_E = \int_{p_t}^{p_b} \frac{[(T)_\lambda^2]_{\lambda\phi}}{2[\sigma]_{\lambda\phi}} dp \quad (2.33)$$

$$K_Z = \int_{p_t}^{p_b} \frac{[(u)_\lambda^2 + (v)_\lambda^2]_{\lambda\phi}}{2g} dp \quad (2.34)$$

$$K_E = \int_{p_t}^{p_b} \frac{[(u)_\lambda^2 + (v)_\lambda^2]_{\lambda\phi}}{2g} dp \quad (2.35)$$

where p is the atmospheric pressure, with subscripts b and t denoting the lower (base) and upper (top) pressure boundaries of the atmosphere, respectively. T represents temperature, g is the acceleration due to gravity, and u and v are the zonal and meridional wind components, respectively. The static stability parameter σ is defined as:

$$\sigma = \left[\frac{gT}{c_p} - \frac{pg}{R} \frac{\partial T}{\partial p} \right]_{\lambda\phi} \quad (2.36)$$

where c_p is the specific heat at constant pressure, and R is the ideal gas constant for dry air.

The APE terms A_Z and A_E are discussed in Section 2.4 and illustrated in Figure 2.16. The term A_Z quantifies the latitudinal temperature gradient, where higher values in the numerator indicate larger differences in mean temperature between latitudes — characteristically, the equator being warmer than the poles. Moreover, lower values of

the denominator suggest a more unstable atmosphere, which can more readily redistribute vertical motions and thus intensify the latitudinal temperature gradients. The term A_E is analogous to A_Z but referring to longitudinal temperature gradients caused by eddy motions, suggesting a higher presence of eddy available potential energy, which can be converted into kinetic energy, driving atmospheric motions.

The kinetic energy terms K_Z and K_E quantify the intensity of atmospheric motions. K_Z correlates with the zonal mean of the wind components; opposing winds cancel out, thus higher K_Z values occur when winds at the same latitude align directionally. The term $[u]\lambda$ denotes the large-scale east-west circulations, including the trade winds, westerlies, and jet streams, while $[v]\lambda$ relates to the north-south circulations, such as those in the Hadley and polar cells. Higher K_Z values therefore indicate stronger mean circulations, contributing to the overall momentum and energy in the atmospheric system. In contrast, $(u)\lambda$ and $(v)\lambda$ represent deviations from these mean values, capturing smaller-scale, turbulent motions and deviations from the average flow, including phenomena like cyclones, anticyclones, and other mesoscale and synoptic-scale disturbances. Thus, elevated K_E values signal increased eddy activity, enhancing turbulence and mixing within the atmosphere.

The four conversion terms are defined as follows, integrating over the atmospheric column from the base (p_b) to the top (p_t) pressures:

$$C_Z = \int_{p_t}^{p_b} -[(T)_\lambda]_\phi ([\omega]_\lambda)_\phi]_{\lambda\phi} \frac{R}{gp} dp \quad (2.37)$$

$$C_E = \int_{p_t}^{p_b} -[(T)_\lambda(\omega)_\lambda]_{\lambda\phi} \frac{R}{gp} dp \quad (2.38)$$

$$C_A = \int_{p_t}^{p_b} - \left(\frac{1}{2a\sigma} \left[(v)_\lambda(T)_\lambda \frac{\partial([T]_\lambda)_\phi}{\partial\phi} \right]_{\lambda\phi} + \frac{1}{\sigma} \left[(\omega)_\lambda(T)_\lambda \frac{\partial([T]_\lambda)_\phi}{\partial p} \right]_{\lambda\phi} \right) dp \quad (2.39)$$

$$C_K = \int_{p_t}^{p_b} \frac{1}{g} \left(\left[\frac{\cos\phi}{a} (u)_\lambda (v)_\lambda \frac{\partial}{\partial\phi} \left(\frac{[u]_\lambda}{\cos\phi} \right) \right]_{\lambda\phi} + \left[\frac{(v)_\lambda^2}{a} \frac{\partial[v]_\lambda}{\partial\phi} \right]_{\lambda\phi} \right. \\ \left. + \left[\frac{\tan\phi}{a} (u)_\lambda^2 [v]_\lambda \right]_{\lambda\phi} + \left[(\omega)_\lambda (u)_\lambda \frac{\partial[u]_\lambda}{\partial p} \right]_{\lambda\phi} + \left[(\omega)_\lambda (v)_\lambda \frac{\partial[v]_\lambda}{\partial p} \right]_{\lambda\phi} \right) dp \quad (2.40)$$

where a is the Earth's radius and ω is the vertical velocity in isobaric coordinates.

The term C_Z (Equation 2.38) shares some similarities with A_Z , as it represents the covariance product of temperature and vertical motion, averaged over the same latitudinal circle. Positive values of C_Z indicate a conversion from zonal available potential energy

(A_Z) to kinetic energy (K_Z), and vice versa. This conversion is detailed in the integrand, which contains the covariance product of the zonal deviation from the domain mean of $-T\omega$. Thus, positive values of C_Z correspond to either the vertical ascent of warm air or the descent of cold air. Conversely, negative values of C_Z are associated with the ascent of cold air or the descent of warm air. This phenomenon is depicted in Figure 2.23, which illustrates a region characterized by meridional gradients of temperature and vertical velocity. In warmer areas where the temperature deviation is positive and the ω deviation is negative, the product $T\omega$ is negative. With the additional negative sign in the equation for C_Z , this results in positive values of C_Z , signifying a conversion from A_Z to K_Z . On the other hand, in situations where air descends in warmer regions and ascends in colder regions, the covariance product $-T\omega$ would be positive, leading to negative C_Z values, indicating a conversion from kinetic energy (K_Z) to available potential energy (A_Z).

Figure 2.23 provides a visual interpretation of C_Z , showing a region with meridional gradients of temperature and vertical velocity. In this scenario, the combination of positive temperature deviations and negative ω deviations in warmer regions results in a negative product of $T\omega$, which when combined with the equation's negative sign, yields a positive C_Z , indicative of energy conversion from A_Z to K_Z . Conversely, in colder regions where temperature deviations are negative and ω deviations are positive, the product is also negative, leading to a positive C_Z . In the reverse situation, where air descends in warmer areas and rises in colder ones, the product $-T\omega$ turns positive, resulting in a negative C_Z , which signifies a reverse energy conversion from K_Z to A_Z .

The term C_E analogously represents the conversion between eddy forms of energy, from available potential energy (A_E) to kinetic energy (K_E). The interpretation of C_E mirrors that of C_Z , but it pertains to gradients and deviations along the longitudinal axis (x-axis) rather than the latitudinal (y-axis). Swapping the axes in Figure 2.23 would illustrate a scenario indicative of a positive C_E .

The term C_A (Equation 2.39) describes the energy conversion between zonal mean available potential energy (A_Z) and eddy available potential energy (A_E). Positive values of C_A signify energy transfer from A_Z to A_E , whereas negative values indicate the opposite. The equation for C_A can be divided into two components, each capturing how deviations from the zonal mean of the meridional (north-south) and vertical winds (addressed in the first and second components, respectively) interact with latitudinal temperature gradients.

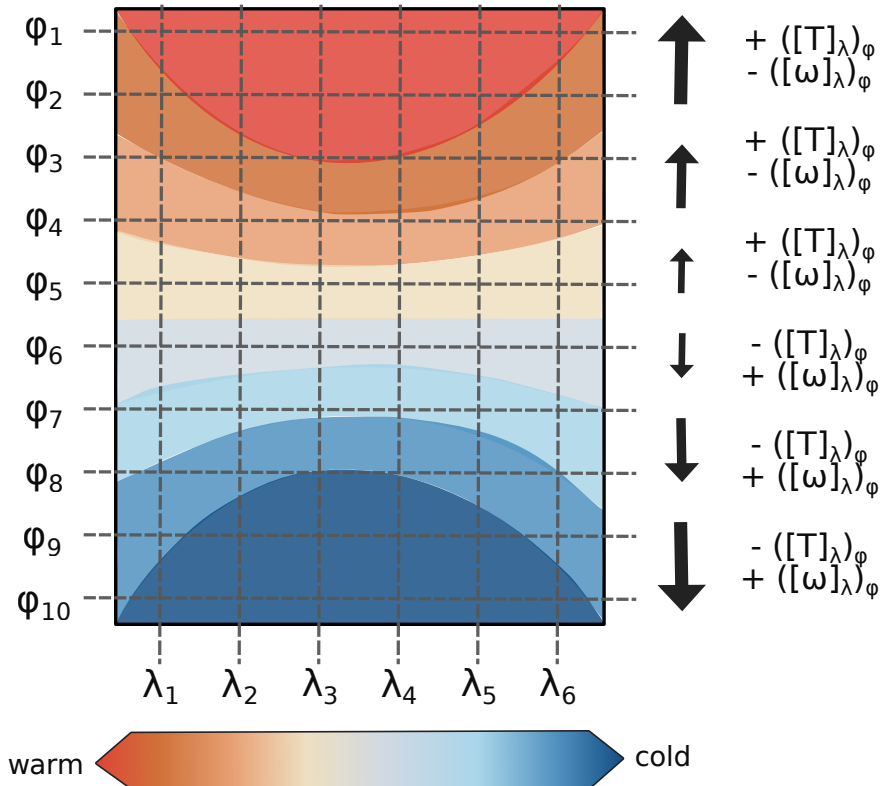


Figure 2.23: Hypothetical situation illustrating the conversion term between available potential energy (A_Z) and kinetic energy (K_Z), represented by C_Z . The y-axis represents latitude circles (ϕ), showing a decrease in temperature and vertical velocity ω (indicated by vertical arrows) toward the pole in the Southern Hemisphere. The x-axis represents longitude (λ).

In the first component, we have $(v)_\lambda(T)_\lambda \frac{\partial([T]_\lambda)_\varphi}{\partial\varphi}$. The negative sign within the equation implies that for C_A to be positive, this term must be negative. To understand each term's contribution to the sign of C_A , consider an illustrative case: a midlatitude low-pressure system in the Southern Hemisphere with a cold front propagating west to the system and a warm front east (Figure 2.24). In the cold front region, $(v)_\lambda$ is positive (northward), $(T)_\lambda$ is negative (cooler), and $\frac{\partial([T]_\lambda)_\varphi}{\partial\varphi}$ is positive (temperature increases equator-ward). Conversely, in the warm front region, $(v)_\lambda$ is negative (southward), $(T)_\lambda$ is positive (warmer), and $\frac{\partial([T]_\lambda)_\varphi}{\partial\varphi}$ remains positive. This configuration is consistent across both hemispheres when accounting for the appropriate directional changes in wind and temperature gradient.

The second component, $(\omega)_\lambda(T)_\lambda \frac{\partial([T]_\lambda)_\varphi}{\partial p}$, must also be negative to contribute positively to C_A . The term $\frac{\partial([T]_\lambda)_\varphi}{\partial p}$ reflects the zonal average atmospheric lapse rate, which typically presents as negative over the cold air mass between ϕ_3 and ϕ_6 and between λ_1 and λ_3 , indicating an increase in temperature with height. Above this level, the lapse rate reverses. In contrast, across the rest of the domain, particularly behind the warm front, this lapse

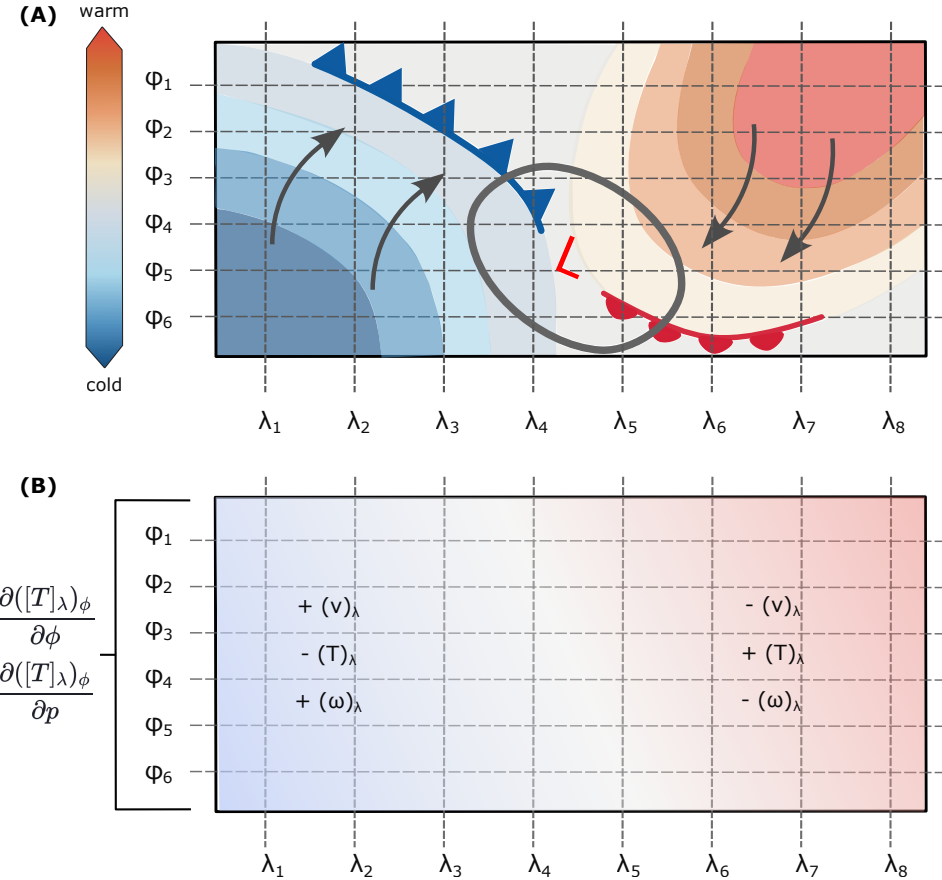


Figure 2.24: Representation of the conversion process between A_Z and A_E . (A) Illustration of an idealized situation of a midlatitude low-pressure system in the Southern Hemisphere, with a cold front propagating west and a warm front east. (B) Analysis of the variables involved in the formula for C_A (Equation 2.39). The y-axis represents latitude circles (ϕ), and the x-axis represents longitude (λ). In the Southern Hemisphere, latitude decreases from ϕ_1 to ϕ_6 .

rate term is positive. Consequently, when averaged across the domain and integrated over vertical levels, the overall contribution of this term tends to be positive. Furthermore, in the area behind the warm front, where $(\omega)_\lambda$ is negative (indicating ascending air) and $(T)_\lambda$ is positive (indicating warmer air), the product $(\omega)_\lambda(T)_\lambda$ is negative. This, in turn, results in a positive contribution to C_A , aligning with the term's requirement for a negative input to yield a positive output.

This analysis shows how an extratropical cyclone can influence global energetics. By transforming meridional into zonal temperature gradients, C_A converts zonal APE into eddy APE. The described scenarios are generalizations and do not capture all atmospheric variations during frontal passages; however, they do reflect significant energetic contributions, especially at lower atmospheric levels. Additionally, it is important to note that the

signs of the first and second components of C_A do not need to match; C_A will be positive if the magnitude of the negative component exceeds that of the positive component.

The last conversion term, C_K (Equation 2.40), represents the conversion of kinetic energy from eddies to the zonal mean state. Positive values indicate an energy transfer from K_E (eddy kinetic energy) to K_Z (zonal kinetic energy), and vice versa. This term's formulation is more complex than others, comprising five distinct components: 1) meridional advection of zonal momentum, 2) meridional shear of meridional wind, 3) interaction of eddy zonal wind with zonal meridional wind, 4) vertical advection of zonal momentum, and 5) vertical advection of meridional momentum.

For simplicity, in analyzing the first term—meridional advection of zonal momentum—we consider $(u)_\lambda$, $(v)_\lambda$, and $\frac{\partial[u]_\lambda}{\partial\phi}$, omitting variables related to the transformation from Cartesian to spherical coordinates. Consider a purely zonal westerly jet (Figure 2.25a), where as latitude decreases from ϕ_1 to ϕ_{10} , $\frac{\partial[u]_\lambda}{\partial\phi}$ transitions from negative in the northern part of the domain to positive in the southern part. However, both v and $(u)_\lambda$ are null in this scenario. Similarly, for a purely meridional northerly jet (Figure 2.25b), $(v)_\lambda$ varies from negative to positive across the domain, but $(u)_\lambda$ and $\frac{\partial[u]_\lambda}{\partial\phi}$ remain null. Therefore, averaged over the entire domain, this term is null for both scenarios.

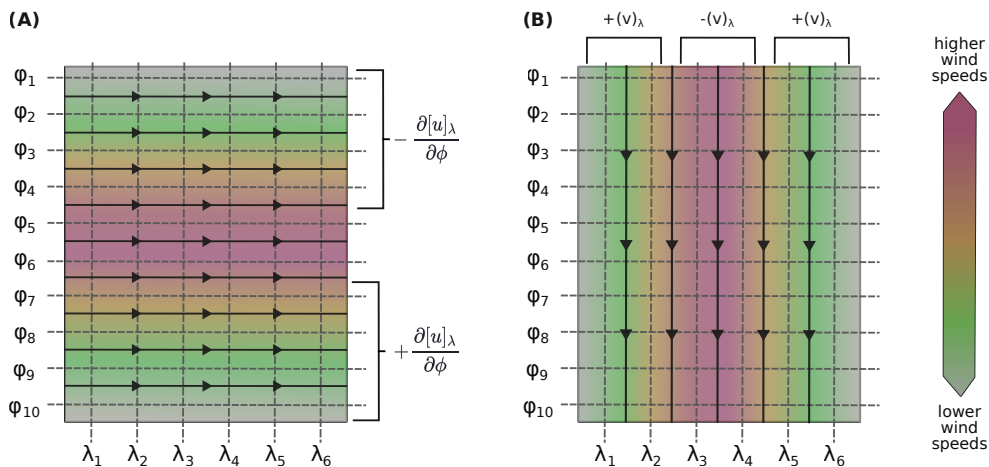


Figure 2.25: Illustration of (A) a zonal westerly jet and (B) a meridional northerly jet in the Southern Hemisphere. The y-axis represents the latitude circles (ϕ) and the x-axis represents longitude (λ).

In situations where small instabilities arise in the zonal or meridional flow, they may initiate the development of larger instabilities. For example, consider a zonal jet becoming unstable with a cyclonic (clockwise) deviation in its flow at the southern part of the domain (Figure 2.26a). Similarly as in a purely zonal jet, $\frac{\partial[u]_\lambda}{\partial\phi}$ exhibits negative values in

the northern part of the domain and positive values in the southern part (Figure 2.26b). With the onset of instability, $(v)_\lambda$ and $(u)_\lambda$ are no longer null across the domain: they are negative on the eastern flank and positive on the western flank of the perturbation. This leads to a positive contribution to C_K from the first term, indicating that the eddy is transferring energy to the zonal flow and thus depleting its own energy over time.

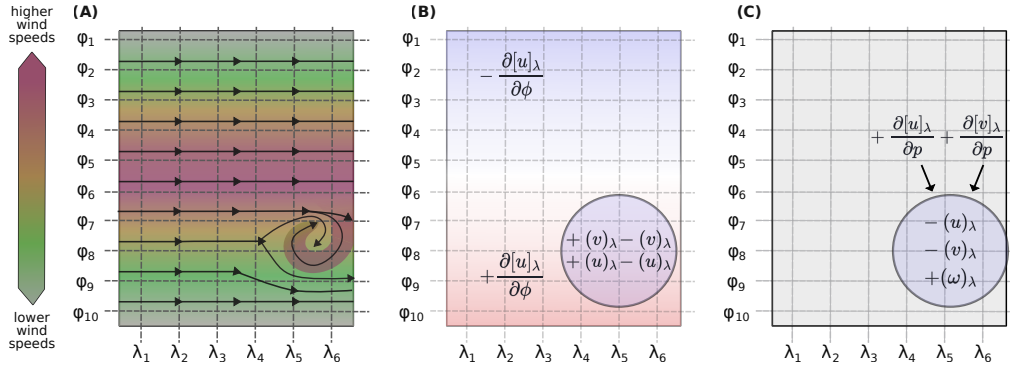


Figure 2.26: (A) Illustration of an eddy developing in the southern part of a purely meridional jet, (B) signal analysis for the first, (C) fourth and fifth terms of C_K (Equation 2.40), for this scenario. The y-axis represents the latitude circles (ϕ) and the x-axis represents longitude (λ).

The second term in C_K - meridional shear of meridional wind - contains $(v)_\lambda^2 \frac{\partial [v]_\lambda}{\partial \phi}$. It is evident that $(v)_\lambda^2$ is null for purely zonal jets, but otherwise is always positive, hence $\frac{\partial [v]_\lambda}{\partial \phi}$ dictates this term's contribution to the signal of C_K . While $\frac{\partial [v]_\lambda}{\partial \phi}$ is typically null for purely zonal and meridional jets, its contribution becomes significant for small instabilities in the zonal flow. For the eddy development illustrated in Figure 2.26a, as $|v|$ decreases from the western to the eastern flank of the perturbation, $[u] < 0$, so $\frac{\partial [v]_\lambda}{\partial \phi} > 0$, making this term's contribution to C_K positive.

The third term - interaction of eddy zonal wind with zonal meridional wind - contains $(u)_\lambda^2 [v]_\lambda$. Both $(u)_\lambda^2$ and $[v]_\lambda$ are null for purely zonal jets. However, similar to the previous terms, their combined signal can be investigated for perturbations in the zonal flow. As $(u)_\lambda^2$ is invariably positive, the signal of this term is influenced by $[v]_\lambda$. In the situation depicted in Figure 2.26a, $[v]_\lambda < 0$ leads to a negative contribution of this term to C_K .

For the fourth and fifth terms - vertical advection of zonal and meridional momentum, respectively - the analysis is more complex due to the three-dimensional variations in wind throughout the troposphere. The fourth term involves $(\omega)_\lambda (u)_\lambda \frac{\partial [u]_\lambda}{\partial p}$, while the fifth includes $(\omega)_\lambda (v)_\lambda \frac{\partial [v]_\lambda}{\partial p}$. In scenarios of purely zonal jets, both terms are null, but they

become significant with perturbations in the zonal flow.

Specifically, at mid-latitudes, we can assume that $\frac{\partial[u]_\lambda}{\partial p}$ is generally negative ($[u]$ increases with height) in the troposphere. However, in the scenario illustrated in Figure 2.26a, where the flow intensifies on the eastern flank of a perturbation, $[u]_\lambda$ becomes negative (westward), making $\frac{\partial[u]_\lambda}{\partial p} > 0$ (Figure 2.26c). Additionally, if the jet is at a higher altitude (e.g., 250 hPa), the convergence caused by the perturbation results in descending air, thus $(\omega)_\lambda$ is positive. These conditions render the contribution of this term to C_K negative. The analysis for the fifth term follows similarly, where $\frac{\partial[v]_\lambda}{\partial p} > 0$, $(u)_\lambda > 0$, and $(\omega)_\lambda > 0$ (Figure 2.26c), resulting in a negative contribution for this term to C_K .

Collectively, the first two terms contribute positively to C_K while the last three terms provide negative contributions. Thus, the terms that, when summed, present the highest magnitude, will dictate the overall signal for C_K . It is essential to recognize that the illustrative examples provided - zonal and meridional flows and a perturbation developing in the zonal flow - are simplifications of atmospheric motion. They are not intended to present a comprehensive picture of all conditions under which conversion between K_Z and K_E might occur but serve as guiding thought experiments to aid understanding of this conversion in real atmospheric motions. To the author's knowledge, due to the complexity of such analysis, no comprehensive attempt has been made previously in the literature.

The APE generation and K dissipation terms are defined as:

$$G_Z = \int_{p_t}^{p_b} \frac{([q]_\lambda)_\phi ([T]_\lambda)_\phi]_{\lambda\phi}}{c_p[\sigma]_{\lambda\phi}} dp \quad (2.41)$$

$$G_E = \int_{p_t}^{p_b} \frac{[(q)_\lambda (T)_\lambda]_{\lambda\phi}}{c_p[\sigma]_{\lambda\phi}} dp \quad (2.42)$$

$$D_Z = - \int_{p_t}^{p_b} \frac{1}{g} [[u]_\lambda [F_\lambda]_\lambda + [v]_\lambda [F_\phi]_\lambda]_{\lambda\phi} dp \quad (2.43)$$

$$D_E = - \int_{p_t}^{p_b} \frac{1}{g} [(u)_\lambda (F_\lambda)_\lambda + (v)_\lambda (F_\phi)_\lambda]_{\lambda\phi} dp \quad (2.44)$$

Here, F_λ and F_ϕ represent the zonal and meridional frictional components, respectively, and q is the diabatic heating term, computed as a residual from the thermodynamic equation:

$$\frac{q}{c_p} = \frac{\partial T}{\partial t} + \vec{V}_H \cdot \vec{\nabla}_p T - S_p \omega \quad (2.45)$$

where $\vec{V}_H \cdot \vec{\nabla}_p T$ represents the horizontal advection of temperature and S_p approximates the static stability, given by:

$$S_p \equiv -\frac{T}{\theta} \frac{\partial \theta}{\partial p} \quad (2.46)$$

where θ is the potential temperature.

The terms G_Z and G_E functionally resemble A_Z and A_E , respectively. The variable q quantifies the heat added to or removed from an air parcel through external sources such as radiation, latent heat release (e.g., condensation), and sensible heat exchange (e.g., conduction from the surface). The variable σ represents the overall stratification of the atmosphere. Generation of G_Z or G_E occurs when anomalous heating aligns with regions of anomalously high temperature, and anomalous cooling coincides with regions of anomalously low temperature. If the temperature/heating gradients are meridional (e.g., differential heating from the equator to the poles), G_Z is generated. Conversely, if the gradients are within the same latitude belt (e.g., differential heating between ocean and land), G_E is generated. Additionally, higher static stability, indicating a more stratified atmosphere, reduces the efficiency of APE generation, while lower static stability enhances it. Maximum generation of APE is analogous to the situation illustrated in Figure 2.24.

The terms D_Z and D_E represent the dissipation of kinetic energy from the zonal mean state and the eddies, respectively. The variable F denotes the frictional forces acting on the wind, which includes elements such as surface drag and turbulent friction. These frictional forces, notably surface drag and turbulent friction within the boundary layer, oppose the wind direction, causing a reduction in wind speed and consequently dissipating kinetic energy. Additionally, D_Z and D_E can also represent energy exchanges between different scales, specifically the transfer of energy from the grid scale to the subgrid scale. These forces not only convert kinetic energy into thermal energy but also facilitate the transfer of energy to smaller scale motions, thereby contributing to the overall energy dissipation within the atmospheric system.

The boundary terms are given by:

$$\begin{aligned} \text{BAZ} &= c_1 \int_{p_1}^{p_2} \int_{\varphi_1}^{\varphi_2} \frac{1}{2[\sigma]_{\lambda\varphi}} \left(2([T]_\lambda)_\varphi (T)_\lambda u + ([T]_{\lambda\varphi})_\varphi^2 u \right)_{\lambda_1}^{\lambda_2} \\ &\times d\varphi dp + c_2 \int_{p_1}^{p_2} \frac{1}{2[\sigma]_{\lambda\varphi}} \left(2[(v)_\lambda (T)_\lambda]_\lambda ([T]_\lambda)_\varphi \cos \varphi + ([T]_\lambda)_\varphi^2 [v]_\lambda \cos \varphi \right)_{\varphi_1}^{\varphi_2} dp \\ &- \frac{1}{2[\sigma]_{\lambda\varphi}} \left([2(\omega)_\lambda (T)_\lambda]_\lambda ([T]_\lambda)_\varphi + \left[[\omega]_\lambda ([T]_\lambda)_\varphi^2 \right]_{\lambda\varphi} \right)_{p_1}^{p_2} \end{aligned} \quad (2.47)$$

$$\begin{aligned} \text{BAE} &= c_1 \int_{p_1}^{p_2} \int_{\varphi_1}^{\varphi_2} \frac{1}{2[\sigma]_{\lambda\varphi}} [u(T)_\lambda^2]_{\lambda_1}^{\lambda_2} d\varphi dp \\ &+ c_2 \int_{p_1}^{p_2} \frac{1}{2[\sigma]_{\lambda\varphi}} \left([(T)_\lambda^2 v]_\lambda \cos \varphi \right)_{\varphi_1}^{\varphi_2} dp \\ &- \left(\frac{[\omega(T)_\lambda^2]_{\lambda\varphi}}{2[\sigma]_{\lambda\varphi}} \right)_{p_1}^{p_2} \end{aligned} \quad (2.48)$$

$$\begin{aligned} \text{BKZ} &= c_1 \int_{p_1}^{p_2} \int_{\varphi_1}^{\varphi_2} \frac{1}{2g} \left(u [u^2 + v^2 - (u)_\lambda^2 - (v)_\lambda^2] \right)_{\lambda_1}^{\lambda_2} \\ &\times d\varphi dp + c_2 \int_{p_1}^{p_2} \frac{1}{2g} \left([v \cos \varphi [u^2 + v^2 - (u)_\lambda^2 - (v)_\lambda^2]]_{\varphi_1}^{\varphi_2} \right) dp \\ &- \left(\frac{1}{2g} [\omega [u^2 + v^2 - (u)_\lambda^2 - (v)_\lambda^2]]_{\lambda\varphi} \right)_{p_1}^{p_2} \end{aligned} \quad (2.49)$$

$$\begin{aligned} \text{BKE} &= c_1 \int_{p_1}^{p_2} \int_{\varphi_1}^{\varphi_2} \frac{1}{2g} \left(u [(u)_\lambda^2 + (v)_\lambda^2] \right)_{\lambda_1}^{\lambda_2} d\varphi dp \\ &+ c_2 \int_{p_1}^{p_2} \frac{1}{2g} \left([v \cos \varphi [(u)_\lambda^2 + (v)_\lambda^2]]_\lambda \right)_{\varphi_1}^{\varphi_2} dp \\ &- \left(\frac{1}{2g} [\omega [(u)_\lambda^2 + (v)_\lambda^2]]_{\lambda\varphi} \right)_{p_1}^{p_2} \end{aligned} \quad (2.50)$$

where $c_1 = -[a(\lambda_2 - \lambda_1)(\sin \varphi_2 - \sin \varphi_1)]^{-1}$, $c_2 = -[a x (\sin \varphi_2 - \sin \varphi_1)]^{-1}$.

The boundary terms BA_Z , BA_E , BK_Z , and BK_E represent the fluxes of A_Z , A_E , K_Z , and K_E , respectively, from the lateral and vertical boundaries. Each boundary term has three components and shares a similar structure. For exemplification purposes, let's look into the BA_Z term. The first component represents the contribution of the zonal temperature flux anomalies to the A_Z term at the western and eastern boundaries. This term is computed for the westernmost and easternmost longitudes, integrated over all latitudes and pressure levels, and averaged over the entire domain. The second component is similar to the first one, representing the contribution of the meridional temperature flux anomalies to the A_Z term at the southern and northern boundaries. This term is computed for the southernmost and northernmost latitudes, integrated over all longitudes and pressure levels, and averaged over the entire domain. The third component represents

the contribution of the vertical temperature flux anomalies to the A_Z term at the top and bottom boundaries. This term is computed for the topmost and bottommost pressure levels, integrated over all longitudes and latitudes, and averaged over the entire domain. The same logic can be applied to all other terms, substituting A_Z with A_E , K_Z , and K_E , respectively.

The boundary terms BA_Z , BA_E , BK_Z , and BK_E represent the fluxes of A_Z , A_E , K_Z , and K_E , respectively, from the lateral and vertical boundaries. Each boundary term includes three components, all sharing a similar structure. To exemplify, consider the BA_Z term. The first component quantifies the contribution of zonal temperature flux anomalies to the A_Z term at the western and eastern boundaries. This term is calculated for the westernmost and easternmost longitudes, integrated over all latitudes and pressure levels, and averaged over the entire domain. The second component mirrors the first, representing the contribution of meridional temperature flux anomalies to the A_Z term at the southern and northern boundaries. This term is evaluated for the southernmost and northernmost latitudes, integrated across all pressure levels, and averaged domain-wide. The third component accounts for the contribution of vertical temperature flux anomalies to the A_Z term at the top and bottom boundaries. This term is calculated at the topmost and bottommost pressure levels and similarly averaged over the entire domain. Applying the same logic, the BA_E , BK_Z , and BK_E terms are structured analogously, with adjustments to the specific energetic terms they represent—substituting A_Z with A_E , K_Z , and K_E respectively.

Lastly, the terms $B\Phi Z$ and $B\Phi E$ are given by:

$$\begin{aligned} B\Phi Z = & c_1 \int_{p_1}^{p_2} \int_{\varphi_1}^{\varphi_2} \frac{1}{g} \left([v]_\lambda ([\Phi]_\lambda)_\varphi \right)_{\lambda_1}^{\lambda_2} d\varphi dp \\ & + c_2 \int_{p_1}^{p_2} \frac{1}{g} \left(\cos \varphi [v]_\lambda ([\Phi]_\lambda)_\varphi \right)_{\varphi_1}^{\varphi_2} dp \\ & - \frac{1}{g} \left(\left[([\omega]_\lambda)_\varphi ([\Phi]_\lambda)_\varphi \right]_{\lambda_\varphi} \right)_{p_1}^{p_2} \end{aligned} \quad (2.51)$$

$$\begin{aligned} B\Phi E = & c_1 \int_{p_1}^{p_2} \int_{\varphi_1}^{\varphi_2} \frac{1}{g} ((u)_\lambda (\Phi)_{\lambda_\lambda})_{\lambda_1}^{\lambda_2} d\varphi dp \\ & + c_2 \int_{p_1}^{p_2} \frac{1}{g} \left([(v)_\lambda (\Phi)_{\lambda_\lambda}]_\lambda \cos \varphi \right)_{\varphi_1}^{\varphi_2} dp \\ & - \frac{1}{g} \left([(\omega)_\lambda (\Phi)_\lambda]_{\lambda_\varphi} \right)_{p_1}^{p_2} \end{aligned} \quad (2.52)$$

The terms $B\Phi Z$ and $B\Phi E$ describe the dynamical mechanisms that produce or destroy kinetic energy. As elucidated by Muench (1965), these terms, along with C_Z and C_E , involve a arise from the derivation of the term $\vec{V} \cdot \nabla \Phi$. This expression represents the generation of kinetic energy through cross-isobaric flow towards areas of low pressure. Conversely, the destruction of kinetic energy occurs when there is cross-isobaric flow towards areas of high pressure.

Apart from examining the individual contributions of each term to the energy cycle, the Lorenz Energy Cycle (LEC) highlights specific interactions between terms that elucidate distinct dynamical mechanisms (Figure 2.27). The A_Z term, involving meridional gradients of temperature and atmospheric stability, interacts in such a way that $C_A > 0$ acts to diminish these gradients through the meridional transport of sensible heat. This process sets the stage for $C_E > 0$, driven by the zonal temperature gradient and vertical motions. In contrast, the conversion from K_Z to K_E (C_K) redistributes kinetic energy without altering the thermal structure and is primarily influenced by the horizontal shear of the mean flow. Therefore, the processes $A_Z \rightarrow A_E \rightarrow K_E$ are often referred to as the "baroclinic chain," while C_K is known as the barotropic conversion term (Michaelides, 1992; Veiga et al., 2013; Pezza et al., 2014; Okajima et al., 2021, e.g.). Additionally, the term "moist baroclinic chain" is used here to refer to the process where G_E supplies energy to A_E , acting in consonance with the baroclinic chain.

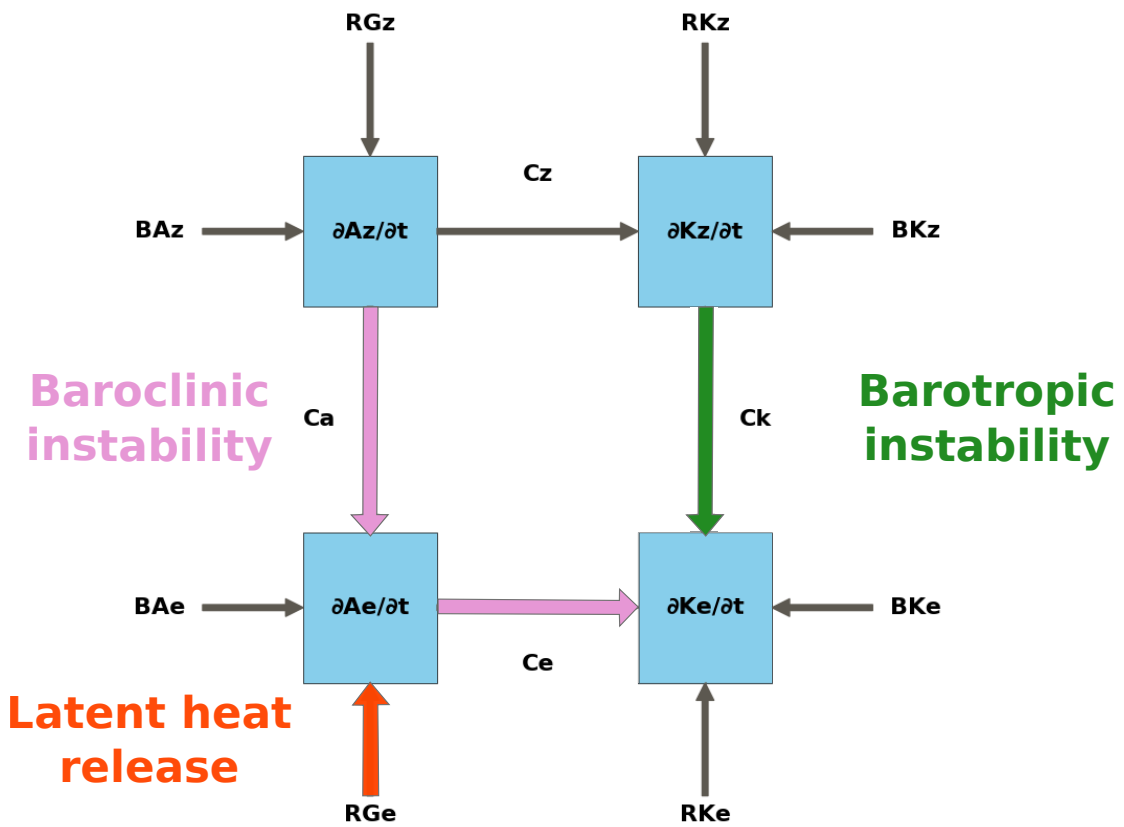


Figure 2.27: Schematic representation of the different energy conversion chains in the Lorenz Energy Cycle. The diagram illustrates the "baroclinic chain" ($A_Z \rightarrow A_E \rightarrow K_E$), indicating the role of baroclinic instability, the contribution of latent heat release by the G_E term and the "barotropic chain" ($K_Z \rightarrow K_E$).

2.4.3 Lorenz Energy Cycle applied to cyclonic systems

During the 1960s and 1970s, extensive research was conducted on the energetics of extratropical cyclonic systems. Smith (1980) reviewed these studies, offering a detailed summary of their outcomes. According to the mean kinetic energy (K) budgets, cyclones are areas of relatively higher concentrated kinetic energy compared to the rest of the hemisphere, though the difference is not markedly substantial. Cyclones are characterized by significant energetic activity, with substantial K_E generation through cross-contour flow. This generation is nearly balanced by the horizontal export of energy and its dissipation. Mature cyclones typically exhibit negative values for D_E ; however, in certain scenarios, D_E can act as an energy source ($D_E > 0$), especially in regions characterized by intense convection or the presence of short upper air waves, predominantly above the planetary boundary layer. This dynamic might be associated with energy transfer from sub-grid scales to the grid scale. Additionally, latent heat release from convective processes plays

a critical role in the generation of APE in extratropical cyclones. Generally, cyclones are inefficient thermodynamic systems; a significant portion of A_E is not converted into K_E , leading to an energy conversion efficiency of only 3% to 4%. Cyclones account for approximately 6% of the hemispheric energy contribution. However, intense cyclones, which are about 50% more energetically active than average, can contribute up to 20% of the hemispheric energy.

More recently, the study by Black and Pezza (2013) provides a detailed climatology of the energetics of cyclonic systems, specifically focusing on explosive cyclones. This research spans four major regions—the Northwest Pacific, the North Atlantic, the Southwest Pacific, and the South Atlantic—utilizing a 32-year climatology to analyze these phenomena. The analysis reveals that anomalous energy conversions begin approximately 48 hours before the explosive cyclone development and remain strong for up to 120 hours. The results demonstrate that the baroclinic chain is the primary mechanism driving the energy dynamics during explosive cyclogenesis, and this holds true across different regions and times of the year. Furthermore, the study finds that within the analyzed domains, the energetic signatures of regular cyclones often merge with background noise, making them indistinguishable.

The review by Smith (1980) provides a broad overview of the energy budget of extratropical cyclones, focusing primarily on their contributions to general circulation rather than on the dynamical mechanisms essential for their development, intensification, and decay. Meanwhile, Black and Pezza (2013) offers a more detailed picture, especially of explosive cyclones. However, the difficulty in distinguishing the energetic signatures of regular cyclones from background noise may be attributed to the large computational domains used, which are extensive enough to include multiple cyclonic systems simultaneously, potentially complicating the analysis. To overcome these challenges and gain a deeper understanding of cyclonic energetics, specific case studies are essential. These studies provide insights into how various energy transformations within a cyclone contribute to its lifecycle. The literature reviewed in the next paragraphs highlights the pathways that supply energy to the eddy energy reservoirs, with particular emphasis on the K_E term, which serves as a proxy for the system's intensity. Special attention is given to the contributions of the baroclinic ($A_Z \rightarrow A_E \rightarrow K_E$) and barotropic ($K_Z \rightarrow K_E$) chains, as well as to the contributions from latent heat release (G_E) due to the eddy's convective activity. These elements are crucial

for understanding the energetic dynamics that drive cyclone behavior and evolution.

There are only a few studies accessing the Lorenz Energy Cycle in the context of tropical cyclones. For instance, Brennan and Vincent (1980) analyzes the synoptic-scale energy budget of Hurricane Carmen (1979) as it intensified from a tropical depression to a major hurricane. During the tropical depression stage, K_E serves as a source of energy for both A_E and K_Z , while also exporting energy ($BK_E < 0$), primarily sustained by RK_E . Concurrently, A_E exports energy ($BA_E < 0$) and experiences energy destruction due to diabatic cooling and/or descending movements ($G_E < 0$). This suggests that during this phase, the system predominantly relies on up-scaling of energy from subgrid scales and/or cross-isobaric flow ($B\Phi E > 0$). However, during the hurricane stage, diabatic heating (from G_E) begins to supply energy to A_E , further supported by the import of energy ($BA_E > 0$) and conversion from A_Z . Most of this energy is transformed into K_E . Additionally, the zonal circulation contributes to the eddy energy ($C_K < 0$). Consequently, during the hurricane phase, moist baroclinic processes drive the system's development, supplemented by barotropic conversions. Despite an overall reduction in K_E and K_Z , the storm's circulation intensifies. The author attributes this paradox to mesoscale processes not being adequately resolved due to the poor resolution of the dataset, with negative values for both D_Z and D_E indicating an energy transfer from the resolved synoptic scale to the mesoscale. These observations imply that higher resolution datasets might reveal different dynamics for K_E and K_Z budgets.

Although the study by Brennan and Vincent (1980) provided important insights into the environmental energetics changes during hurricane formation, several caveats merit discussion. First, the dataset used features a coarse resolution with 2.5° grid spacing, which is insufficient to accurately represent mesoscale phenomena associated with the hurricane. Additionally, the data consisted primarily of point-source rawinsonde observations, surface observations, and daily infrared satellite imagery, with gaps filled by linear interpolation. Lastly, the computational domain was excessively large ($50^\circ \times 50^\circ$), raising concerns that the system's energetics could be confounded with background environmental influences. These limitations suggest that the study's findings should be interpreted with caution, considering the potential blending of cyclone energetics with broader atmospheric processes.

Using data from the NCEP/NCAR reanalysis, Veiga et al. (2008) analyzed the energy

budget for Hurricane Catarina, distinguishing its development into distinct phases. During the extra-tropical phase, the moist baroclinic chain was active, with both A_Z and G_E supplying energy to A_E , which was predominantly converted into K_E . As the system transitioned into the tropical phase, this chain loss intensity, notably as G_E decreased significantly, making the conversion from K_Z to K_E the primary contributor to K_E . However, much of this energy was exported from the domain, leading to a decrease in K_E . Upon reaching Category 1 Hurricane status, there was a reversal in the sign of the baroclinic chain, characterized by conversions from K_E to A_E to A_Z , with both C_K and RK_E playing roles in augmenting K_E .

More attention was given to the energetics of subtropical cyclones than to the tropical systems. Michaelides (1987) analyzes the synoptic-scale energy budget of a frontal depression that initially formed in the Mediterranean region, categorizing its evolution into four distinct phases. Although the nomenclature was not established at the time, the system might potentially have been classified as a medicane, a type of subtropical cyclone that originates in the Mediterranean (da Rocha et al., 2019). During the precyclogenetic period ("incipient stage"), A_E is sustained by contributions from A_Z , K_E , and BA_E . However, it experiences a net decrease due to negative generation from cooling and descending motions. Meanwhile, K_E sees an increase, fueled by conversions from K_Z and energy import. As cyclogenesis begins ("intensification stage"), the signals for both C_A and C_E reverse, enabling A_E to feed both A_Z and K_Z , supported by energy import and positive G_E . Although K_Z continues to enhance K_E , increased dissipation begins to diminish K_E . In the development phase ("mature phase"), A_E reaches its peak, primarily due to latent heat generation and significant energy import. A_E is actively converted to K_E , yet K_E continues to decline overall, affected by heightened dissipation and energy conversions to K_Z . In the post-cyclogenesis phase ("decay phase"), both A_E and K_E diminish as the system weakens, with marked reductions in import, conversion rates, and D_E reaching its maximum.

In their study, Dias Pinto et al. (2013) investigate the potential for tropical transition of Subtropical Cyclone Anita near the southeast Brazilian coast. During the early stages of the system, the barotropic chain primarily fueled K_E . As the system evolved into a hybrid stage and approached its potential for tropical transition, both moist baroclinic and barotropic chains actively supplied energy to K_E , complemented by positive values of G_E

due to convective processes. Concurrently, the system exported both A_E and K_E through its boundaries. Eventually, Anita entered a baroclinic environment and transitioned to an extratropical system. This phase was marked by a reversal in the sign of C_K and a dominance of the baroclinic chain in its energetics.

The study by Pezza et al. (2014) explores the energetics of the hybrid subtropical cyclone known as "Duck," which occurred over the Tasman Sea. Influenced by a persistent mid-latitude blocking high, the genesis of Duck created a conducive environment for cyclogenesis, with the system undergoing a partial tropical transition. During the genesis phase, a significant peak in C_K was observed, reaching a maximum near 350 hPa, facilitated by the presence of the blocking system — a similar environmental condition to that observed during Catarina's tropical transition. As Duck evolved, a secondary peak in baroclinic conversion coincided with the development of an upper-level warm core for the first time. However, the energy supply for K_E during this stage was insufficient for a full tropical transition. The authors speculate that the baroclinic conversion prevented Duck from achieving a complete tropical transition, hence not reaching hurricane status.

The energetics of the Duck storm were also investigated by Cavicchia et al. (2018), with comparisons made to an extratropical cyclone, the Pasha Bulker storm. Similar to findings by Pezza et al. (2014), the Duck storm's lifecycle was predominantly influenced by the barotropic chain, which was the main source of energy for K_E . In contrast, the Pasha Bulker storm was primarily driven by the baroclinic chain, with the most significant baroclinic energy conversions occurring during its intensification phase. However, Cavicchia et al. (2018) does not present results for generation and boundary terms, which limits the depth of the analysis.

For extratropical cyclones, a larger body of literature exploring their energy cycle can be found, especially for the Mediterranean and South Atlantic regions. For instance, in Michaelides (1992), an extratropical system originating in the Mediterranean region is analyzed, providing a basis for comparison with the earlier study by Michaelides (1987). During the initial development phase, A_E increases due to significant latent heat release and the advection of colder air over warmer waters, which enhances G_E and C_A . Concurrently, K_E is sustained by conversions from both A_E and K_Z . As cyclogenesis progresses, the energetic profile remains similar to the previous stage; however, convective activity and imports of A_E decline, leading to a decrease in this term. Simultaneously, an increase in

D_E causes a reduction in the absolute value of K_E . During this stage, K_E is primarily maintained by C_K . In the mature phase, there is a further decline in G_E and imports of A_E , causing A_E to decrease further. Additionally, as D_E increases and conversion from other terms decreases, K_E also diminishes over time. During the decay phase, G_E reaches its lowest level; however, A_E increases due to enhanced C_A and weakened C_E . Conversely, K_E , despite the weakened C_A and C_K , increases as dissipation becomes minimal.

Wahab et al. (2002) also analyzed the energy budget throughout the development of a Mediterranean cyclone. The cyclogenesis phase is characterized by a significant increase in K_E , primarily supported by the residual term (RK_E), while A_E is initially sustained by K_E . However, as the RG_E term increases, A_E begins to feed K_E . The growth period of the cyclone is marked by K_E being bolstered by C_K and imports of energy, which are subsequently either dissipated or converted to A_E , with RG_E acting as a sink of energy. During the dissipation period, A_E serves as a source of energy for both K_E and A_Z . Concurrently, while K_E is supported by K_Z and imports of energy, dissipation acts as a significant sink of energy, resulting in a decrease in K_E .

The study by Bulic (2006) investigates the energy budget associated with a deep and rapid cyclogenesis over the Mediterranean region, utilizing the ALADIN model. Before cyclogenesis, K_E is converted into A_E , a process that reverses after the cyclone forms. Throughout the cyclone's lifecycle, C_K consistently supplies energy to K_E . This conversion, most intense at upper levels around 350 hPa, is identified as crucial for the system's development. Additionally, B_{K_E} is responsible for exporting eddy energy throughout the entire lifecycle, except during the time of cyclone formation. The study highlights the cyclone's dependency on both baroclinic and barotropic processes; however, it also notes that the results may be limited to the dynamics captured by the model and might not fully reflect observational data.

Dias Pinto and Rocha (2011) analyzed the energy cycle for three extratropical cyclones, one for each genesis region in South America, detailing each system's development across formation, mature, and decay phases. For the first system, with genesis in the SE-BR region, the energetics were most active during the formation phase, where both baroclinic and barotropic chains provided energy to K_E , with significant contributions from the C_K term. In the mature phase, the baroclinic chain reversed, making C_K the sole contributor to K_E . During the decay phase, K_E transferred energy to K_Z and A_E to A_Z . The

second system, originating in the LA-PLATA region, maintained a consistent energy supply throughout its lifecycle via the moist baroclinic chain, most prominently during the mature phase. Throughout all phases, K_E consistently supplied energy to K_Z . The third system, with its genesis in the ARG region, was primarily sustained by the baroclinic chain, with contributions from latent heat release (G_E) only during the mature phase. Although less significant, there was also an energy supply from C_K during the formation and mature phases.

The study by Pezza et al. (2010) examines the Lorenz energetics of a high-latitude baroclinic storm that caused severe flooding in Nome, Alaska. The trajectory and intensity of the storm were significantly influenced by a blocking high-pressure system that steered its path a week prior to its formation. From the onset of cyclogenesis to the rapid intensification phase, the environment transitioned from lower to higher energy states, marked by peaks in A_E and K_E . During these phases, both the baroclinic and barotropic energy chains supplied energy to K_E , with a smaller contribution from G_E to A_E . The computational domain included the blocking region, highlighting the role of this high-pressure system in facilitating the energy conversion C_K , which supplied K_E to the cyclonic system. As the storm reached its peak activity, the barotropic chain reversed, with K_E feeding energy back to zonal kinetic energy (K_Z). Thus, during this stage, the maintenance of the system was predominantly sustained by the baroclinic chain. Additionally, the peak in baroclinic energy transfer occurred approximately 18 hours before the storm reached maximum intensity, indicating significant preconditioning of the environment by the baroclinic processes.

Michaelides et al. (1999) analyze the energetics of an intense Mediterranean cyclone, employing both Eulerian and quasi-Lagrangian frameworks for comparison. The quasi-Lagrangian framework reveals a significant increase in A_E during the cyclone's development, driven by diabatic heating processes such as latent heat release in the warm sector. Concurrently, K_E increases from the early stages to the maturity phase and then decreases as the cyclone decays. This initial rise in K_E is propelled by C_K , especially prominent at the jet level in the upper troposphere. The transformations between A_E and K_E are characterized by initial conversions of A_E to K_E , fueling the cyclone's intensification, followed by a reversal where K_E converts back to A_E as the system weakens. Notably, there are substantial imports of K_E during the cyclone's intensification phase and exports during its dissipation. The quasi-Lagrangian analysis indicates higher A_E and lower K_E compared

to the Eulerian method, suggesting that the fixed volume method captures more ambient kinetic energy from surrounding regions. Both methods confirm an overall conversion from K_Z to K_E , although the values are greater in the Eulerian method, and the conversions from A_E to K_E change signs. Additionally, there are reversals in signs for the boundary terms. The semi-Lagrangian method is considered to more genuinely represent the energetics characteristics of the synoptic system under study, as it isolates the cyclone as much as possible at all times. In contrast, the Eulerian method allows for circulations other than the cyclonic system under study to infringe into the computational region, potentially spuriously contaminating the cyclone's energetics.

The reviewed literature provides valuable insights into the energetics of different cyclonic systems. For tropical cyclones, although the limited body of literature prevents definitive conclusions, it appears that the barotropic chain, aided by the G_E term and subsequent conversions from A_E to K_E , is a primary driver for cyclone development. This emphasis on barotropic instability aligns well with research highlighting the role of barotropic instability in tropical waves for the initial development of tropical cyclones, with further intensification facilitated by latent heat release *via* CISK/WISHE mechanisms, as discussed in Section 2.1.3. Meanwhile, studies on subtropical cyclones indicate a shared contribution from barotropic and baroclinic processes, with the moist contributions to the baroclinic chain being variably active. The barotropic chain seems particularly important in the initial stages, with the baroclinic chain gaining significance in later stages. For extratropical cyclones, contrary to expectations, the baroclinic chain is not the sole driver of their energy cycle; most case studies indicate a role for the barotropic chain in their development. From Black and Pezza (2013)'s results, we can infer that the primary difference in the Lorenz Energy Cycle (LEC) between regular and explosive cyclones is the heightened importance of the baroclinic chain in the latter. Additionally, it is noteworthy that for both subtropical and extratropical systems, barotropic conversions occur predominantly at upper tropospheric levels. Nevertheless, while these energy pathways are crucial for system development, other terms also play important roles. For instance, D_E is often indicated as a significant sink for K_E , with larger values as K_E increases. Additionally, imports of K_E (BK_E), particularly in the early stages of development, also contribute to system development.

From the reviewed literature, it is evident that the LEC methodology is a valuable

diagnostic tool for studying cyclonic system dynamics. However, despite the methodology dating back to the 1960s and still being in use today, the body of literature on this topic is still expanding, primarily comprising case studies, with the only comprehensive climatology provided by Black and Pezza (2013). Furthermore, most case studies utilize the Eulerian framework, which may underestimate contributions from certain terms, as the large-scale environment might overshadow the systems' energetics. There is a need for more climatologies assessing the LEC for cyclonic systems—or at least analyses of a large number of systems—to better understand the energy pathways related to their development.

Chapter 3

Data & Methods

3.1 Fluxograma de atividades

- Fluxograma demonstrando os passos metodológicos e como se encaixam em cada pergunta de pesquisa

3.2 Databases

3.2.1 Cyclone tracks in the South Atlantic

For this study, precise information about the positioning (track) and central vorticity at the 850 hPa level (ζ_{850}) of cyclones was essential. These data were sourced from the "Atlantic Extratropical Cyclone Tracks Database" as detailed by Gramcianinov et al. (2020). Spanning from 1979 to 2020, this database covers the entire Atlantic Ocean within the spatial domain of 15°S–55°S and 75°W–20°E. Cyclone tracking within this database utilizes the ERA5 reanalysis fields, employing the TRACK algorithm (Hodges, 1994, 1995) and the method outlined by Hoskins and Hodges (2002), which computes relative vorticity from wind components at the 850 hPa level. The TRACK algorithm has previously been used for obtaining cyclone climatologies in the South Atlantic region (Gramcianinov et al., 2019, 2020). The ERA5 dataset was chosen for its superior resolution, offering significant advantages in analyzing regions with complex orography and temperature gradients, such as the SESA region, ensuring a comprehensive and consistent representation of cyclone climatology (Gramcianinov et al., 2020).

The tracking criteria included a minimum cyclone duration of 24 hours and a displacement threshold of 1000 km. These requirements align with previous climatologies of South

Atlantic cyclones (Sinclair, 1995; Gramcianinov et al., 2019). Additionally, systems that spent over 80% of their lifecycle over continental regions were excluded to avoid counting thermal lows and lee troughs, which are not the focus of this study (Crespo et al., 2021). While the primary focus was on extratropical cyclones, due to the specific calibration and sensitivity of the TRACK algorithm to features typical of these systems, the methodology does not explicitly exclude subtropical or tropical cyclones. Despite their rarity in the South Atlantic, subtropical systems, which occasionally exhibit characteristics similar to extratropical cyclones (Hart, 2003), may still be detected but remain a minority in the dataset. Further details on the methodology and database evaluation are discussed in Gramcianinov et al. (2020).

- ERA5
- Tracks do Atlântico Sul (base de dados da Carolina)
- CHIRPS (apenas se for incluir modelagem)
- QUICKSCAT (apenas se for incluir modelagem)
- OISST (apenas se for incluir modelagem)

3.3 *Cyclone’s Life Cycle Detection*

This section outlines the procedure for detecting the life cycle phases of cyclones. In the current study, an automated method, the Cyclophaser program, was developed and employed to facilitate this process. Section 3.3.1 provides an in-depth examination of the Cyclophaser program, highlighting its functionalities and the methodologies it employs. Subsequently, Section 3.3.2 explores the specific settings and configurations of the Cyclophaser used in this study.

3.3.1 *Cyclophaser program description*

To facilitate the detection of individual life cycle phases of cyclones, an automated Python package named Cyclophaser (Figure 3.1) was developed (**CITATION**). This package is open-source and freely available on the PyPI repository. It can be installed using

the pip package manager with the command `pip install cyclophaser`. Comprehensive documentation, including usage examples, is available on ReadTheDocs at <https://cyclophaser.readthedocs.io/en/latest/>, and the complete source code, which is open to contributions, can be found on GitHub at <https://github.com/daniloceano/CycloPhaser>.



Figure 3.1: The logo of the Cyclophaser program.

The program is designed to detect cyclone lifecycle phases using series of relative vorticity at the system's central position and its first derivative (Figure 3.2). While Cyclophaser was specifically developed and tested for this purpose, other variables such as sea level pressure or geopotential data might also be effective, although tests using these variables have not yet been conducted. Exploring how the lifecycle of cyclones might vary with different variables and how the geographical positioning of each stage might differ is an open research question.

The program begins with a preprocessing stage where users have the option to apply the Lanczos filter (Duchon, 1979) to the vorticity time series (Figure 3.2b). Based on the *sinc* function, the ideal mathematical representation of a low-pass filter, the Lanczos filter is adapted by windowing the *sinc* function to a finite range. Cyclophaser utilizes a band-pass filtering technique where weights are calculated using two cutoff frequencies, creating a differential of two *sinc* functions. This allows the filter to pass a specific frequency range while attenuating frequencies outside this range, permitting customization based on the spatio-temporal resolutions of different reanalysis datasets.

The Lanczos filter's primary use in Cyclophaser is to remove noise unrelated to the development of extratropical cyclones on synoptic scales, including fluctuations due to topography-induced circulations, sea breezes, and spatial and temporal variations in sea surface structures (Steele et al., 2015; Da et al., 2017; Acevedo et al., 2010). High-resolution datasets like ERA5 benefit from this filtering, which effectively reduces noise from struc-

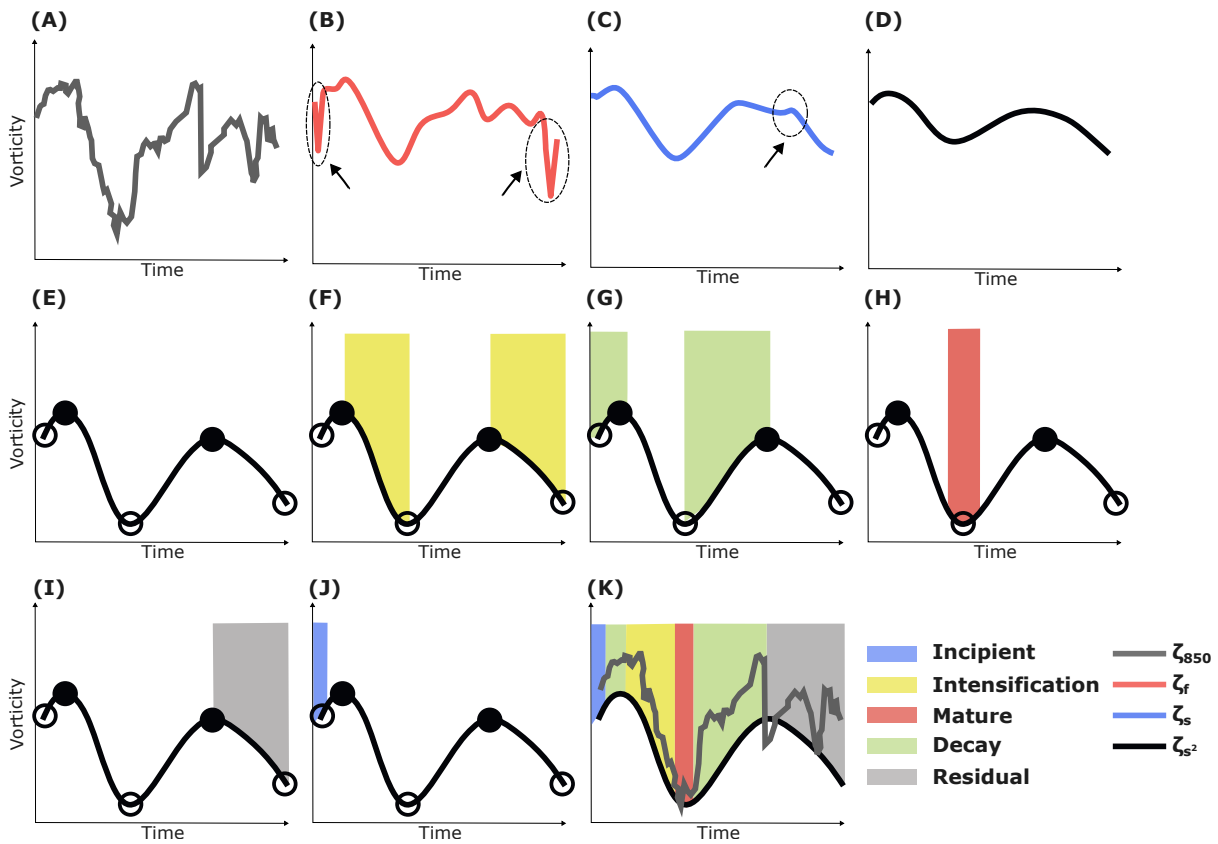


Figure 3.2: Illustrative representation of the methodological steps employed by Cyclophaser in analyzing cyclone lifecycle phases using vorticity series. The detailed steps demonstrate the application of data processing techniques including the Lanczos filter.

tures like frontal systems (Hoskins and Hodges, 2002). However, this filtering step may be omitted for datasets that have been preprocessed by tracking algorithms incorporating spatial filters (Murray and Simmonds, 1991; Pinto et al., 2005; Flaounas et al., 2014; Hoskins and Hodges, 2002, e.g.). The Lanczos filter can exhibit issues at discontinuities due to the Gibbs phenomenon and edge effects, leading to spurious oscillations at data series endpoints¹. To mitigate this, a weaker low-pass Lanczos filter is applied to the initial and

¹ The Lanczos filter, like other finite impulse response filters (FIR), can exhibit issues at discontinuities in the data. These issues arise primarily due to the Gibbs phenomenon and edge effects:

1. **Gibbs Phenomenon:** The Gibbs phenomenon refers to the overshoot and ringing that occurs near discontinuities when approximating a function with a finite series of basis functions (Gibbs, 1898; Hamming, 1989). In the context of the Lanczos filter, which utilizes a sinc function, abrupt changes at the edges of the filter window can cause ringing effects at the points of discontinuity in the data.

2. **Edge Effects:** FIR filters, including the Lanczos filter, can produce artifacts at the boundaries of the data series due to the reliance on data points that may not be available at the edges (Oppenheim and Schafer, 2009; Proakis and Manolakis, 2006). Techniques such as zero-padding or reflection are often used

final 5% of the data series, ensuring smoother transitions at the endpoints (Figure 3.2b).

The Lanczos band-pass filter is mathematically formulated as follows:

$$w(n) = \begin{cases} 2 \cdot (\text{cutoff}_{\text{high}} - \text{cutoff}_{\text{low}}) & \text{if } n = 0 \\ (\text{sinc}(2 \cdot \text{cutoff}_{\text{high}} \cdot n) - \text{sinc}(2 \cdot \text{cutoff}_{\text{low}} \cdot n)) \cdot \text{sinc}\left(\frac{n}{N}\right) & \text{if } n \neq 0 \end{cases} \quad (3.1)$$

where n is the index of the weight in the filter window, $w(n)$ is the weight at index n , $\text{cutoff}_{\text{low}}$ and $\text{cutoff}_{\text{high}}$ are the specified lower and upper cutoff frequencies, respectively, and N is half the length of the filter window. The *sinc* function is defined as:

$$\text{sinc}(x) = \frac{\sin(\pi x)}{\pi x} \quad (3.2)$$

After the initial filtering, the CycloPhaser program employs the Savitzky-Golay filter (Savitzky and Golay, 1964), as implemented in SciPy's package (Virtanen et al., 2020), to further reduce residual noise. This step is crucial for ensuring that the derivative curves form a sinusoidal pattern, which is essential for precise phase detection (Figure 3.2c). The Savitzky-Golay filter operates by fitting a polynomial of degree k to a window of $2m + 1$ data points centered at each point y_i in the input signal. The coefficients of this polynomial are determined by minimizing the least squares error between the polynomial and the data points within the window. The smoothed value \hat{y}_i at the point y_i is then calculated by evaluating the fitted polynomial at x_i :

$$\hat{y}_i = \sum_{j=-m}^m c_j y_{i+j}$$

where c_j are the coefficients derived from the polynomial fit, and m represents half the window size.

to mitigate these effects, but they can still result in artifacts or less accurate filtering near the boundaries.

3. Finite Window Length: The window length of the Lanczos filter determines the number of data points used in the convolution. A finite window length means the filter may not fully capture long-term trends or low-frequency components, especially at the edges, leading to discontinuities or spurious oscillations (Smith, 1997; Oppenheim, 1999).

4. Windowing Effect: The Lanczos filter uses a windowed *sinc* function to perform the convolution. While windowing reduces spectral leakage by smoothing the transition at the edges of the filter, it also introduces artifacts, particularly near discontinuities where the transition from one region to another is abrupt (Harris, 1978; Mitra, 2001).

Users have the option to apply this smoothing twice (Figure 3.2d), adjusting the window size $2m + 1$ and the polynomial order k to optimize the balance between noise reduction and data fidelity. This flexibility allows users to fine-tune the filter settings to meet specific requirements based on the spatio-temporal resolutions of various reanalysis datasets.

Subsequently, the first derivative of the relative vorticity is calculated predominantly using second-order finite differences, with central differences applied to interior points and first-order forward or backward differences used for endpoints. This derivative is then subjected to double smoothing with the Savitzky-Golay filter to maintain a sinusoidal pattern in the derivative series. This step is critical for accurately identifying cyclone lifecycle phases, making the dual smoothing process mandatory; omitting this could result in a noisy derivative series, potentially leading to erroneous phase detections, which emphasizes its necessity for reliable analysis.

The first phases to be detected are the intensification and decay stages. The program achieves this by analyzing peaks and valleys in the relative vorticity time series data, as shown in Figure 3.2e. The intensification phase is defined as the period between a peak and the subsequent valley (Figure 3.2f). Conversely, the decay phase is defined as the interval between a valley and the following peak (Figure 3.2g). To ensure that only significant phases are considered, each intensification and decay interval must span at least 7.5% of the total length of the time series. This threshold helps filter out minor fluctuations that are not indicative of true phase changes. To further refine the accuracy of phase detection, the program checks for multiple blocks of consecutive intensification or decay periods. If the gap between these blocks is smaller than 7.5% of the total series length, the program merges them into a single period. This merging process is crucial as it prevents the fragmentation of significant phases due to short gaps, thereby providing a more accurate and continuous representation of the intensification and decay stages.

After detecting the intensification and decay stages, the program proceeds to identify the mature stage of the cyclone's life cycle (Figure 3.2h). This stage is determined by analyzing not only the peaks and valleys in the relative vorticity but also the smoothed derivative of vorticity. Between a peak and the subsequent valley (or a valley and the subsequent peak) of the vorticity series, there is always a corresponding valley (or peak) in its derivative. These points indicate periods of maximum intensification or decay of vorticity. The mature stage is defined as the interval between a vorticity valley and an

adjusted point calculated based on the derivative of vorticity. Specifically, the mature stage spans from 12.5% of the time between the preceding derivative valley to 12.5% of the time to the following derivative peak. To be recognized as a significant mature stage, each interval must span at least 3% of the total length of the time series. This threshold ensures that only substantial periods are classified as mature stages. Additionally, the program verifies that all mature stages are preceded by an intensification stage and followed by a decay stage. This verification step ensures that the mature phase is accurately identified within the context of the entire cyclone life cycle.

Our methodology introduces the 'residual' stage, which is not directly related to the intrinsic development of extratropical cyclones but rather to peculiarities arising from the tracking algorithms (Figure 3.2i). This stage is exemplified in Figure 3.3. Panel (a) illustrates the intensification of a cyclonic system near the southernmost part of Argentina. The system reaches maturity, characterized by closed isobars at 850 hPa (Panel b). As the system begins to decay, it displays open isobars and diminished relative vorticity cohesion (Panel c). During its decay, it is influenced by a nearby system that leads to a temporary increase in the magnitude of its central relative vorticity, indicating a temporary re-intensification (Panel d). The tracking algorithm eventually discontinues its tracking, categorizing this late period of intensification as 'residual'—a phase of late intensification that is not associated with the primary development of the cyclone, as depicted in the relative vorticity series (Panel e).

The CycloPhaser classifies stages as residual by analyzing the previously detected cyclone phases. For phases classified as mature that do not transition to a decay stage, these instances are classified as residual. Similarly, if a full cycle of intensification, maturity, and decay is followed by another intensification that does not lead to a mature phase, it is also classified as residual (Figure 3.2i). This criterion accounts for scenarios where the tracking algorithm may continue to follow a cyclone post-decay, potentially capturing a re-intensification that does not culminate in a mature stage due to tracking limitations.

Following the residual phase classification, a post-processing step is applied to refine cyclone phase identification. This step bridges any gaps that may appear between consecutive periods identified as intensification or decay phases. Specifically, the program scans for discontinuities within consecutive phase blocks and fills any identified gaps with the adjacent phase to ensure smooth and continuous phase transitions. Additionally, this

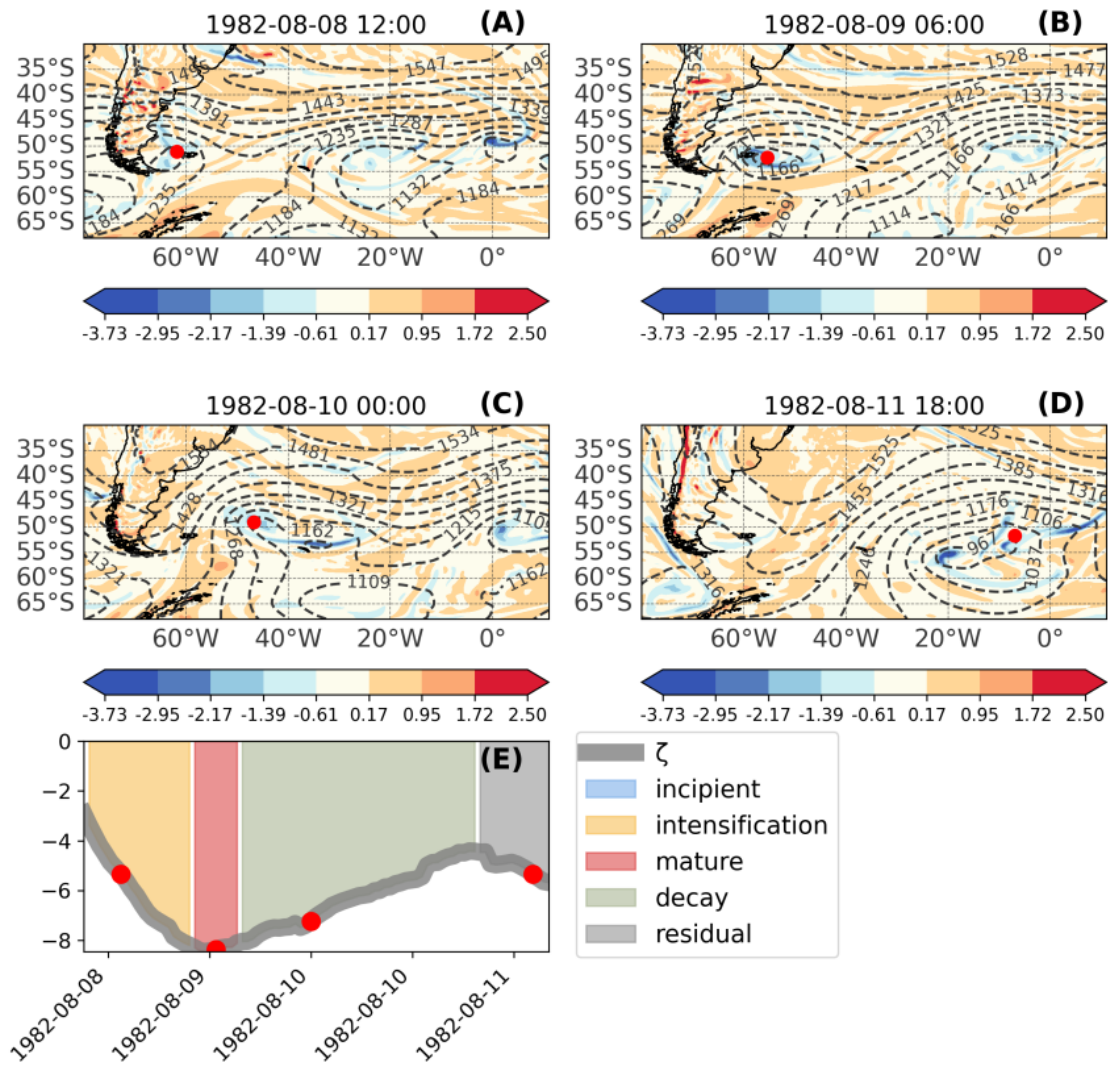


Figure 3.3: Relative vorticity (shaded) and geopotential heights (contours) at 850 hPa, illustrating distinct stages of a cyclone’s lifecycle where a residual stage is present. Panel (A) shows the intensification stage with isobars still open, indicating a strengthening system. Panel (B) depicts the mature stage, characterized by maximum organization and extent. Panel (C) illustrates the decay stage, with open isobars and reduced relative vorticity cohesion. Panel (D) captures the residual phase, where, despite a general trend of weakening, there is a temporary increase in vorticity influenced by external factors, not directly associated with the primary development of the cyclone. The complete lifecycle of the system is depicted in Panel (E), where each red dot on the vorticity series corresponds to the specific moments shown in Panels (A) to (D).

step involves correcting isolated phases—those misclassified phases that last only one time step—by aligning them with the subsequent phase if they occur at the start of the series, or with the preceding phase elsewhere. This adjustment enhances the consistency of phase identification throughout the cyclone lifecycle.

Ironically, the final step of the CycloPhaser program involves identifying the incipient

stage, which marks the beginning of cyclone development (Figure 3.2j). Initially, all undefined periods in the time series are labeled as incipient. Subsequently, the program analyzes the sequence of already labeled phases. If the life cycle commences with an intensification phase, the program searches for a vorticity valley preceding the next mature stage. Should such a valley be present, it designates the period from the start of the intensification phase to 40% of the duration to this valley as incipient. Conversely, if the life cycle starts with a decay phase, the program looks for a subsequent vorticity peak before the next mature stage. Upon identifying such a peak, it marks the time from the start of the decay phase to 40% of the duration to this peak as incipient.

The specific thresholds for phase detection, including the 7.5% duration for intensification and decay intervals, the 3% minimum for the mature stage, and the 12.5% intervals defining the boundaries of the mature stage, along with 40% of the series length for the incipient stage, were established through rigorous testing. This testing involved an iterative trial-and-error calibration process where various percentage thresholds were applied to a representative sample of cyclone tracks. The objective was to determine the most accurate parameters for delineating the phases. The chosen percentages proved effective in capturing the true progression of cyclogenesis while filtering out inconsequential fluctuations in vorticity. This meticulous calibration ensures that the CycloPhaser program reliably identifies each phase, providing a consistent and objective methodology for analyzing the life cycle of extratropical cyclones. This process is illustrated in Figures 3.4 and 3.5, 3.6, 3.7. For most of these thresholds, and in most cases analyzed, even altering the parameters to 25% or 150% of their original values did not result in significant modifications to the identified life cycle, reinforcing the method's reliability.

3.3.2 Cyclophaser settings

In this study, the default settings of the CycloPhaser were primarily utilized to identify the life cycle phases of cyclones. Since the TRACK algorithm already incorporates spatial filtering on the ζ_{850} vorticity fields, application of the Lanczos filter was deemed unnecessary (Hodges, 1994, 1995). Nevertheless, the Savitzky-Golay filter was applied twice to ensure that the ζ_{850} series exhibited a smooth sinusoidal profile. The window length of this filter was adjusted specifically for each system's life cycle duration: for systems with a total life cycle spanning 8 days, the window length was set to an odd integer approximately 25% of

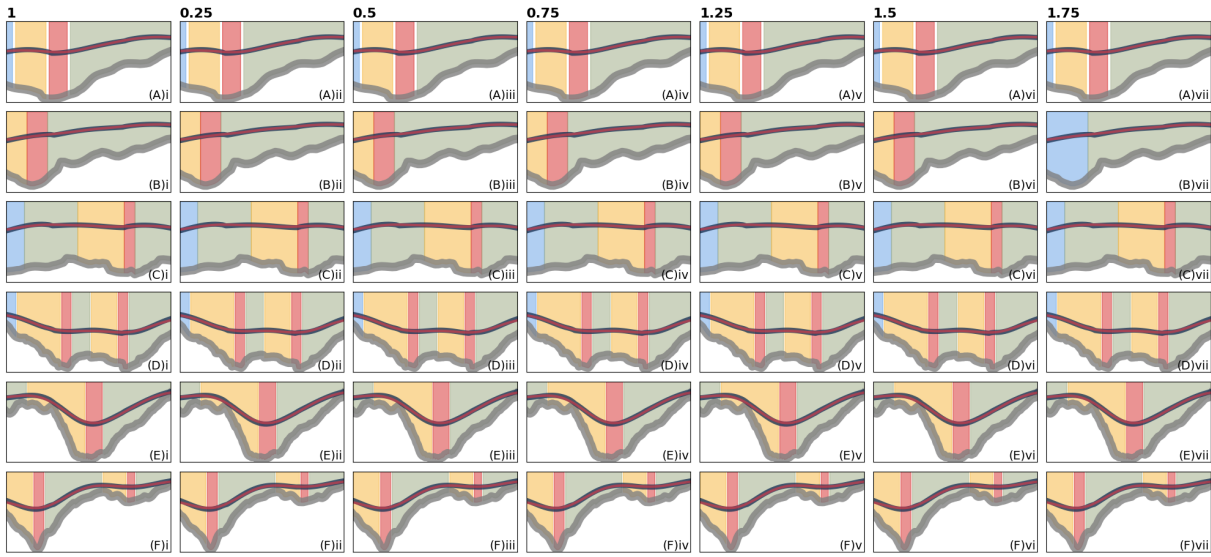


Figure 3.4: Impact of varying threshold values for the minimum length of the intensification phase across the six study cases. The original threshold value is maintained at 7.5% of the cyclone's total life cycle duration in panel (i). Panels (ii) to (vii) depict variations where the threshold is adjusted from 25% to 175% of the original value, illustrating the method's sensitivity to threshold changes. Adapted from **REFERENCE**.

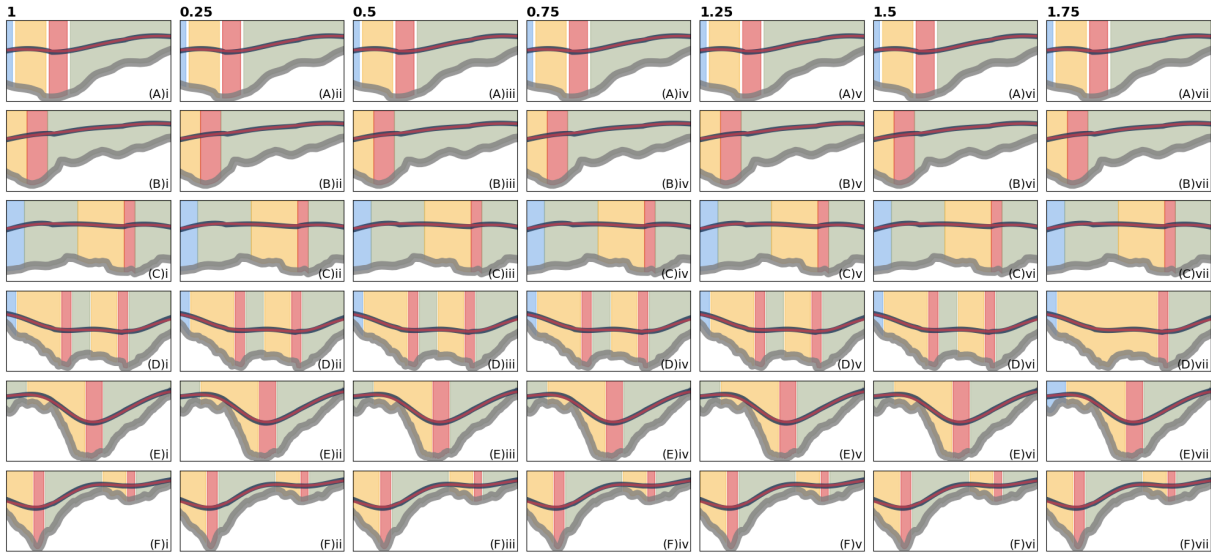


Figure 3.5: Same as Figure 3.4, but for the minimum length of the decay phase. Adapted from **REFERENCE**.

the series length. For systems with shorter life cycles, the window length was adjusted to an odd integer approximately 50% of the series length. In the second smoothing process, for life cycles exceeding 8 days, the window length was set to an odd integer close to 50% of the series length; however, for shorter cycles, it was kept consistent with the initial

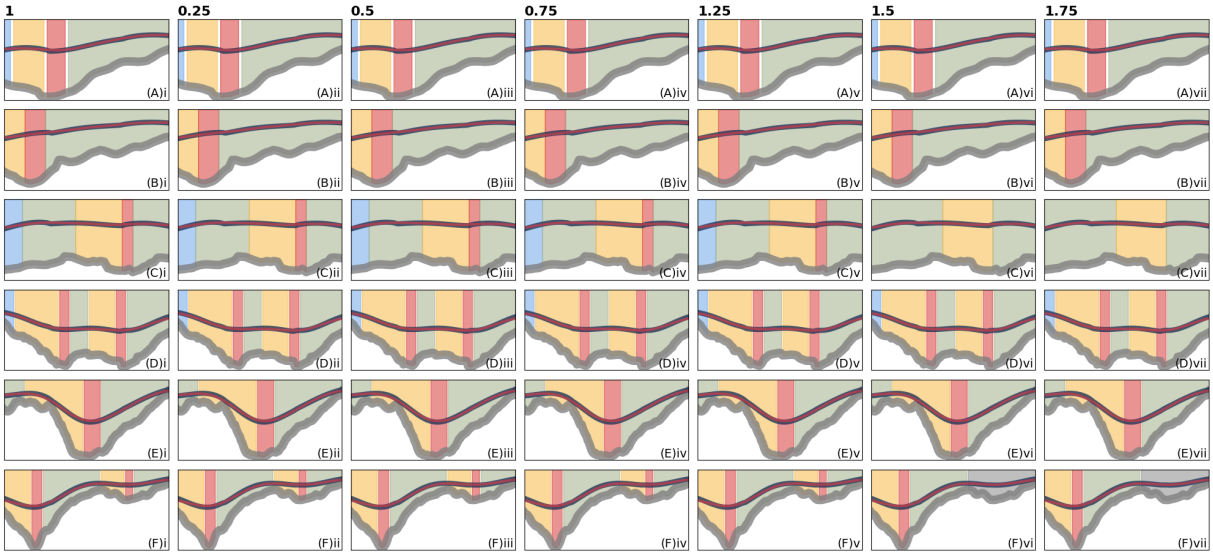


Figure 3.6: Variations in threshold values for the time intervals between the valley of vorticity and the preceding derivative valley, as well as from the vorticity valley to the subsequent derivative peak, used for determining the mature stage. The original threshold is set at 12.5%. Subsequent panels adjust this threshold from 25% to 175% of the baseline value, evaluating the robustness of phase detection across six study cases. Adapted from **REFERENCE**.

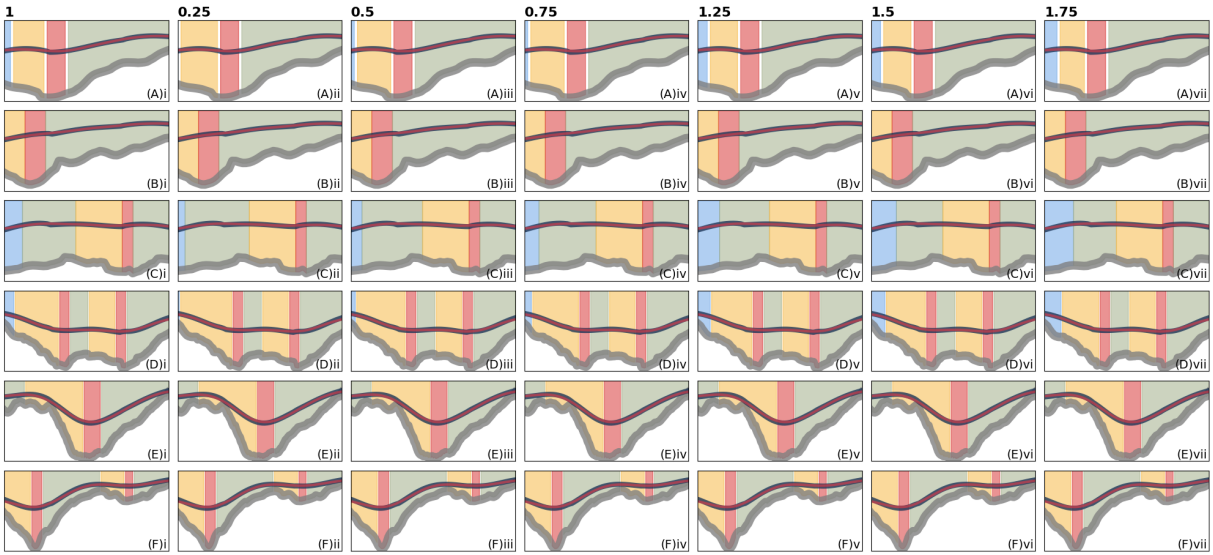


Figure 3.7: Impact of varying the minimum length threshold for the incipient phase of cyclone development. The incipient phase is identified from the beginning of the vorticity series to the next peak or valley in vorticity. The original threshold (shown in panel i) is set based on a percentage of the total vorticity series length. Panels ii to vii display the results when this threshold is modified from 25% to 175% of its original value across six study cases. Adapted from **REFERENCE**.

smoothing step.

3.4 Cálculo do ciclo energético

- Programa de calculo do LEC (Github) e procedimentos adotados para os cálculos

3.5 Determinação dos padrões energéticos

- Padronização da duração dos sistemas através do ciclo de vida
 - Cyclophaser
- Diagrama de fase (Lorenz Phase Space)
- Cálculo da PCA dos termos
- Método K-means

3.6 Descrição do MPAS-A

- Visão geral do modelo
- Descrição do núcleo dinâmico e discretizações numéricas
- Malha adotada e estrutura de grade (horizontal e vertical)
- Opções disponíveis de parametrizações físicas

3.7 Desenho experimental das simulações

3.7.1 Testes de sensibilidade: Furacão Catarina

- Desenho dos experimentos
 - Combinações de parametrizações físicas e de cumulus
 - Duração de cada set de experimentos (3 períodos de 48h cada)
- Inicialização do modelo
- Estrutura de grade adotada (horizontal e vertical)

3.7.2 Experimentos com SST

- Casos escolhidos
- Pertubações adotadas

Chapter 4

Life Cycle of Cyclones in the Southwestern Atlantic

This chapter delves into the varied life cycle configurations, statistical characteristics, and geographical distribution of cyclones within the Southwestern Atlantic, with a particular focus on the South American Southeastern region (SESA). Employing the Cyclophaser program, this analysis facilitates a detailed examination of cyclone behaviors and patterns. While some of the results discussed herein are also presented in **CITATION**, this chapter narrows its focus to the SESA region, unlike the cited study which includes all cyclogenesis regions across the South Atlantic, extending to the Antarctic Peninsula and the Weddell Sea. Section 4.1 examines statistical metrics for the selected cyclonic systems' whole life cycle, as well as for individual development phases, while Section 4.2 explores the spatial distribution of the distinct phases across the SESA and adjacent regions. These two approaches combined not only provide a novel perspective on the South Atlantic storm tracks and on the development of cyclonic systems but also open avenues for future research, as will be discussed.

4.1 *Climatology and Statistics*

This section delves into the climatology and statistical characteristics of cyclones in the Southwestern Atlantic, focusing on their frequency, seasonality, and developmental metrics such as average duration and intensity. Previous analyses have explored these aspects for systems originating in the SESA region; here, they serve both for comparative purposes and for validating the database generated during this study. A novel aspect of this analysis is the dissection of these metrics not just over the cyclones' complete lifecycles but also across distinct developmental phases. Section 4.1.1 presents the overall characteristics and

life cycle configurations of the detected cyclonic systems, Section 4.1.2 explores lifecycle statistics for different genesis regions and seasons, and Section 4.1.3 provides detailed statistical breakdowns by individual development phases.

4.1.1 Climatological Aspects and Life Cycle Configurations

Using the tracking methodology described in Section 3.2.1, the TRACK algorithm identified 33,376 cyclone systems in the South Atlantic region from 1979 to 2020. The focus here was on systems originating from the SESA region, specifically from SE-BR, LA-PLATA, and ARG genesis regions. After filtering to include only these tracks, the number of systems was narrowed down to 7,931 (Figure 4.1). Among these, 56% originated in the ARG region, 23.6% in LA-PLATA, and 20.4% in SE-BR. This distribution and general seasonality aligns with previous studies by Gramcianinov et al. (2019) and Crespo et al. (2021). However, the SE-BR region exhibited a higher relative frequency in this analysis, potentially attributable to the finer resolution of the ERA5 dataset used here compared to previous studies (Gramcianinov et al., 2020). However, comparing the seasonal distribution with earlier studies introduces complexities due to variations in the definitions and boundaries of genesis regions (Reboita et al., 2010; Crespo et al., 2021, e.g.,).

During the period from 1979 to 2020, cyclonic systems originating from the ARG, LA-PLATA, and SE-BR regions demonstrated 41 distinct life cycle configurations (Figure 4.2). Most configurations did not account for more than 1% of the total system count, typically lacking a mature stage. This phenomenon is likely due to these systems having maturation stages shorter than the CycloPhaser's threshold for detecting this phase. Adjusting the threshold to recognize shorter mature stages would risk identifying spurious cycles.

To focus on significant life cycle patterns, it was filtered the configurations to include only those comprising at least 1% of all types (Figure 4.3). This criterion reduced the sample size to 7,531 systems, accounting for approximately 95% of the original database. It was also merged life cycle counts that differed solely by the inclusion of a residual stage, as these are not indicative of the system's actual development (as discussed in Section 3.3.1). Further, to avoid bias in phase statistics, it was excluded life cycles lacking a mature phase. For instance, systems exhibiting only intensification and/or decay phases might have longer durations for these phases compared to others, potentially skewing statistics. Such configurations might represent undeveloped systems exiting the tracking

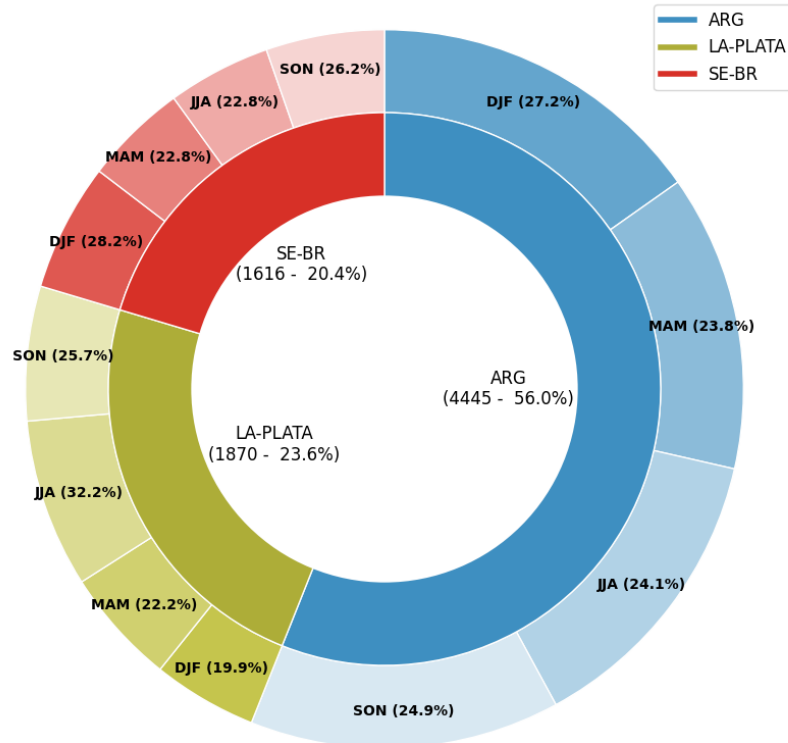


Figure 4.1: Number of systems and their relative frequencies by genesis region in the SESA region for the period 1979-2020. The inner pie chart displays the total frequency of systems by region, while the outer ring shows the seasonal distribution of cyclogenesis within each region.

domain before maturation. With these filters applied, the number of systems analyzed was reduced to 7,151, representing about 90% of the initial count of systems with genesis in the SESA region (Figure 4.3b).

Figure 4.4 depicts representative cases for each life cycle configuration retained for analysis (as shown in Figure 4.3b). The most common configuration in the SESA region typically follows the expected development pattern of extratropical cyclones: incipient, intensification, mature, and decay stages (Figure 4.4a), accounting for 68% of all evaluated systems. The second most common type mirrors this sequence but omits the incipient stage, indicating a rapid intensification process (Figure 4.4b). The third and fourth most frequent types depict a repeated complete cycle, including a secondary intensification, mature, and decay phases, with the third type including an incipient stage (Figure 4.4c) and the fourth lacking one (Figure 4.4d). The fifth and sixth configurations exhibit an early decay stage, differentiated by the presence (Figure 4.4e) or absence (Figure 4.4f) of an incipient phase.

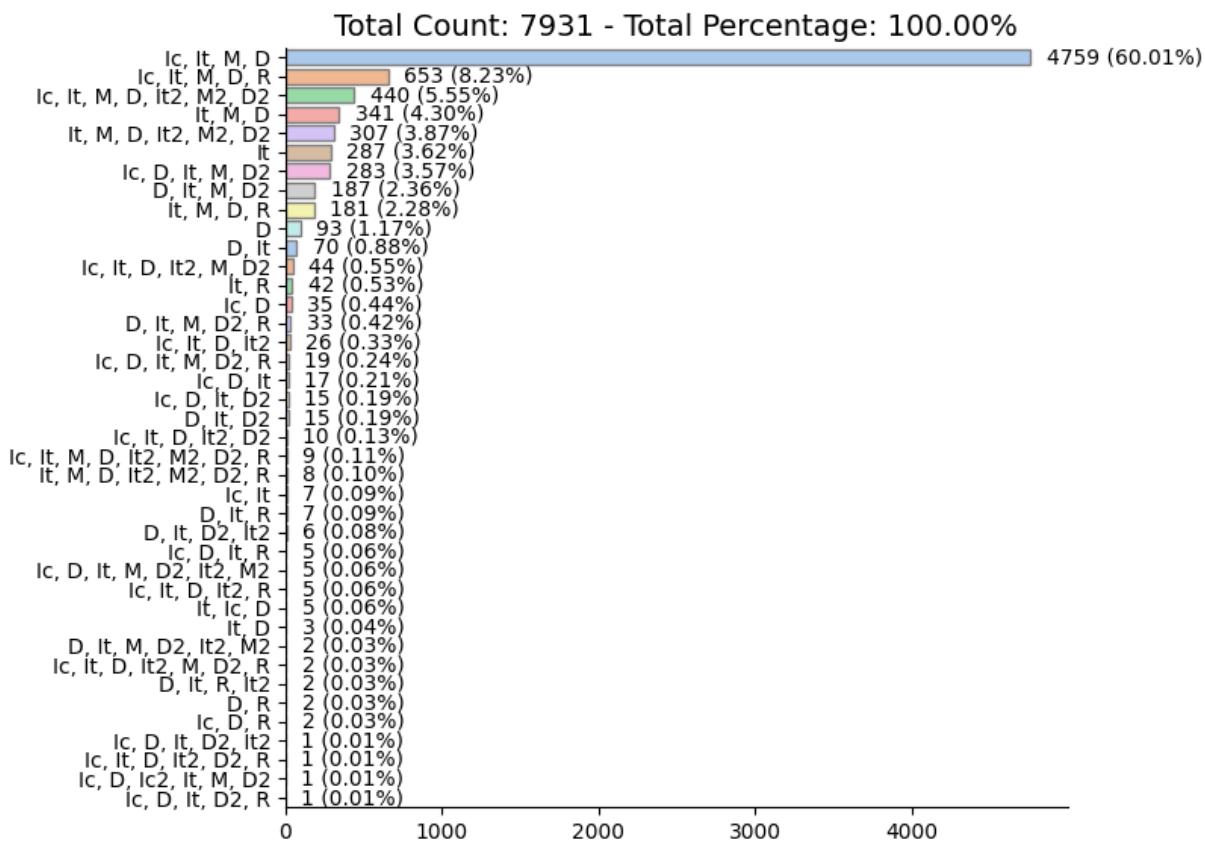


Figure 4.2: Distribution of all identified cyclone lifecycle configurations in the SESA region, spanning from 1979 to 2020. The configurations are sorted by their total count (frequency), with each bar representing the total number of cyclones exhibiting a specific lifecycle pattern, containing distinct stages: incipient (Ic), intensification (It), mature (M), decay (D), and residual (R), showing their sequence within the lifecycle.

The analysis reveals minimal to negligible seasonal variability in the frequency of each life cycle configuration across different genesis regions (Figure 4.5). The configurations "Ic, It, M, D" and "Ic, It, M, D, It2, M2, D2" are consistently more frequent, jointly accounting for 60% to 68% of all cases across all regions. However, exceptions include the "It, M, D" configuration emerging as the second most frequent in ARG during JJA, and in SE-BR during MAM and JJA. Additionally, the "Ic, D, M, D2" configuration appears significantly more often in LA-PLATA during JJA and in SE-BR during SON.

4.1.2 Mean Cyclone Statistics

This section explores the statistical analysis of cyclones in the SESA region, comparing the constrained data utilized in this study with extant literature. Results are presented both for an aggregate view across all genesis regions and individually by region. To capture

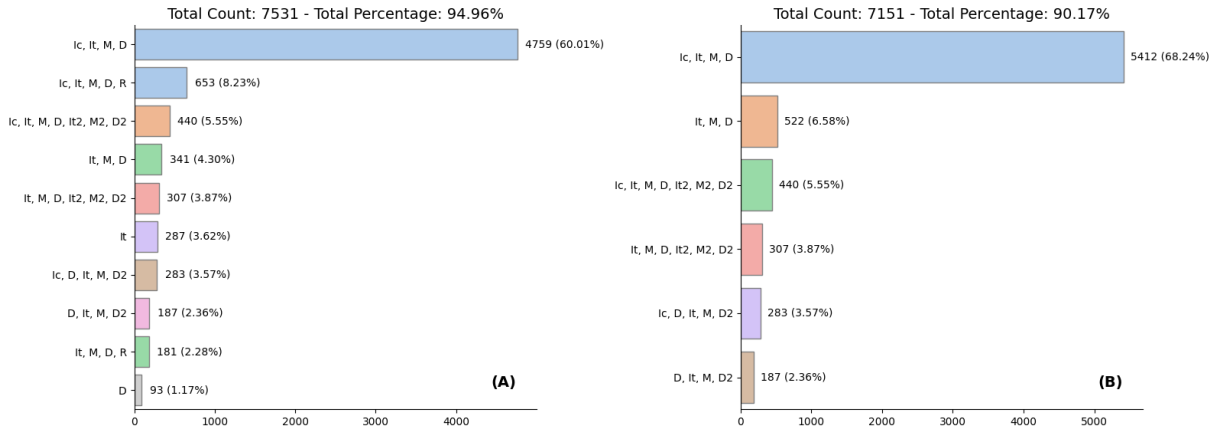


Figure 4.3: (a) Lifecycle configurations of cyclones that represent at least 1% of the total identified patterns. (b) Adjusted lifecycle configurations after merging periods classified as residual and removing stages not contributing to a standard development pattern, focusing analysis on the core developmental stages of cyclones.

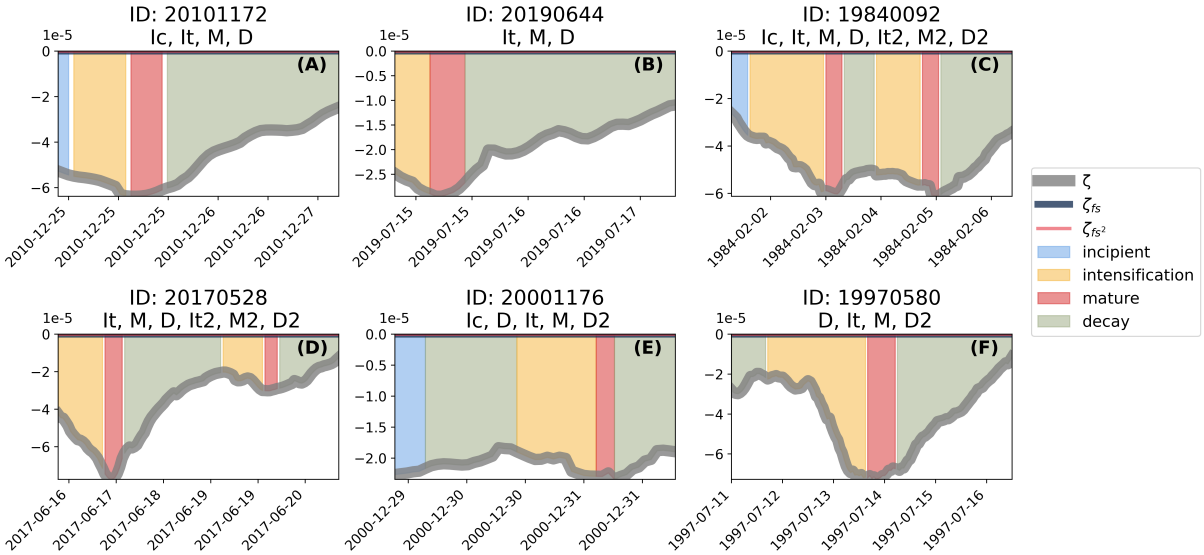


Figure 4.4: Representative examples of cyclone life cycles for configurations shown in Figure 4.3b. Panels A to F illustrate the central relative vorticity ζ_{850} and its first (ζ_{fs}) and second (ζ_{fs^2}) smoothed derivatives. Background colors indicate different life cycle phases: : incipient (Ic), intensification (It), mature (M) and decay (D). Lines represent the original vorticity series (ζ), the first (ζ_{fs}), and the second (ζ_{fs^2}) smoothed relative vorticity series.

the seasonal variability of cyclone behavior, analysis is focused on the winter (JJA) and summer (DJF) months. This approach is chosen because the transitional seasons (MAM and SON) generally display characteristics that are intermediate to those observed in JJA and DJF, aligning with findings from previous climatologies of the SESA region (Gan and Rao, 1991; Reboita et al., 2010; Crespo et al., 2021, e.g.).

On average, cyclones exhibit longer lifespans during DJF, with a duration of 97.6 ± 66.2

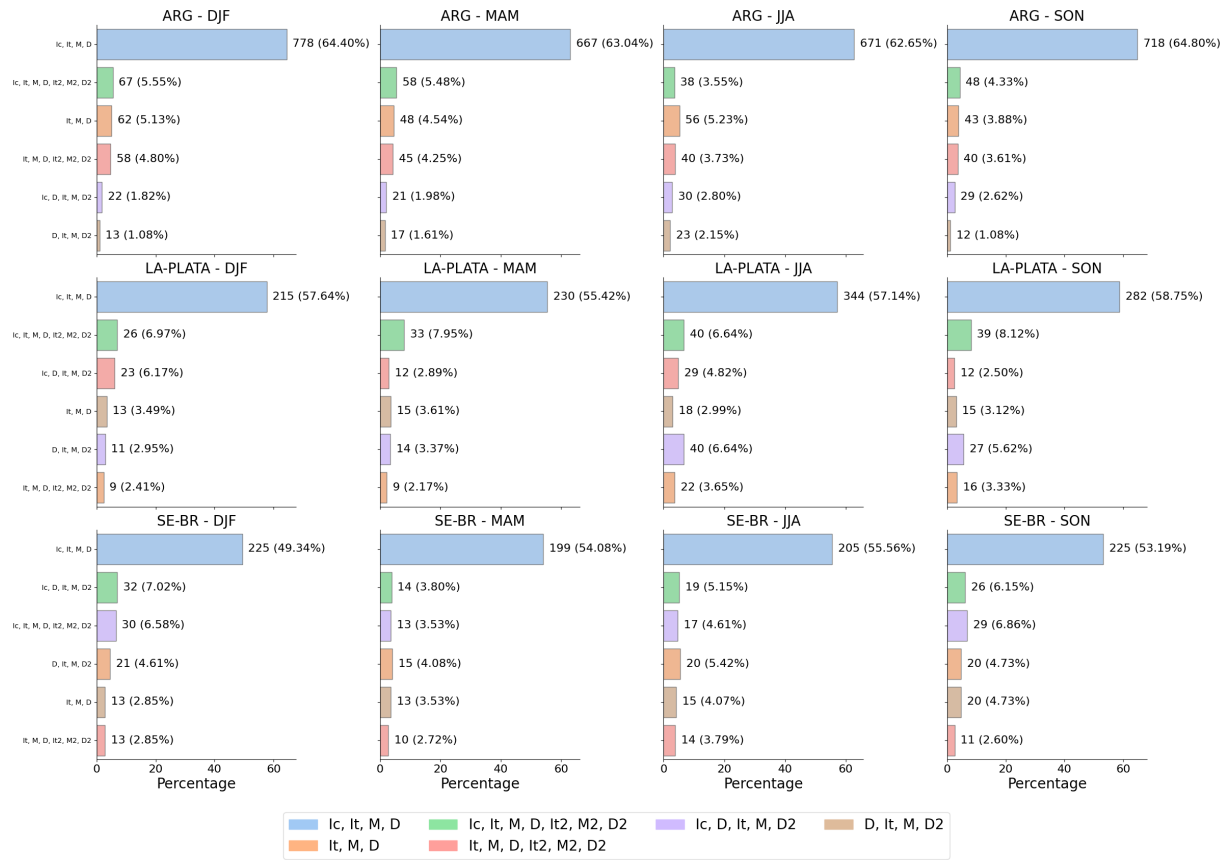


Figure 4.5: Similar to Figure 4.3, but separated by genesis region (ARG, LA-PLATA and SE-BR) and season.

hours (Figure 4.6a) compared to 91.1 ± 59.7 hours during JJA (Figure 4.6b). Conversely, the average total distance traveled by cyclones is slightly greater during JJA, amounting to 4777 ± 3182 km (Figure 4.6d), versus 4658 ± 3212 km in DJF (Figure 4.6c). This is reflected in the mean propagation speed, which is higher in JJA at 15.3 ± 4.8 m/s (Figure 4.6f) compared to DJF at 14.0 ± 4.4 m/s (Figure 4.6e).

These results largely corroborate those by Gramcianinov et al. (2019, 2020); Hoskins and Hodges (2005) and exceed the mean duration, traveled distance, and propagation speed reported by Simmonds and Keay (2000), Mendes et al. (2010), and Reboita et al. (2010). The disparities likely stem from differing tracking methodologies, data sets, and the exclusion of systems without a mature phase in our analysis. Particularly, the exclusion of continental systems may inflate displacement statistics during austral summer when quasi-stationary lows are prevalent over the continent (Mendes et al., 2010). Furthermore, Reboita et al. (2010) focused on oceanic systems, which might have overlooked early deve-

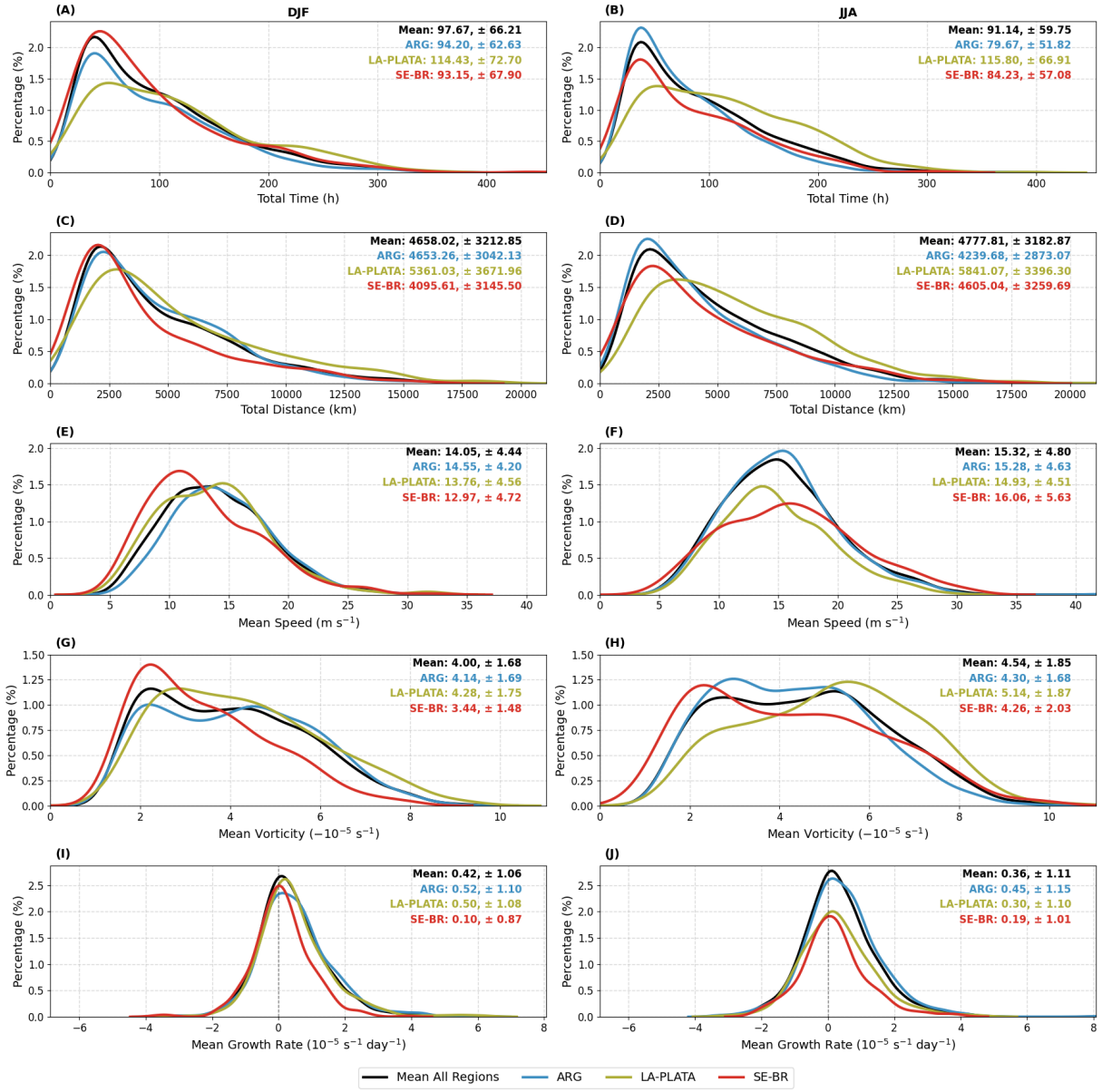


Figure 4.6: Probability density functions (PDF) comparing cyclone lifecycle metrics across different genesis regions (ARG, LA-PLATA, SE-BR) for DJF and JJA. Each panel displays the density distributions for a specific metric: total time (A and B), total distance (C and D), mean speed (E and F), mean vorticity (G and H), and mean growth rate (I and J). The lines in each graph represent the mean values for all regions combined (black), ARG (blue), LA-PLATA (green), and SE-BR (red), while the annotations represent the mean and standard deviation values.

lopment stages, and their use of relative vorticity at 10m, impacted by surface drag, could account for variations in propagation speed.

The analysis reveals notable inter-regional variability in cyclone behavior, with trends predominantly mirroring those observed in the ARG region, which accounts for the highest frequency of cyclone occurrences within the SESA region (Figure 4.1). When examining to-

tal cyclone duration, distinct seasonal patterns emerge: both the ARG and SE-BR regions exhibit significantly shorter lifespans during JJA compared to DJF, with the probability density functions (PDFs) peaking at approximately 50 hours. In contrast, the LA-PLATA region shows slightly longer durations during JJA, with a mean difference of about 1.5 hours. Additionally, the distribution of cyclone durations in the LA-PLATA region is more right-skewed than in ARG and SE-BR, indicating greater variability in the lifespan of cyclones originating from LA-PLATA. Across all regions, the standard deviation decreases from DJF to JJA, suggesting a higher occurrence of longer-lasting cyclones during the summer months.

In terms of displacement, the ARG region displays shorter average distances during DJF compared to JJA, whereas LA-PLATA and SE-BR exhibit increases, particularly notable in SE-BR. Similar to the trends in duration, the displacement patterns in ARG and SE-BR exhibit distinct peaks at approximately 2500 km, while LA-PLATA shows a more right-skewed distribution, especially during JJA, indicating greater variability in cyclone travel distances. These regional differences in displacement are also mirrored in the average propagation speeds of the cyclones: during DJF, cyclones in ARG generally move faster than those in LA-PLATA and SE-BR. This changes in JJA, with SE-BR exhibiting the highest increases in speed, making it the region with the most mobile cyclones during this season, followed by ARG and then LA-PLATA. This variation is reflected in the PDFs for each region: during DJF, SE-BR's propagation speed peaks at approximately 10 m s^{-1} and ARG at 13 m s^{-1} , while LA-PLATA displays a bimodal distribution with peaks at approximately 10 m s^{-1} and 15 m s^{-1} . During JJA, the peak for ARG shifts to approximately 16 m s^{-1} , and LA-PLATA's distribution changes to peak at around 14 m s^{-1} , while SE-BR assumes a bimodal shape, peaking at roughly 10 m s^{-1} and 16 m s^{-1} .

The PDFs for the mean vorticity values of the examined systems display a bimodal, right-skewed distribution with peaks near $2 \times 10^{-5} \text{ s}^{-1}$ and $4 \times 10^{-5} \text{ s}^{-1}$, with a higher occurrence percentage near the first peak and an average value of $4 \pm 1.68 \times 10^{-5} \text{ s}^{-1}$ during DJF (Figure 4.6g). In JJA, the peaks are positioned near $2 \times 10^{-5} \text{ s}^{-1}$ and $5 \times 10^{-5} \text{ s}^{-1}$, but with a higher occurrence percentage at the second peak, reflecting an overall increase in mean vorticity, especially in the LA-PLATA region (Figure 4.6h). The ARG region presents a PDF mirroring the mean cyclone behavior, and SE-BR peaks near $2 \times 10^{-5} \text{ s}^{-1}$ in both seasons, being more right-skewed in JJA, which reflects the occurrence of weaker

systems in this region. Meanwhile, LA-PLATA shifts from being right-skewed in DJF to left-skewed in JJA, reflecting a significant increase in the intensity of systems in this region. These results highlight the previous findings that LA-PLATA presents the most intense systems in the SESA regions, while SE-BR, the weakest (Simmonds and Keay, 2000; Reboita et al., 2010; Gramcianinov et al., 2019). Although the regional and seasonal variability largely corroborates findings from Gramcianinov et al. (2019), the intensity of cyclones reported here is somewhat smaller, possibly due to the ERA5 dataset be able to detect less intense systems (Gramcianinov et al., 2020).

The mean growth rate distribution, is symmetric around zero with a low standard deviation, indicating a dynamic equilibrium in system intensity throughout the life cycle, marked by neither consistent intensification nor weakening, which will be later discussed for each individual phase. It is important to note that these values were computed from normalized relative vorticity data, where positive values suggest system intensification (ζ_{850} increasing in magnitude), while negative values indicate a decay (ζ_{850} decreasing in magnitude). Overall, although the differences are minimal, the results suggest slightly more intense intensification during DJF (Figure 4.6i) compared to JJA (Figure 4.6j), with the latter exhibiting higher mean values.

4.1.3 Life Cycle Phase Statistics

This section examines the statistical characteristics of cyclones, exploring various metrics describing cyclonic behavior throughout distinct lifecycle phases. This unique approach is enabled by the Cyclophaser program, offering a more granular analysis than previously available in the literature. As shown in Section 4.1.2, the region mean results predominantly reflect the ARG region's behavior and hence, region-specific results are detailed here.

Figure 4.7 displays the PDFs for the mean total time spent in each development phase. These PDFs are right-skewed, indicating high variability across different phases but smaller seasonal and regional differences. Typically, the incipient, mature, and second mature phases show the shortest average durations, often peaking between 3 and 5 hours. The intensification, second intensification, and decay phases often exhibit longer tails, suggesting a wide variability in their durations. In the ARG region, all phases show a slight reduction in mean duration from DJF (Figure 4.7a) to JJA (Figure 4.7b), with decay and second

decay stages exhibiting the most significant reductions, indicating that shorter average total durations in JJA are primarily due to these phases (Figure 4.6). For LA-PLATA and SE-BR, notable changes include particularly variations in the standard deviations of the second intensification and decay phases, and in the decay phase for SE-BR, suggesting that seasonal differences in total mean durations for these regions are largely attributable to fluctuations in extreme values.

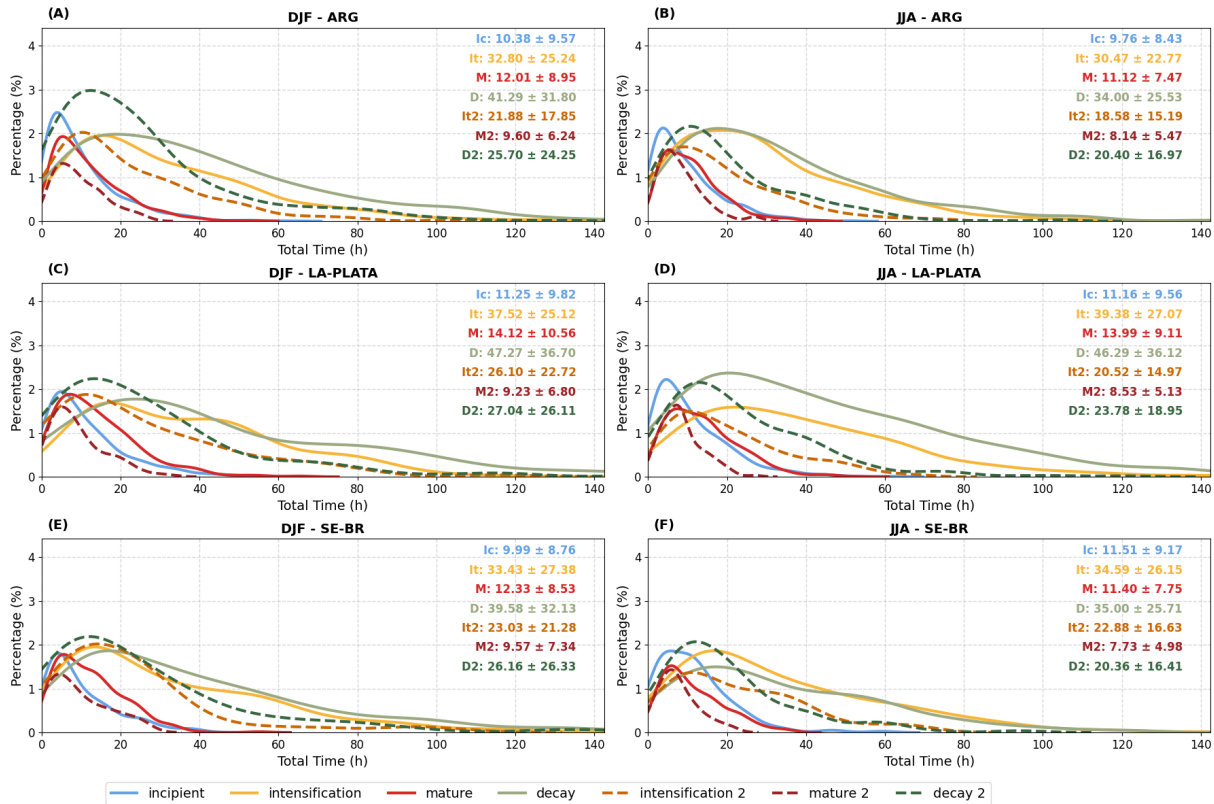


Figure 4.7: Probability density functions (PDF) comparing the mean total duration of each cyclone phase, across all regions combined and for each genesis region (ARG, LA-PLATA, SE-BR) for DJF and JJA. Annotations display mean and standard deviation values for each phase.

The total traveled distance for each phase is depicted in Figure 4.8, which mirrors the overall behavior observed for total time (Figure 4.7). All PDFs are right-skewed, and across all regions and seasons, the incipient, mature, and second mature phases peak approximately between 300 and 400 km, while the other phases present long tail distributions. In the ARG region, there is an overall reduction in traveled distance across all phases from DJF to JJA. Conversely, for LA-PLATA and SE-BR, there is a general increase, reflecting the seasonal behavior for the entire lifecycle's total distance (Figure 4.6).

The results for mean speed (Figure 4.9) aggregate the results for total time and traveled

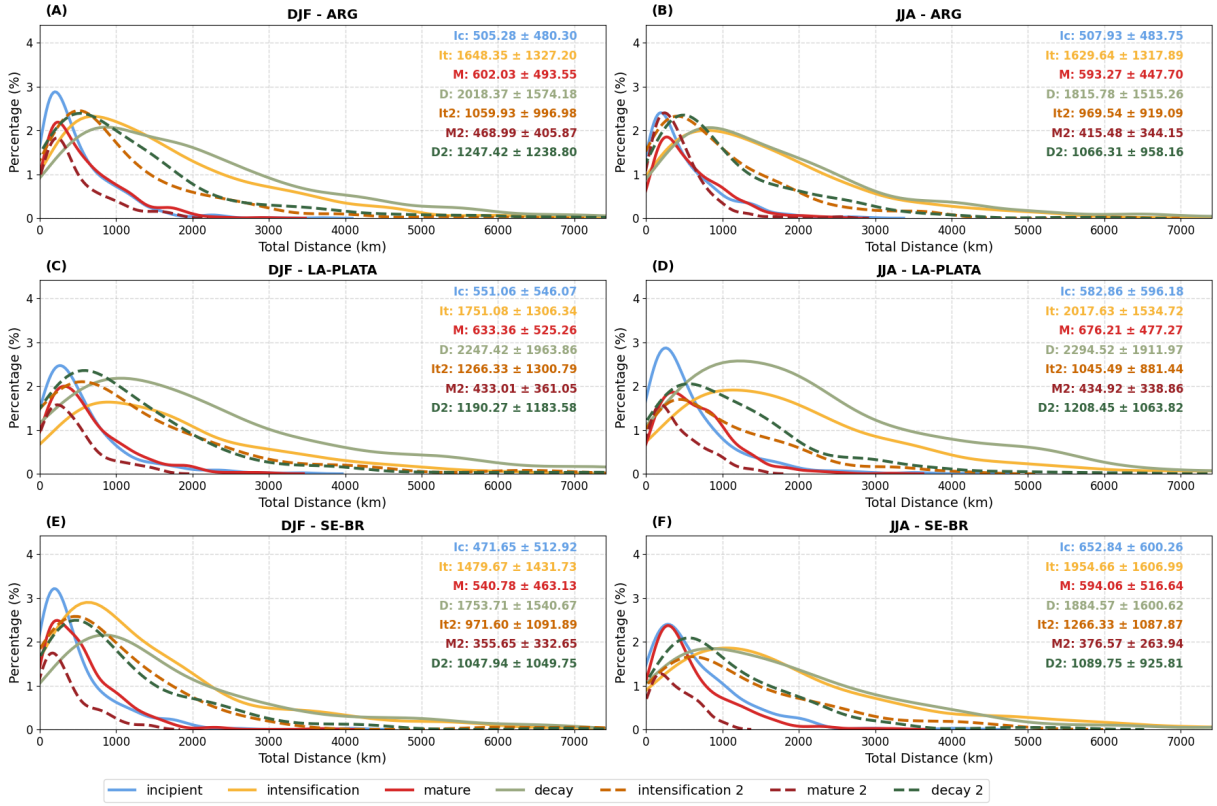


Figure 4.8: Similar to Figure 4.7, but for total traveled distance.

distance. There is less variability across distinct phases for this metric when compared to the total time and distance, with the PDFs for distinct phases, regions, and seasons often presenting a Gaussian-like shape centered between 10 and 15 ms^{-1} . These values align with those found in previous studies (Gramcianinov et al., 2019, 2020; Hoskins and Hodges, 2005), although slightly higher, likely due to the constraints adopted in this analysis. Additionally, this study's ability to account for distinct developmental phases provides a foundation for further research into the dynamical mechanisms that could be linked to the systems' varying speeds across different periods. In the ARG region, the largest increases in mean propagation speed from DJF to JJA are found in the secondary development phases, accompanied by increases in standard deviation values, with slightly right-skewed PDFs for these phases. LA-PLATA displays a similar behavior, especially for intensification and mature decay, which shifts their peaks from near 10ms^{-1} in DJF to near 15ms^{-1} in JJA. For SE-BR, the major change is in the shape of the PDFs, which change from a Gaussian-like shape in DJF to a more right-skewed shape in JJA. Overall, although the differences are only marginal, the cyclones tend to be faster in the incipient stage and in

the intensification stage, being slower at the mature phase, speeding up again in the decay phase. Also, the systems tend to be slower in the second development cycle than in the first one, especially slower at the second mature phase. Therefore, cyclones in the SESA region are slower at their mature phases. The slower propagation speed of cyclones is related to extreme wave occurrence (Gramcianinov et al., 2023) and therefore the positioning of these systems during that phase are of importance for coastal management in the South American Southeastern coast.

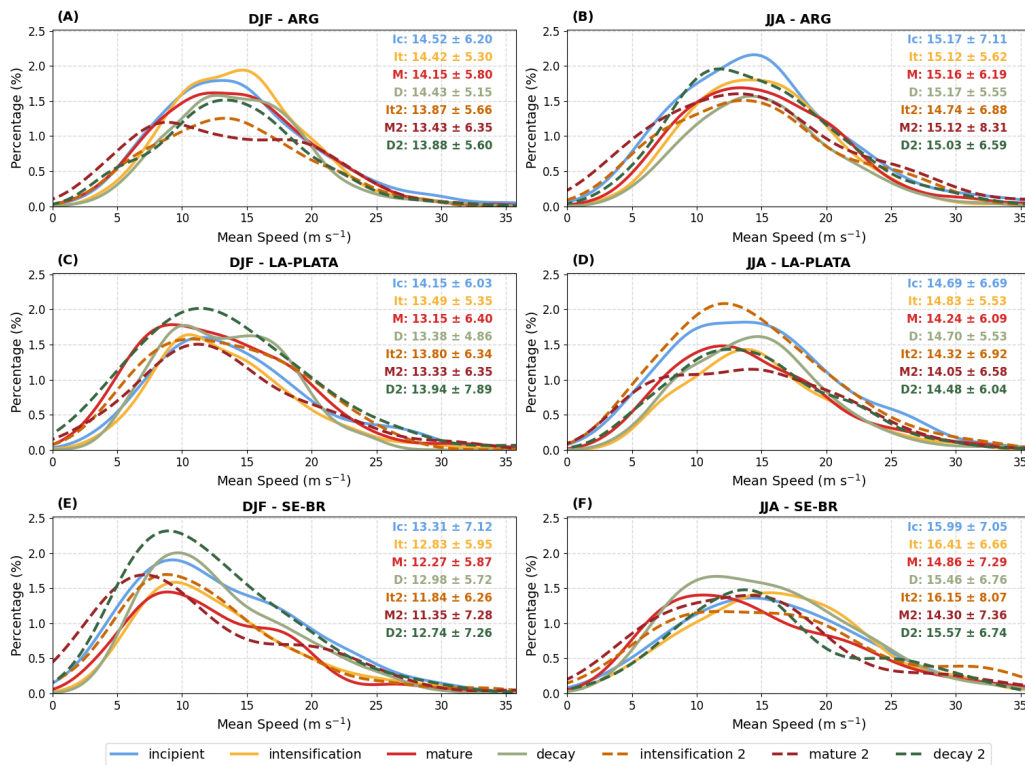


Figure 4.9: Similar to Figure 4.7, but for mean propagation speed.

The PDFs for mean central ζ_{850} across various cyclone phases exhibit bimodal and right-skewed distributions, with a general increase in mean vorticity from DJF to JJA (Figure 4.10). This trend reflects the heightened intensity of cyclonic systems during JJA compared to DJF (Figure 4.6). It is important to note that these vorticity values are derived from the raw output of the TRACK program, and as such, they may include some level of noise that can influence the statistical results. Notably, the mature phase is characteristically the most intense during the first developmental cycle across all regions, demonstrating a wide range of vorticity values and highlighting the variability in peak intensities of mature

cyclones. Meanwhile, the second mature phase typically records the highest vorticities among all phases, suggesting a tendency for systems to intensify further during subsequent cycles. In contrast, the incipient phase generally exhibits the lowest mean vorticities, reflecting the nascent stages of cyclone development. However, in the SE-BR region, this phase shows unusually high mean vorticities during JJA, occasionally surpassing other phases, indicating exceptionally conducive conditions for early cyclone formation. The intensification and decay phases generally present similar mean vorticities, aligning with their respective roles in modifying system intensity: intensification increases vorticity from a baseline state, while decay reduces it back towards this baseline. Secondary intensification and decay phases often exhibit higher mean vorticities than their initial counterparts, reflecting the dynamics of re-intensification in the lifecycle, particularly marked by the higher mean values observed during the second mature phase.

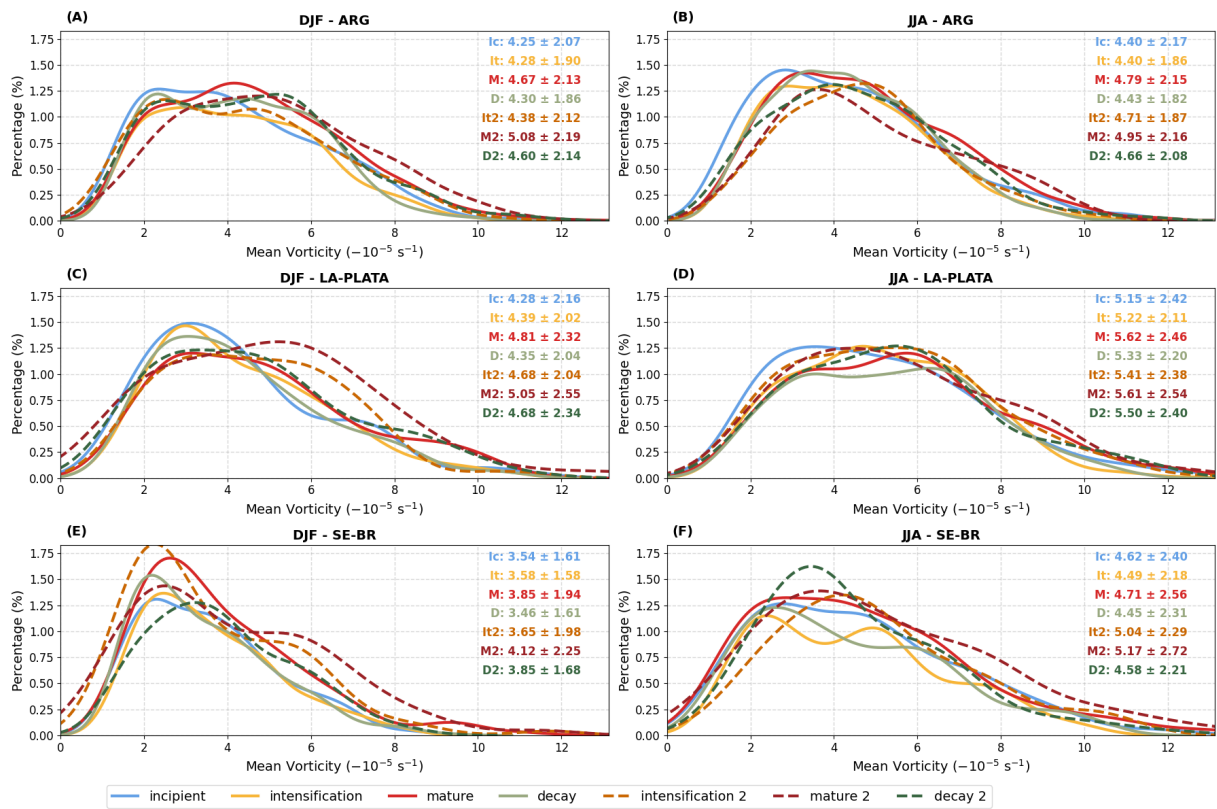


Figure 4.10: Similar to Figure 4.7, but for mean central relative vorticity at cyclone center (ζ_{850}).

The results found here for the incipient stage exhibit higher vorticities compared to the initial vorticities reported by Reboita et al. (2010), Gramcianinov et al. (2019), and Gramcianinov et al. (2020). This discrepancy may be attributed to our exclusion criteria,

which likely excluded weaker and underdeveloped systems, coupled with the observed tendency for vorticity to increase (becoming more negative) when an incipient stage is followed by an intensification phase (e.g., Figure 4.4a and c), potentially resulting in a bias toward higher values for this phase. Additionally, Sinclair (1995), in their analysis focusing on the first time step, the time step of minimum vorticity, and the last time step, reported higher vorticity values compared to our findings for the incipient, mature, and decay stages. However, these authors omitted the influence of topography by using geostrophic relative vorticity, which justifies the difference in vorticity distribution observed in their study.

There are complexities in interpreting the results for the mean growth rate due to the use of raw vorticity data from the TRACK algorithm, which introduces additional noise to the findings (Figure 4.11). This metric exhibits considerable variability across different regions, with most PDFs centered around zero yet displaying wide variations, where standard deviations significantly exceed the mean values. The incipient stage often shows the highest or second-highest growth rates, typically skewing more to the right. These observations are consistent with previously reported mean growth rates for cyclogenesis regions by Hoskins and Hodges (2005) and Gramcianinov et al. (2019). A similar pattern is observed in the intensification phase, which alternates with the incipient stage in displaying the greatest growth rates. Despite positive average values, the decay and second decay phases predominantly peak at negative values, reflecting their role in diminishing system vorticity.

While most regions and seasons show the mature phase peaking at zero — expected due to its position near local vorticity minima — the positive mean suggests that the increase in vorticity preceding the peak is more pronounced than the subsequent decline. This assertion is supported by the lower mean values observed during the decay phase compared to the intensification phase. Moreover, the detection of the mature phase often occurs between the peaks and valleys of vorticity derivatives (Section 3.3.1), potentially shifting its center of mass toward either the intensification or decay stages, as depicted in Figure 4.12. During JJA in LA-PLATA, the mature phase peaks positively, whereas in SE-BR during DJF, it peaks negatively. Determining whether these shifts are due to greater increases in intensity, displacement of the phase's center of mass, or residual data noise is beyond this study's scope.

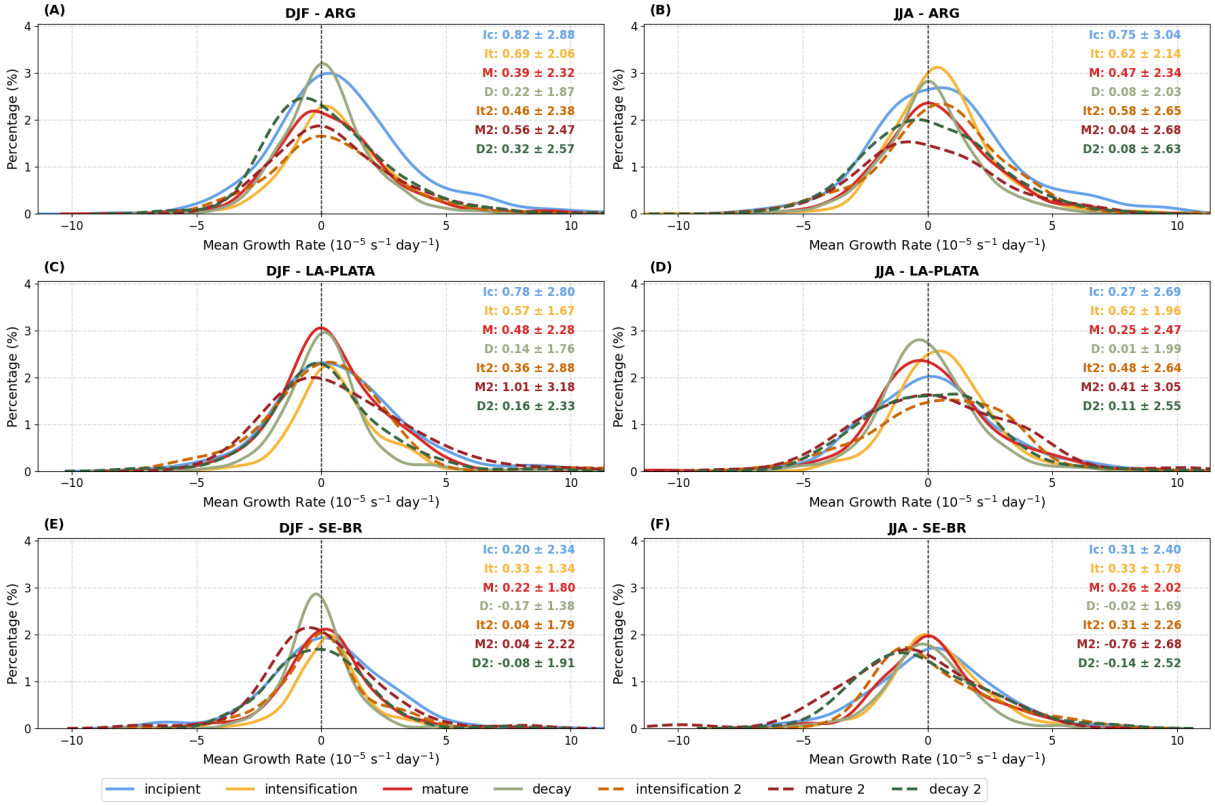


Figure 4.11: Similar to Figure 4.7, but for mean growth rate.

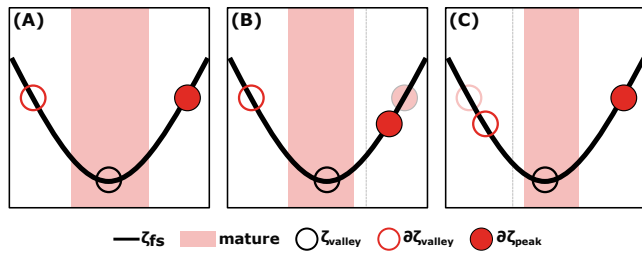


Figure 4.12: Illustrative example of how the center of mass of the mature phase can be displaced: (A) Symmetrically around the vorticity valley ($\partial\zeta_{valley}$) when distances to the first derivative valley ($\partial\zeta_{valley}$) and peak ($\partial\zeta_{peak}$) are equal. (B) Displacement towards the previous phase when $\partial\zeta_{peak}$ is closer to ζ_{valley} . (C) Displacement towards the subsequent phase when $\partial\zeta_{valley}$ is closer to ζ_{valley} .

4.2 Spatial Distribution of Cyclone Life Cycle Phases

The current section explores the spatial distribution across the SESA region of the distinct phases of cyclone development: incipient (Section 4.2.1), intensification (Section 4.2.2), mature (Section 4.2.3), decay (Section 4.2.4) and the secondary development cycle, as well the residual phase (Section 4.2.5). The analysis focuses only on systems that presented a mature phase to avoid including underdeveloped systems, those that might not have exhibited a mature phase before leaving the tracking domain, or cases where the maturation stages were shorter than the CycloPhaser's threshold for detecting this phase (as discussed in Section 4.1.1). The track density ranges differ from one figure to the other as does not make sense to compare track density between distinct phases, as those differ in duration and in total displacement (Section 4.1.3).

4.2.1 Incipient Phase

Figure 4.13 illustrates cyclone track density (cyclones per 10^6 km^2 per month) during the incipient phase for DJF and JJA in the SESA region. Given that transitional seasons display intermediate characteristics between these extremes (Gan and Rao, 1991; Reboita et al., 2010; Crespo et al., 2021, e.g.,), our analysis primarily focuses on DJF and JJA, encompassing the cyclogenesis regions of ARG, LA-PLATA, and SE-BR. As expected, the track density for the incipient phase correlates with these genesis regions (Figure 4.13a and b).

The ARG region consistently shows similar track densities in both DJF (Figure 4.13c) and JJA (Figure 4.13d), exceeding 30 cyclones per 10^6 km^2 per month. In contrast, LA-PLATA and SE-BR regions exhibit noticeable seasonal patterns. LA-PLATA sees increased activity in JJA (Figure 4.13f) compared to DJF (Figure 4.13e), with densities rising above 20 and 10 cyclones per 10^6 km^2 per month, respectively. Conversely, SE-BR demonstrates higher activity in DJF (Figure 4.13g) than in JJA (Figure 4.13h), with densities exceeding 10 and 8 cyclones per 10^6 km^2 per month, respectively. This seasonality is consistent with findings from previous studies (Gan and Rao, 1991; Hoskins and Hodges, 2005; Mendes et al., 2010; Reboita et al., 2010; Gramcianinov et al., 2019; Crespo et al., 2021). Variations in reported track density values by (Gramcianinov et al., 2020, 2019) may arise from different methodologies; those studies analyzed only the initial time step of the system life

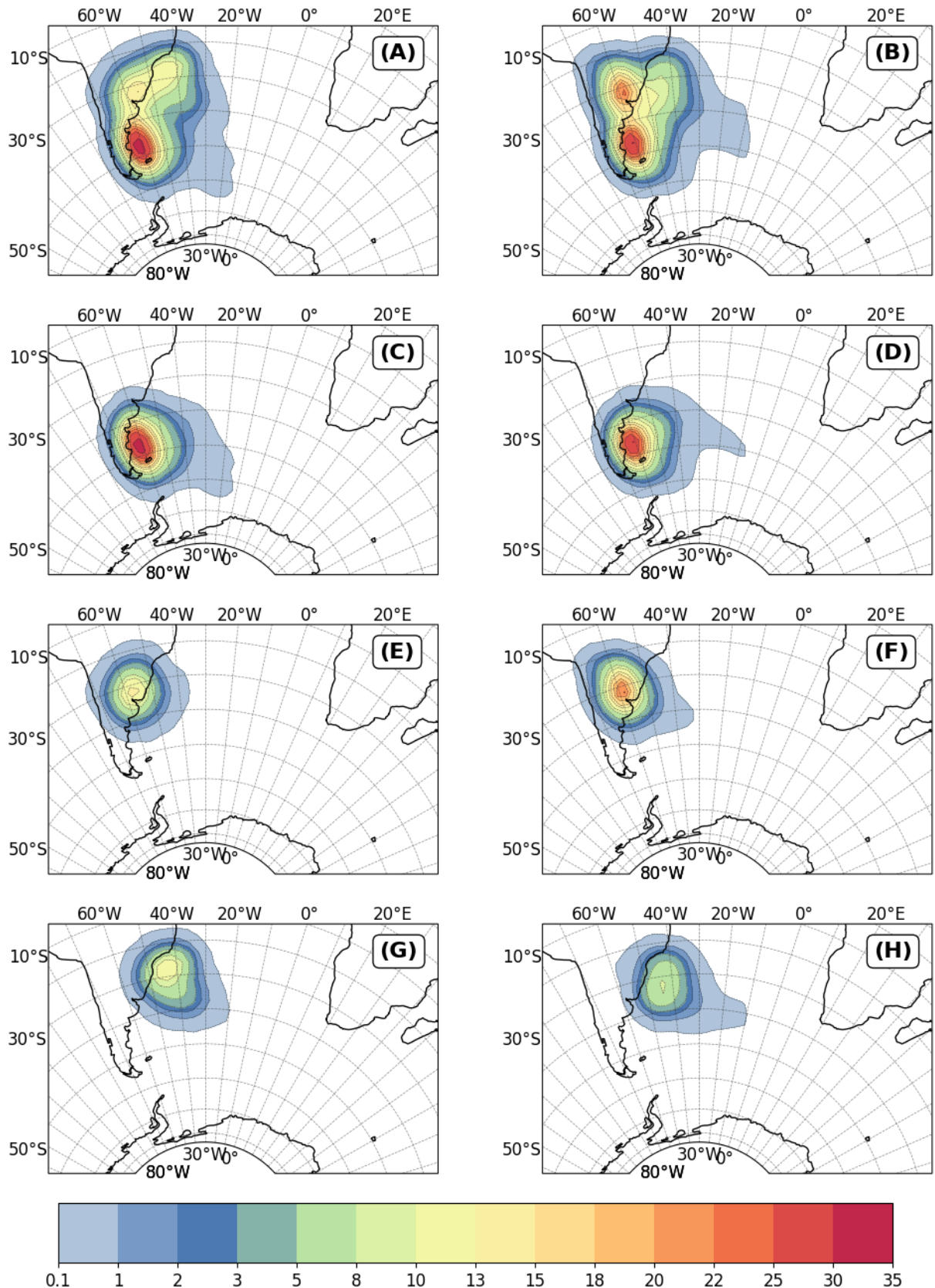


Figure 4.13: Cyclone track density during the incipient phase for all systems with genesis in the ARG, LA-PLATA and SE-BR regions. Panels A and B show the aggregate density across all regions for DJF and JJA, respectively. Panels C to H depict individual genesis regions: ARG (C and D), LA-PLATA (E and F), and SE-BR (G and H) for DJF (left panels) and JJA (right panels). The unit is cyclones per 10^6 km^2 per month.

cycle, while this study considers all periods classified as the incipient stage. Additionally, Gramcianinov et al. (2019) utilized the NCEP-CFSR reanalysis database for tracking, in contrast to the ERA5 dataset employed here.

4.2.2 Intensification Phase

The track densities during the intensification phase (Figure 4.14) exhibit significantly higher values compared to the incipient stage. This is expected due to the longer duration of the intensification phase, as discussed in Section 3.3.1. Across all genesis regions, during both DJF (Figure 4.14a) and JJA (Figure 4.14b), the maximum track density extends from approximately 60°W to 20°W. The central concentration around 50°S, particularly during both seasons, is primarily composed of systems originating in the ARG region (Figure 4.14c and d). During DJF, the maximum density region, extending eastward/southeastward from the incipient stage, reaches up to 100 cyclones per 10^6 km^2 per month, while in JJA, it shows a slight decrease to 80 cyclones per 10^6 km^2 per month, with a predominantly eastward orientation. The higher track density and the cyclones reaching further east in DJF can be attributed to the longer mean duration of the intensification phase for systems from ARG, as shown in Figure 4.7, and the overall greater displacement distances during this phase across all genesis regions, as indicated in Figure 4.8.

Moreover, the maximum track density at around 50°S for the ARG region connects with the track densities for the LA-PLATA and SE-BR regions. LA-PLATA shows higher activity during JJA (Figure 4.14f), with track densities reaching 50 cyclones per 10^6 km^2 per month, compared to 40 during DJF (Figure 4.14e). Conversely, SE-BR exhibits higher activity during DJF (Figure 4.14g), with densities reaching 40 cyclones per 10^6 km^2 per month, compared to 20 during JJA (Figure 4.14h). This seasonality for both LA-PLATA and SE-BR regions reflects the seasonality in cyclogenesis (Figure 4.1) and consequently, of the incipient phase (Figure 4.13). Consequently, in the aggregate densities for all regions during DJF (Figure 4.14a), the SE-BR region's signal is more apparent near 30°S and 40°W. In JJA (Figure 4.14b), the track density associated with LA-PLATA is evident as the maximum track region extends southeastward from near 35°S and 55°W (Figure 4.14f). Furthermore, for the LA-PLATA region, it can be seen that during JJA, the systems tend to reach further southeast, associated with higher mean displacements (Figure 4.8).

Notably, the track densities for the intensification phase across all genesis regions show

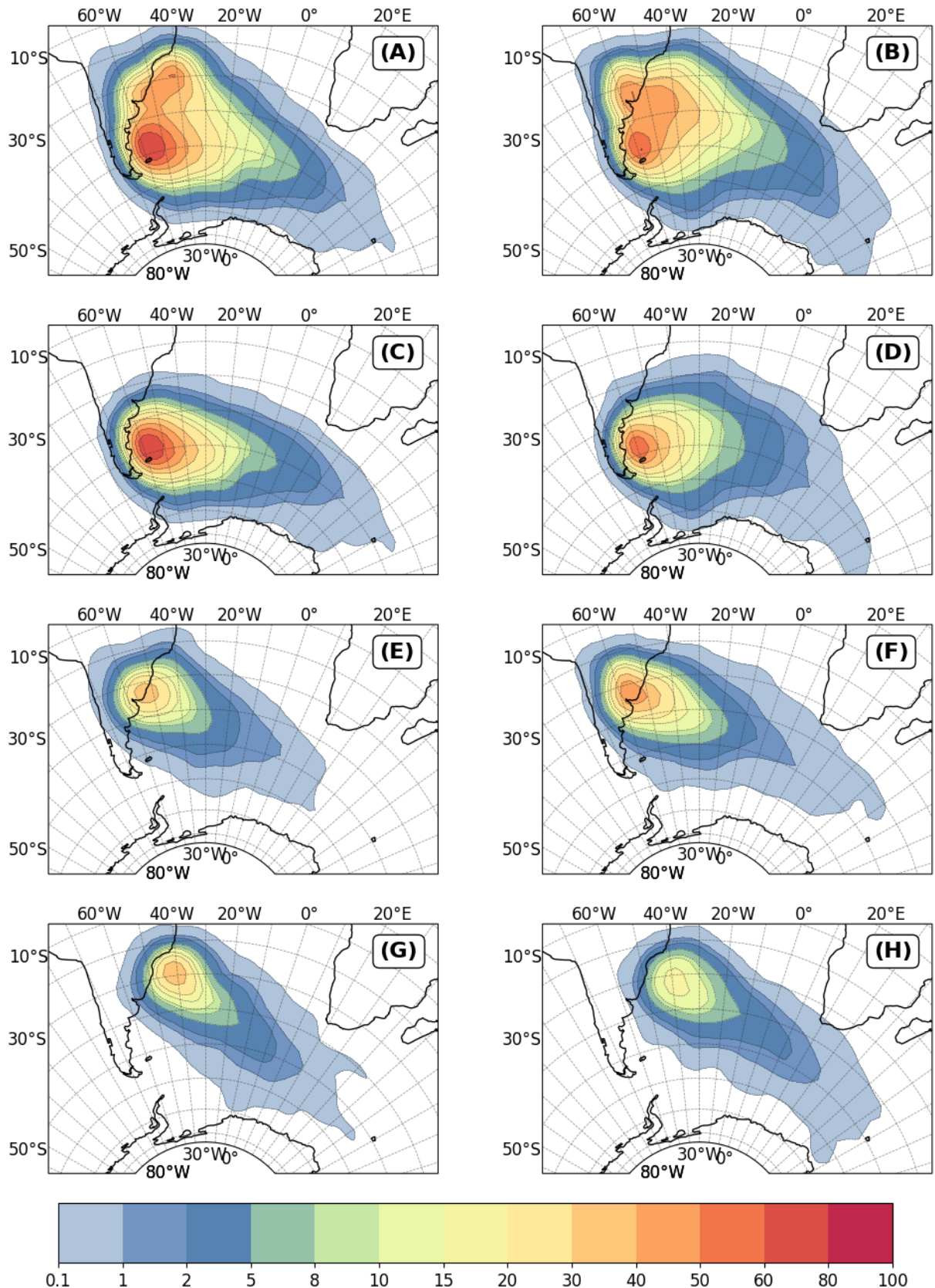


Figure 4.14: Cyclone track density during the intensification phase for all systems with genesis in the ARG, LA-PLATA and SE-BR regions. Panels A and B show the aggregate density across all regions for DJF and JJA, respectively. Panels C to H depict individual genesis regions: ARG (C and D), LA-PLATA (E and F), and SE-BR (G and H) for DJF (left panels) and JJA (right panels). The unit is cyclones per 10^6 km^2 per month.

far-reaching systems that intensify throughout the entire South Atlantic basin, extending as far as 30°E or even 60°E. While the orientation of the track density for the ARG region is predominantly eastward, for LA-PLATA and SE-BR, the tracks are southeastward oriented. This results in a concentration of track densities between 40°S and 60°S, displaced more northward during JJA than DJF, indicating a preference for systems to intensify in this region, which corresponds to the storm track path for the South Atlantic (Hoskins and Hodges, 2005; Gramcianinov et al., 2019).

4.2.3 Mature Phase

In the mature phase, there is a notable reduction in track densities compared to the intensification phase, with maximum values decreasing from 100 to 20 cyclones per 10^6 km^2 per month. During DJF, the aggregate for all genesis regions shows two principal maximum track density areas (Figure 4.15a). The first area, centered near 35°S and 45°W, exhibits a lower maximum track density reaching 14 cyclones per 10^6 km^2 per month, predominantly associated with cyclones originating in the LA-PLATA and SE-BR regions (Figures 4.15e and 4.15g). The second area, located near 55°S and 30°W, reaches up to 18 cyclones per 10^6 km^2 per month and is primarily associated with systems from the ARG region (Figure 4.15c). During this season, maximum track densities for ARG, LA-PLATA, and SE-BR peak at 16, 9, and 10 cyclones per 10^6 km^2 per month, respectively.

In JJA, the primary track density maximum for the aggregate is located near 45°S and 45°W, slightly westward compared to the DJF maximum, with secondary maxima to the north and northeast, each reaching 12 cyclones per 10^6 km^2 per month (Figure 4.15b). This lower density compared to DJF reflects shorter mature phase durations and reduced mobility of systems from the ARG region during JJA, as shown in Figures 4.7 and 4.8. Notably, the track density center for the ARG region shifts from near 45°W during DJF to around 55°W during JJA (Figure 4.15d), indicating a tendency for systems to mature closer to their intensification locations, which is also indicated by the lower mobility of these systems when compared to the other genesis regions for this period (Figure 4.8). Secondary maxima near 35°S and 45°S result from overlaps in tracks from all regions, with LA-PLATA contributing significantly (Figure 4.15f). Although this overlaps with a center from SE-BR, the track density maximum for SE-BR during JJA remains low, not exceeding 5 cyclones per 10^6 km^2 per month (Figure 4.15h), while for LA-PLATA, it reaches up to 7

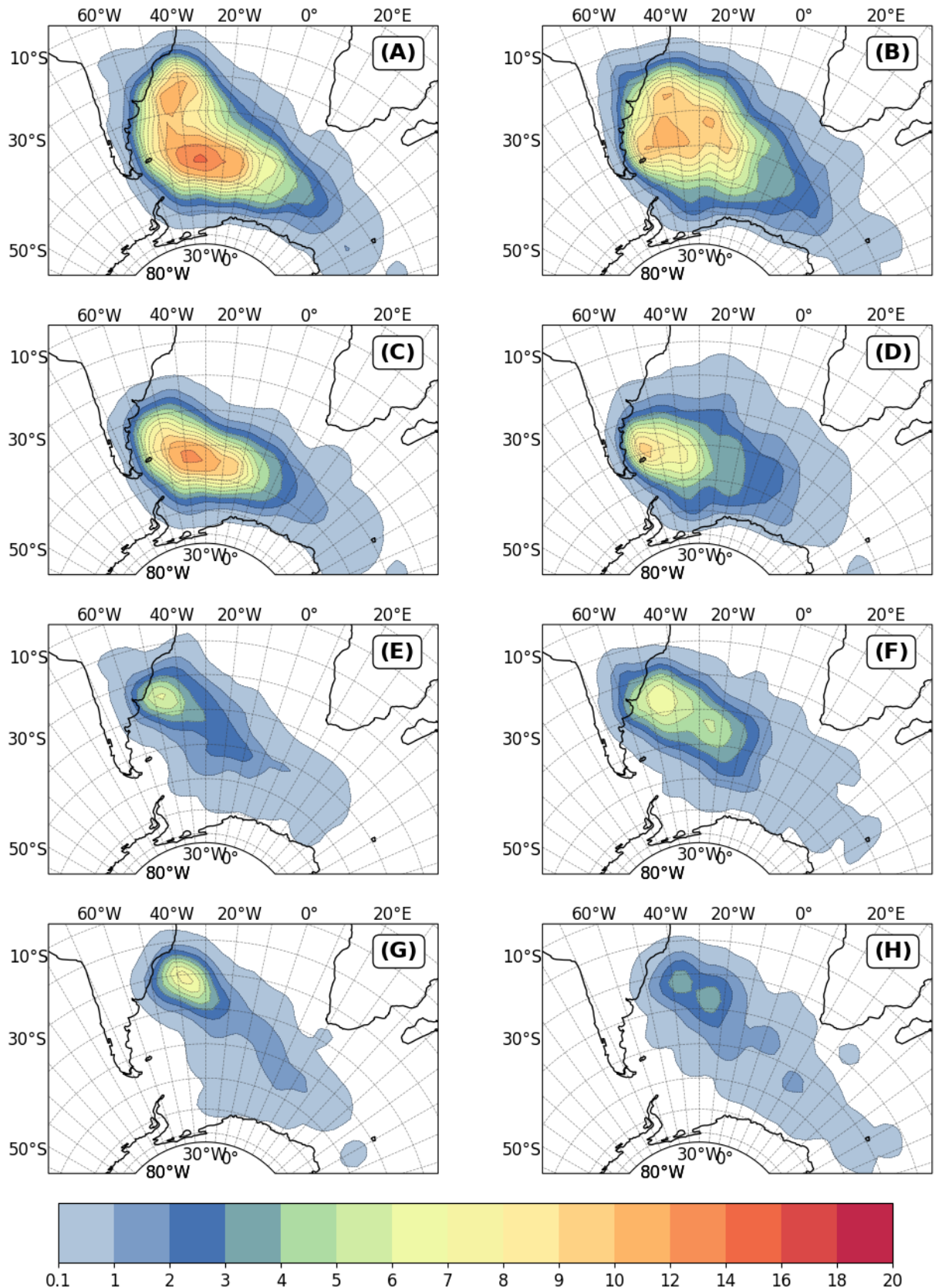


Figure 4.15: Cyclone track density during the mature phase for all systems with genesis in the ARG, LA-PLATA and SE-BR regions. Panels A and B show the aggregate density across all regions for DJF and JJA, respectively. Panels C to H depict individual genesis regions: ARG (C and D), LA-PLATA (E and F), and SE-BR (G and H) for DJF (left panels) and JJA (right panels). The unit is cyclones per 10^6 km^2 per month.

near 55°W and 6 near 45°W.

Overall, the density maximum centers for the mature phase are displaced southeastward from those for the intensification phase for DJF and east/southeastward for JJA. Tracks are typically found between 40°S and 60°S, aligning with the storm track path for the South Atlantic. For DJF, most tracks are located below 50°S, while for JJA, they are predominantly above 50°S. This pattern is more pronounced during the mature phase than during the intensification phase, with the southward shift during DJF largely associated with cyclones originating in the ARG region, while a maximum density region closer to Uruguay and Southern/Southeastern Brazil is mostly linked with LA-PLATA and SE-BR genesis regions.

4.2.4 Decay Phase

The decay phase generally exhibits increased track densities compared to the mature phase, with maximum values reaching 40 cyclones per 10^6 km^2 per month, but still lower than observed during the intensification phase. During DJF, two primary centers of maximum track density are observed: one near 35°S, close to Uruguay and South/Southeastern Brazil (Figure 4.16a), and another near 55°S, west of the Weddell Sea (Figure 4.16a). The latter, primarily influenced by cyclones from the ARG region, reaches up to 35 cyclones per 10^6 km^2 per month (Figure 4.16c). The former, influenced by the LA-PLATA and SE-BR regions, records densities of up to 13 and 30 cyclones per 10^6 km^2 per month, respectively (Figures 4.16e and 4.16g).

For JJA, two primary density maxima are identified: one centered at 45°S, spanning from 60°W to 20°W, and another near 35°S and 40°W, with both areas achieving track densities up to 35 cyclones per 10^6 km^2 per month (Figure 4.16b). The former is predominantly linked to systems from the ARG region, where densities reach 30 cyclones per 10^6 km^2 per month (Figure 4.16d), while the latter is influenced by the SE-BR and especially the LA-PLATA regions, showing densities of 10 and 15 cyclones per 10^6 km^2 per month, respectively (Figures 4.16h and 4.16f). Additionally, a notable center of density, although less pronounced, emerges in the LA-PLATA region, associated with systems that enter an early decay phase (Section 4.2.5).

For the ARG region, the decay phase densities are typically shifted southeastward from those of the mature phase during DJF and mostly southeastward/eastward during JJA,

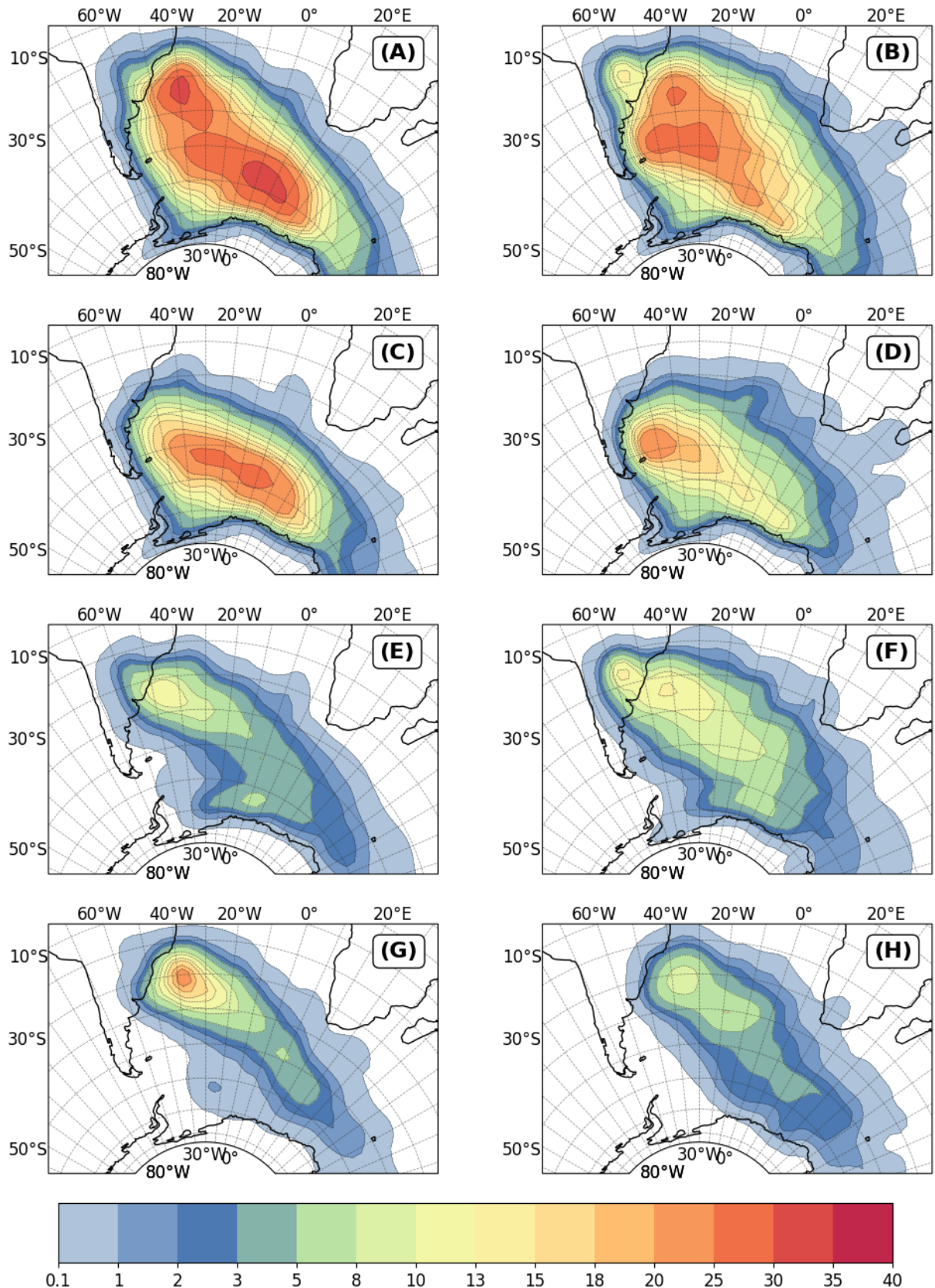


Figure 4.16: Cyclone track density during the decay phase for all systems with genesis in the ARG, LA-PLATA and SE-BR regions. Panels A and B show the aggregate density across all regions for DJF and JJA, respectively. Panels C to H depict individual genesis regions: ARG (C and D), LA-PLATA (E and F), and SE-BR (G and H) for DJF (left panels) and JJA (right panels). The unit is cyclones per 10^6 km^2 per month.

with some systems extending westward to the Weddell Sea. This pattern highlights a seasonal variation in the decay behaviors of systems within the SESA region. Moreover, for both LA-PLATA and SE-BR, decay densities are generally proximate to those of the mature phase but extend further southeastward, reaching as far south as 70°S and as far east as 30°E. This expansive spread into the southern Atlantic aligns with findings by Hoskins and Hodges (2005), who identify the region south of 60°S and west of the Weddell Sea as the primary dissolution area for cyclones in the South Atlantic.

4.2.5 Secondary Development Phases

For analyzing the track densities for the phases related to the systems' secondary development, the results are shown as yearly values rather than by seasonal variability, as done in previous sections. This approach is due to the lower frequency of systems undergoing secondary development compared to those that do not (Figure 4.3). Additionally, as shown in Section 4.1.1, the number of systems presenting early intensification or decay phases is comparable to those with secondary development stages. Therefore, the analysis here focuses on systems that exhibited a complete secondary development cycle: incipient, intensification, mature, decay, intensification 2, mature 2, and decay 2. Figure 4.17 illustrates the track density differences when other life cycle configurations are included in the analysis. The occurrence of early intensification and decay phases impacts the overall track density distribution, with maximum density centers between 30°S and 40°S, centered near 45°W (Figures 4.17a and 4.17c). These centers disappear when the analysis focus only on the systems with a complete secondary development (Figures 4.17b and 4.17d).

For the second intensification phase, there is a maximum track density region south of South Africa, with 30 cyclones per 10^6 km^2 per month (Figure 4.18a). This maximum density region is related to the aggregate occurrence of systems from all genesis regions and closely matches the SE-SAO cyclogenesis region reported by Gramcianinov et al. (2019). Gramcianinov et al. (2019) highlighted a potential link between this region and secondary cyclogenesis. It is possible that some of the detected re-intensifications might stem from secondary cyclogenesis events or spurious links by the TRACK algorithm, which could mix weak decaying systems with incipient secondary cyclones. While secondary cyclogenesis generally follows a frontal wave post an extratropical cyclone's passage (Mailier et al., 2006; Shapiro et al., 1997; Ford et al., 1990; Rivals et al., 1998), the CycloPhaser program

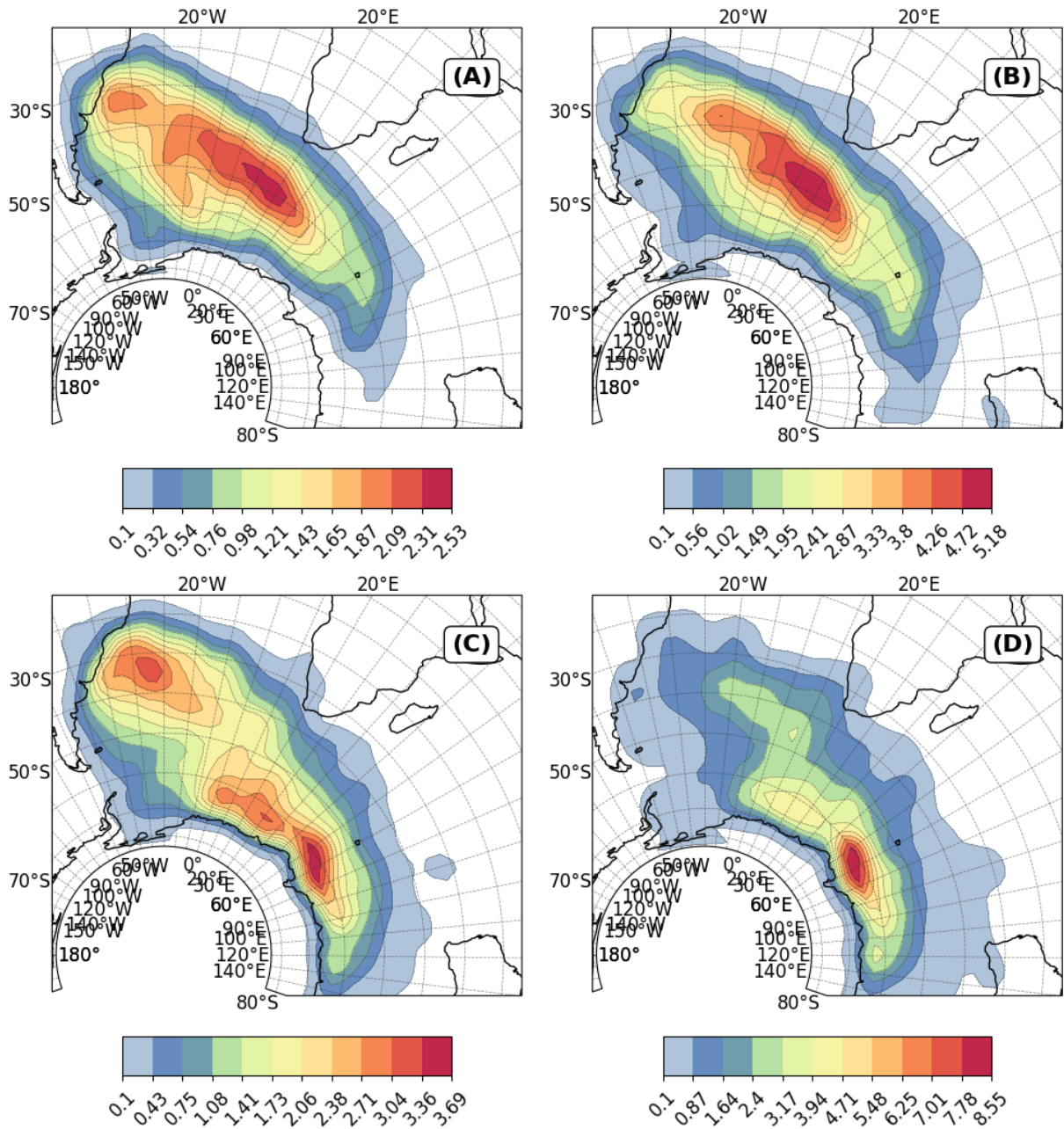


Figure 4.17: Cyclone track density for the secondary development stages. Panels A and B display the phase intensification 2, while panels C and D, phase decay 2. Panels A and C show the results when all life cycle configurations are included in the analysis, while panels B and D show the results when only the systems that exhibited a complete secondary development cycle - incipient, intensification, mature, decay, intensification 2, mature 2, and decay 2 - are analysed. The unit is cyclones per $10^6 \text{ km}^2 \text{ per month}$.

classifies a phase as "intensification 2" whenever the ζ_{850} series indicates a pattern of increases in its magnitude, followed by subsequent mature and decay phases. This secondary intensification could result from a decaying wave at 850 hPa finding favorable conditions for subsequent intensification. Alternatively, the surface cyclone might have already dissipated, but there is still a signal of it in the ζ_{850} field, causing the TRACK algorithm to continue tracking a weak decaying trough at 850 hPa. In these instances, the CycloPhaser may classify this weak intensification as 'residual' should it not progress to a mature stage (Section 3.3.1). Conversely, if the TRACK algorithm mistakenly associates this decaying wave with a newly forming cyclone nearby, the CycloPhaser would label this transition as "intensification 2," introducing potential analysis errors. However, distinguishing between true secondary genesis and re-intensification remains beyond this study's scope. Furthermore, notably, there is a track density maxima near Uruguay and South Brazil associated with LA-PLATA systems.

The second mature phase, characterized by its overall low track density, presents a diffuse spatial distribution. This low track density is primarily due to the infrequent occurrence of secondary development in SESA systems (Figure 4.3) and the fact that it exhibits the lowest displacement and duration across all phases (Figures 4.8 and 4.7). However, a notable maximum track density is centered at 60°S and 50°E, with 2 cyclones per 10^6 km^2 per month (Figure 4.19a). This peak is mainly associated with systems from ARG and SE-BR (Figures 4.19b and 4.19d). A weaker density maximum is found to the west, between 10°E and 20°E, predominantly linked to systems from LA-PLATA (Figure 4.19c). For all regions, the track density regions are mostly displaced southeastward compared to the intensification 2 phase.

The second decay phase displays the systems in their southernmost and easternmost positions, with track densities extending up to 140°E and bordering the Antarctic continent. All three genesis regions present a track density maximum centered between 60°E and 110°E, with the resulting aggregate displaying up to 8.5 cyclones per 10^6 km^2 per month (Figure 4.20a). Individually, each genesis region has a track maximum of approximately 2 to 3 cyclones per 10^6 km^2 per month, with LA-PLATA displaying a second weaker maximum between 20°E and 40°E, with up to 2 cyclones per 10^6 km^2 per month (Figure 4.20c). This region also presents the highest density values northwestwards, contributing to the track densities near 40°S.

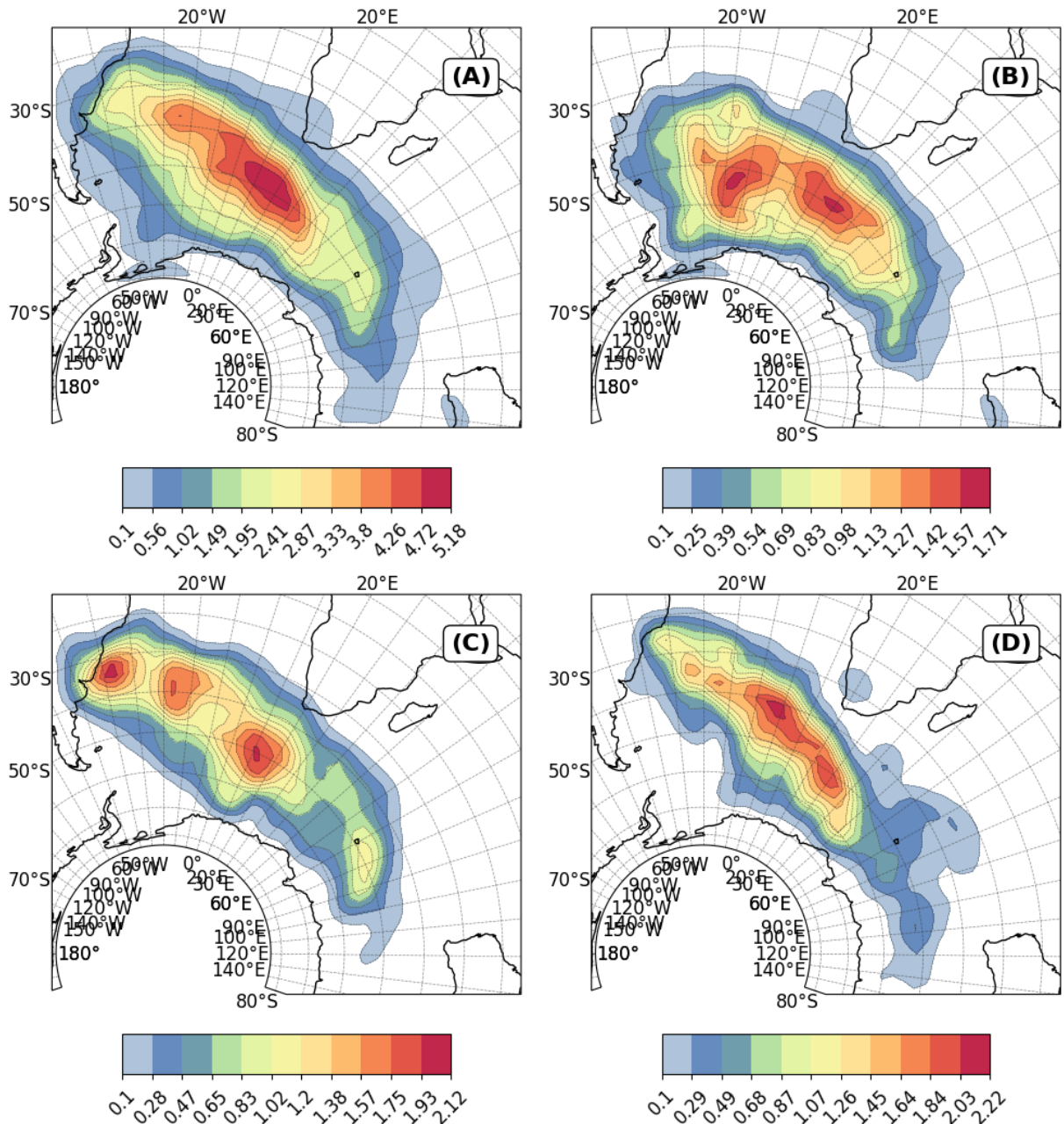


Figure 4.18: Cyclone track density during the second intensification phase for all systems with genesis in the ARG, LA-PLATA and SE-BR regions that display a complete secondary development cycle. Panel A shows the aggregate density across all regions. Panels B to D depict individual genesis regions: ARG (B), LA-PLATA (C), and SE-BR (D). The unit is cyclones per $10^6 \text{ km}^2 \text{ per month}$.

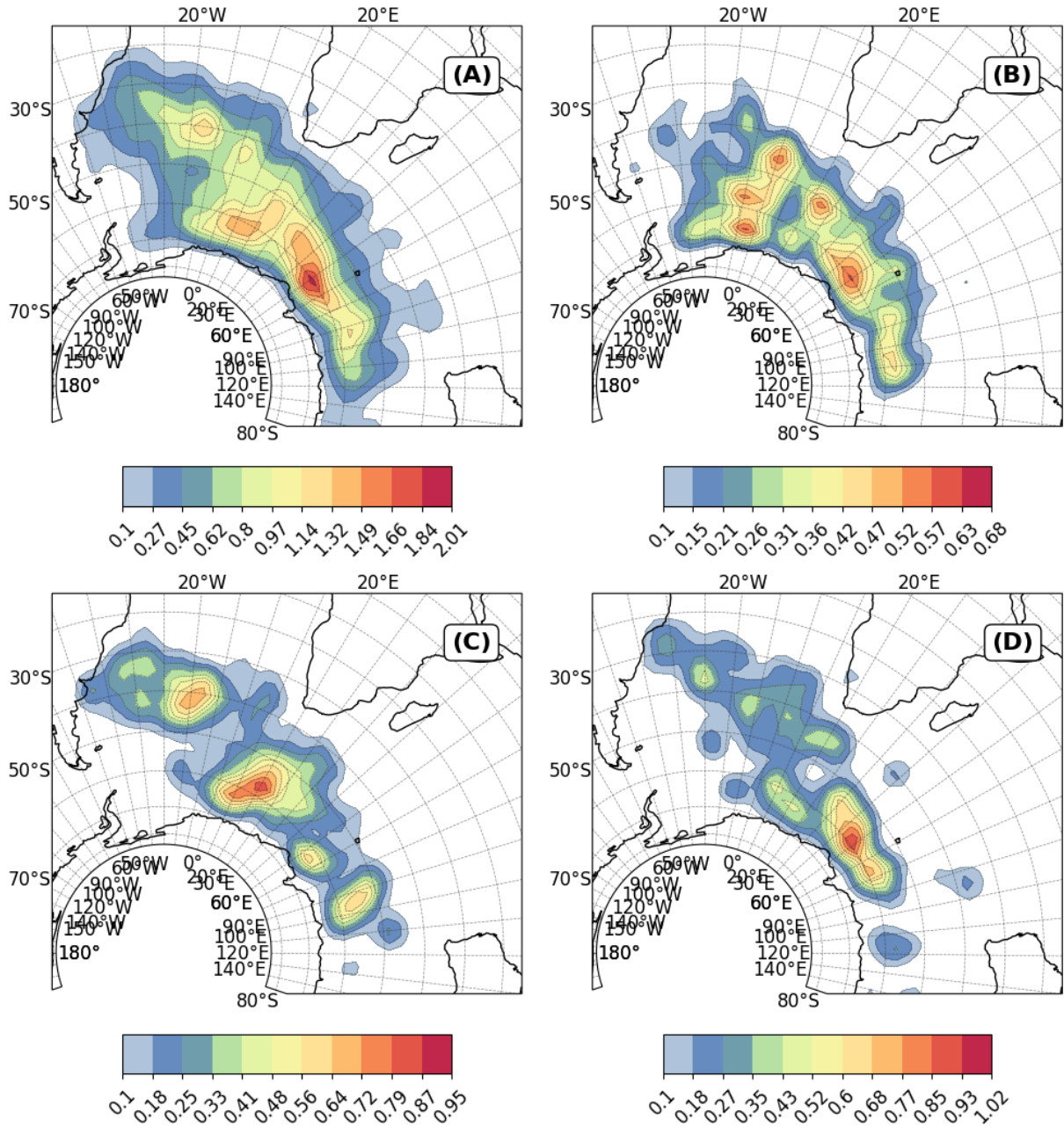


Figure 4.19: Cyclone track density during the second mature phase for all systems with genesis in the ARG, LA-PLATA and SE-BR regions that display a complete secondary development cycle. Panel A shows the aggregate density across all regions. Panels B to D depict individual genesis regions: ARG (B), LA-PLATA (C), and SE-BR (D). The unit is cyclones per 10^6 km^2 per month.

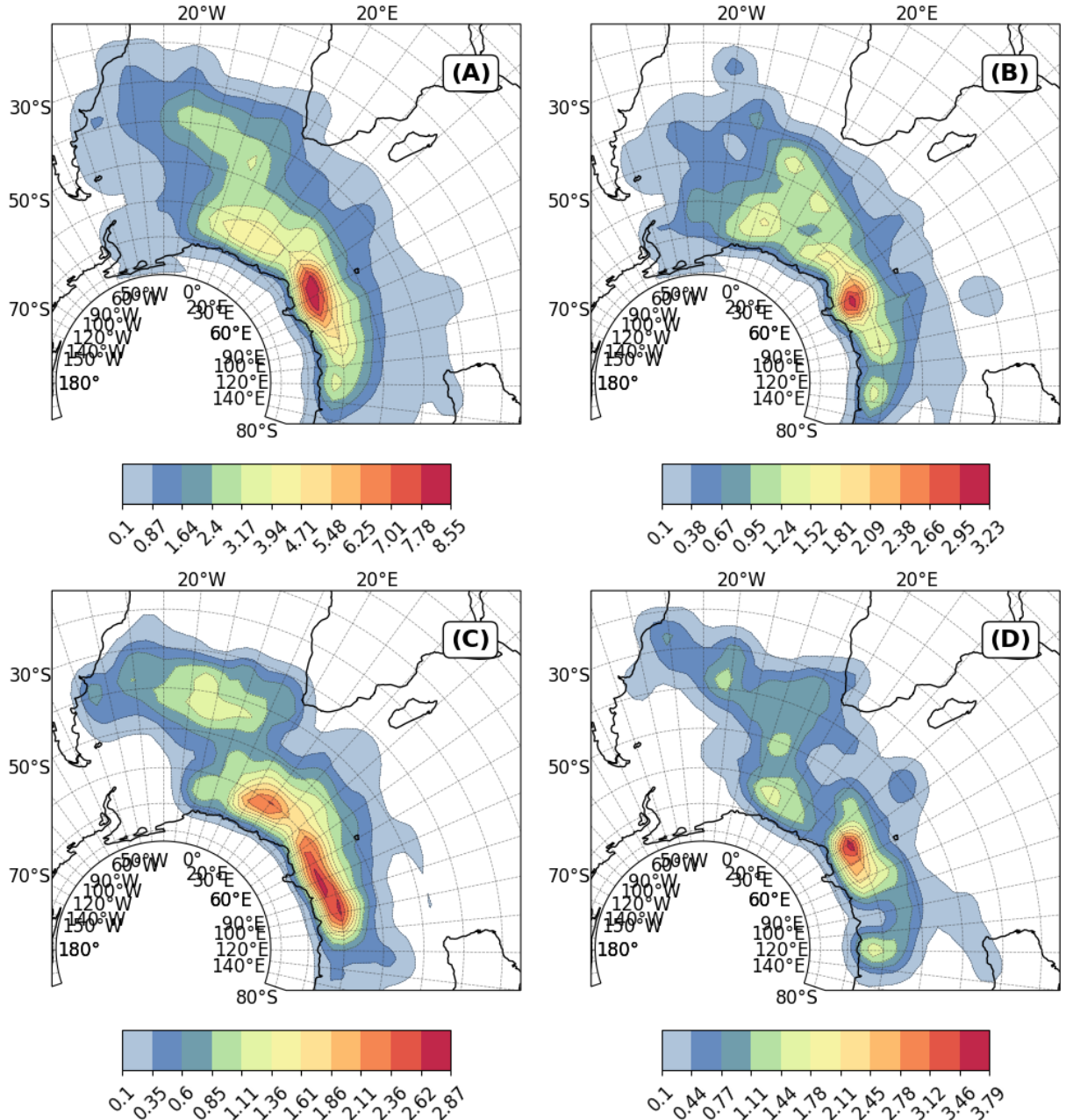


Figure 4.20: Cyclone track density during the second decay phase for all systems with genesis in the ARG, LA-PLATA and SE-BR regions that display a complete secondary development cycle. Panel A shows the aggregate density across all regions. Panels B to D depict individual genesis regions: ARG (B), LA-PLATA (C), and SE-BR (D). The unit is cyclones per $10^6 \text{ km}^2 \text{ per month}$.

Across all second development phases, a weaker albeit noticeable track density region is present near the SE-BR genesis area. This region also shows occurrences of subtropical cyclones Evans and Braun (2012); de Jesus et al. (2022); Cardoso et al. (2022), especially during DJF months, where approximately 30% of the systems exhibit hybrid characteristics Gozzo et al. (2014). Previous works analyzing case studies of such systems that have genesis in the SE-BR region reveal that they present complex life cycles, often transitioning between different types of cyclonic systems and presenting multiple stages of intensification, maturation, and decay (Dias Pinto et al., 2013; Veiga et al., 2008; Reboita et al., 2022; Dutra et al., 2017; Reboita et al., 2021, e.g.,). Consequently, one can speculate that some of the systems related to these track density regions near SE-BR might be subtropical. However, further analysis would be needed for confirm this assertion, which is beyond the scope of the current work.

4.2.6 Residual Phase

The residual phase, though not representing a physical stage of cyclone development, plays an important role in identifying tracking and detection inconsistencies, highlighting potential areas for methodological improvement. This phase typically includes systems that experience temporary intensification due to favorable environmental factors but fail to progress into mature cyclones. Identifying the residual phase involves detecting situations where a system's central vorticity increases outside the standard development cycle, often influenced by nearby systems or localized atmospheric conditions that promote brief intensification (Section 3.3.1).

Figure 4.21 shows the track densities across all regions and seasons. A noticeable track density maximum is present near Uruguay and South Brazil, over the Brazil-Malvinas confluence (Gordon, 1989). The confluence region presents low-level baroclinicity, which can be transferred upwards in the atmosphere (Sanders and Gyakum, 1980; Vera et al., 2002, e.g.,). Systems passing over the confluence might experience brief intensification due to favorable conditions but not achieve maturity. This could also be important for systems with genesis in SE-BR, which are often weaker (Sinclair, 1995; Hoskins and Hodges, 2005). Furthermore, the track density maximum near 40°E and 55°S indicates that upper-level jet support (Swart et al., 2015, e.g.,) and a baroclinic environment (Hoskins and Hodges, 2005, e.g.,) could similarly drive marginal intensification, leading to a residual classification.

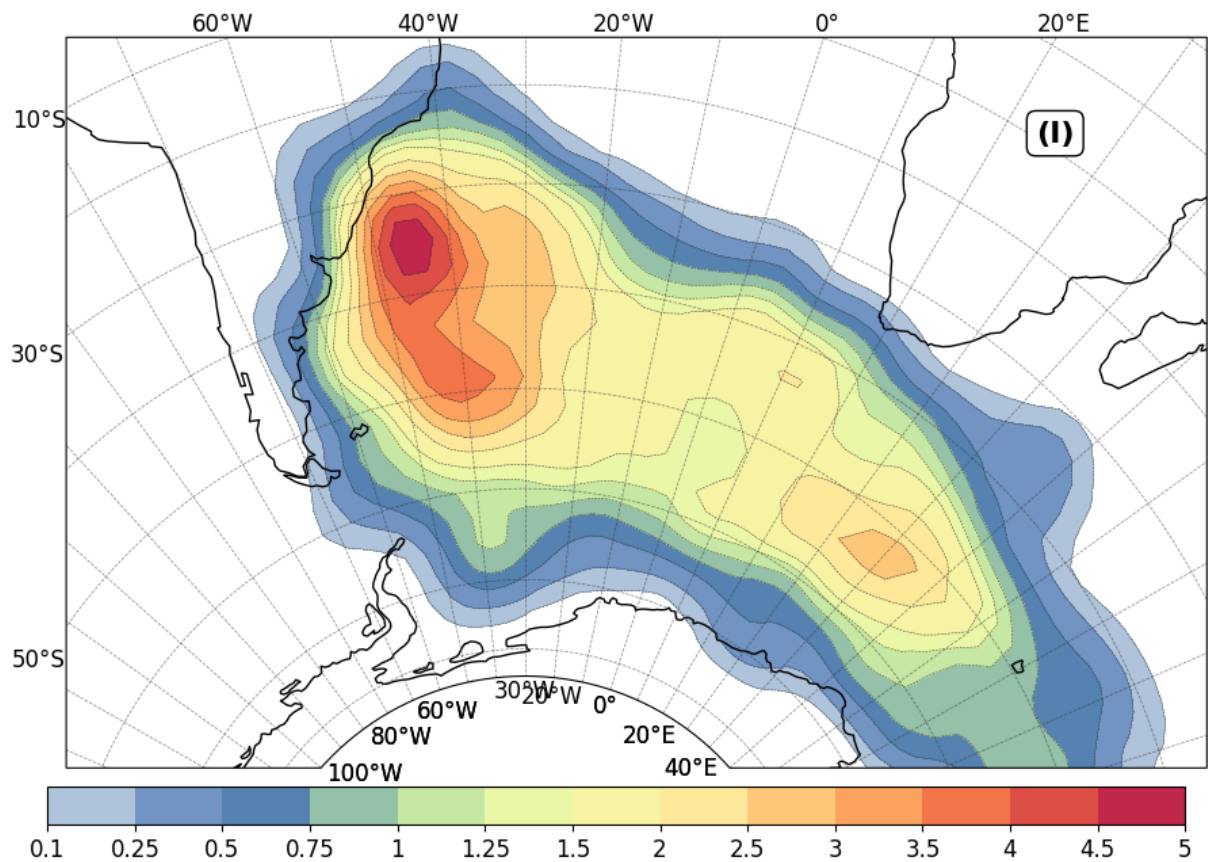


Figure 4.21: Cyclone track density during the residual phase for all systems with genesis in the ARG, LA-PLATA and SE-BR regions. The unit is cyclones per 10^6 km^2 per month.

4.3 Summary and Concluding Remarks

This study introduces CycloPhaser, a novel, open-source Python package for automated cyclone life cycle detection, available on the PyPI repository. Its low memory footprint, flexibility, and rapid deployment capabilities make it a valuable asset for climatological studies or even operational forecasts. The TRACK program identified a total of 7,931 systems from 1979 to 2020 for the cyclogenesis regions near South America. These results were narrowed down to life cycle configurations that accounted for at least 1% of the overall life cycle types count and presented at least one mature phase. These configurations represented approximately 95% of the total systems, amounting to 7,531 systems in total. The most common cyclone type followed a four-phase configuration: incipient, intensification, mature, and decay, accounting for about 60% of the analyzed systems. The results from the CycloPhaser program align well with previous studies regarding cyclone behavior in the South Atlantic region, confirming known cyclogenesis regions and providing statistical insights into cyclone lifetimes and paths. The CycloPhaser program calculated an average cyclone lifetime of approximately 97.6 and 91.1 hours (4 and 3.7 days) for austral summer (DJF) and winter (JJA), respectively, and an average displacement of 4,658 and 4,777 km for DJF and JJA. The mean displacement speed ranged from 14 to 15 ms^{-1} from DJF to JJA, while the mean vorticity ranged from 4 to $4.5 - 10^{-5}s^{-1}$. These findings largely corroborate those of previous studies for the regions and indicate a broad range of cyclone behaviors (Simmonds and Murray, 1999; Hoskins and Hodges, 2005; Mendes et al., 2010; Reboita et al., 2010; Gramcianinov et al., 2019, 2020; Crespo et al., 2023).

The analysis of spatial distributions revealed distinct patterns across various phases of the cyclone life cycle:

- **Incipient Phase:** The overall pattern matches the genesis regions described in the literature.
- **Intensification Phase:** The seasonal differences in track densities are mostly related to seasonal differences in genesis. Two maxima are present in both seasons: one mostly associated with ARG and the other with either LA-PLATA or SE-BR. However, other patterns include ARG systems being more eastward-oriented during JJA than DJF and reaching further east during DJF, while LA-PLATA systems tend to reach further southeast during JJA. Overall, the tracks are more displaced northward

during JJA than DJF.

- **Mature Phase:** The maximum track densities are southeast of the intensification centers during DJF and east/southeast during JJA. During JJA, cyclones from the ARG region mature close to the intensification. There is a higher positioning of cyclones close to Uruguay and Southern/Southeastern Brazil during DJF than JJA.
- **Decay Phase:** The track density regions elongate southeastward compared to the mature phase, with a maximum density east of the Weddell Sea, mainly related to systems from ARG. Systems with an early decay phase appear as density centers in LA-PLATA. During DJF, there are more tracks positioned near Uruguay and South/Southeast Brazil than JJA.
- **Second Intensification Phase:** There is a high concentration of tracks south of South Africa, which might be linked to secondary cyclogenesis processes (Mailier et al., 2006; Shapiro et al., 1997; Ford et al., 1990; Rivals et al., 1998).
- **Second Mature Phase:** This phase generally occurs southeastward of the second intensification phase.
- **Second Decay Phase:** This phase occurs bordering Antarctica, predominantly east of 40°E.

Figure 4.22 provides an illustrative representation of the life cycle of systems with genesis in the South American cyclogenesis regions. This figure highlights the systems' path through their lifecycle, showing that after genesis, the systems follow the usual storm tracks in the South Atlantic or, in the case of systems with genesis in ARG and LA-PLATA, the subtropical storm path branch. Although systems from ARG and SE-BR tend to have their genesis and intensification over the ocean, LA-PLATA systems tend to start intensifying close to the continent, which can impact coastal communities (de Souza and da Silva, 2021). Moreover, systems from SE-BR and LA-PLATA have their mature phases — where they are most intense and, therefore, transfer more momentum from the atmosphere to the ocean — near oceanic regions close to South and Southeast Brazil. These regions host large urban centers and significant economic activities, such as oil drilling.

The results presented here contribute significantly to the climatology of South Atlantic cyclones. CycloPhaser's detailed analysis of cyclone life cycle types, particularly focusing

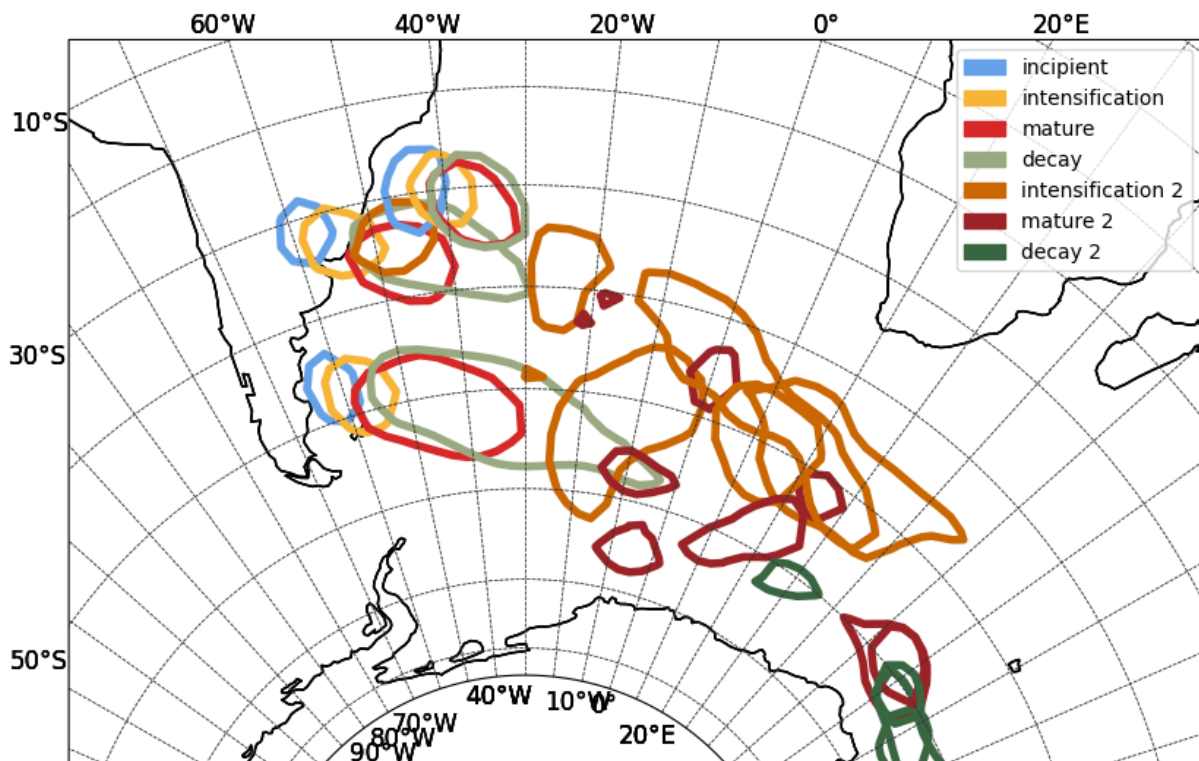


Figure 4.22: Track densities normalized for each region, using yearly values for all phases. For computing the track densities for the secondary development phases, only systems that display a complete secondary development cycle were used. Contours representing normalized track densities above 0.8 were plotted for each region individually.

on configurations accounting for significant proportions of cyclone activity, enhances our understanding of the spatial distribution of cyclone phases. This analysis reaffirms the common four-phase configuration (incipient, intensification, mature, and decay) and sheds light on variations in cyclone development cycles, contributing to a better understanding of how different regions within the South Atlantic influence the formation and evolution of distinct cyclone types. These insights are valuable for improving weather forecasting and developing effective mitigation strategies in the region.

Despite the valuable contributions of the CycloPhaser program, it is important to acknowledge the study's limitations. The analysis at a single atmospheric level offers a concentrated but partial view of the cyclone life cycle. Consequently, our conclusions about cyclone characteristics throughout their life cycle predominantly reflect the processes observable at the 850 hPa level. This methodological choice inherently limits our ability to fully explore the cyclones' vertical development and the complex interactions occurring at different atmospheric altitudes. Future research could benefit from incorporating a multi-level approach, providing a more holistic understanding of cyclone dynamics across the troposphere.

One of the unique contributions of this research is the assessment of cyclone life cycle stages along their storm tracks, a perspective not commonly explored in existing cyclone track climatologies. This first application has highlighted the complexity of cyclone systems and opened several avenues for future research. The approach presented here allows for the analysis of distinct dynamical mechanisms linked to the development of cyclonic systems at different stages of their life cycle. Investigating cyclonic life cycles in climate projections might be particularly relevant for coastal management in South America, posing questions such as: Will future cyclones intensify and mature closer to or further from coastal regions? Will these phases last longer? Furthermore, using the method presented here, future studies can delve deeper into the primary processes associated with each development stage in cyclone life cycles, including the secondary development stages reported herein, and determine whether some of these cases represent secondary genesis.

Chapter 5

Southwestern Atlantic Cyclones Energetics

The current chapter delves into the energetics of cyclones in the Southwestern Atlantic. The Lorenz Energy Cycle (LEC) was computed for all 7,531 systems with genesis in the ARG, LA-PLATA and SE-BR regions, as described in Chapter 2.14. This is the first time such large dataset is generated and analysed for the South Atlantic region, providing a comprehensive view of the energetics of all systems with genesis near South America.

CONTINUE

1. **Descriptive Statistics** - Compute summary statistics (mean, median, standard deviation, skewness, and kurtosis) for each component of the Lorenz Energetics. - Create histograms and boxplots to visualize the distribution of these components.
2. **Comparative Analysis** - Seasonal Variations: Analyze how the Lorenz Energetics vary across different seasons. Use ANOVA or Kruskal-Wallis tests to determine if there are significant differences between seasons. - Geographical Differences: Assess the spatial variability of the energetics. You can use spatial clustering methods or geostatistical analysis to identify patterns.
3. **Trend Analysis** - Conduct time-series analysis to identify any long-term trends in the energetics components over the study period. - Use techniques like Mann-Kendall trend test or linear regression to assess the presence of trends.
4. **Correlation Analysis** - Examine the relationships between different components of the Lorenz Energetics (e.g., Ca x Ce, Residuals x Generation terms). - Use Pearson or Spearman correlation coefficients to quantify the strength and direction of these relationships.
5. **Principal Component Analysis (PCA)** - Perform PCA to reduce the dimensionality of the Lorenz Energetics data and identify the main modes of variability. - Interpret

the principal components to understand the dominant patterns in the energetics data.

6. Cluster Analysis - Apply clustering techniques like K-means or hierarchical clustering to group cyclones based on their energetics profiles. - Analyze the characteristics of each cluster to identify distinct types of cyclones in terms of their energetics.

7. Extreme Value Analysis - Focus on the tails of the distribution to study extreme events. - Use generalized extreme value (GEV) distribution or peaks-over-threshold (POT) methods to model and analyze the extreme values of the energetics components.

8. Hypothesis Testing - Formulate and test hypotheses regarding the differences in Lorenz Energetics between different cyclone categories (e.g., intense vs. weak cyclones, coastal vs. open ocean cyclones). - Use t-tests, Mann-Whitney U tests, or chi-square tests depending on the data distribution and sample size.

9. Multivariate Regression Analysis - Build regression models to predict the Lorenz Energetics components based on various meteorological and oceanographic predictors. - Evaluate the model performance using metrics like R-squared, RMSE, and AIC.

5.1 LEC Climatology

5.1.1 Descriptive Statistics: Complete Life Cycle

This section provides exploratory statistics for each term of the LEC, covering the systems' complete life cycle. The aim is to offer a comprehensive view of the systems' energetics while identifying the main differences among the terms. Table 5.1 contains exploratory statistical metrics for these terms. Figure 5.1 presents the boxplots for all LEC components, where each panel depicts a distinct group of terms: (A) energy, (B) conversion, (C) boundary, (D) generation/dissipation terms, and (E) budgets. Figures 5.2, 5.3, 5.4, 5.5, and 5.6 display these groups of terms' density distributions, respectively.

For the energy terms, the values for K_Z are an order of magnitude higher than the others for all metrics analyzed (Table 5.1). Despite the high standard deviation (std) and quantile (Q) values indicating substantial variability, this can be attributed to the presence of numerous outliers (Figure 5.1a). Most values for K_Z peak between 15 and 17 $\times 10^5 J m^{-2}$ (Figure 5.2c). In contrast, A_Z presents relatively moderate mean and median values, with a right-skewed distribution and significant spread (Figure 5.2a). The notable outliers (Figure 5.1a) suggest periods of unusually high energy values.

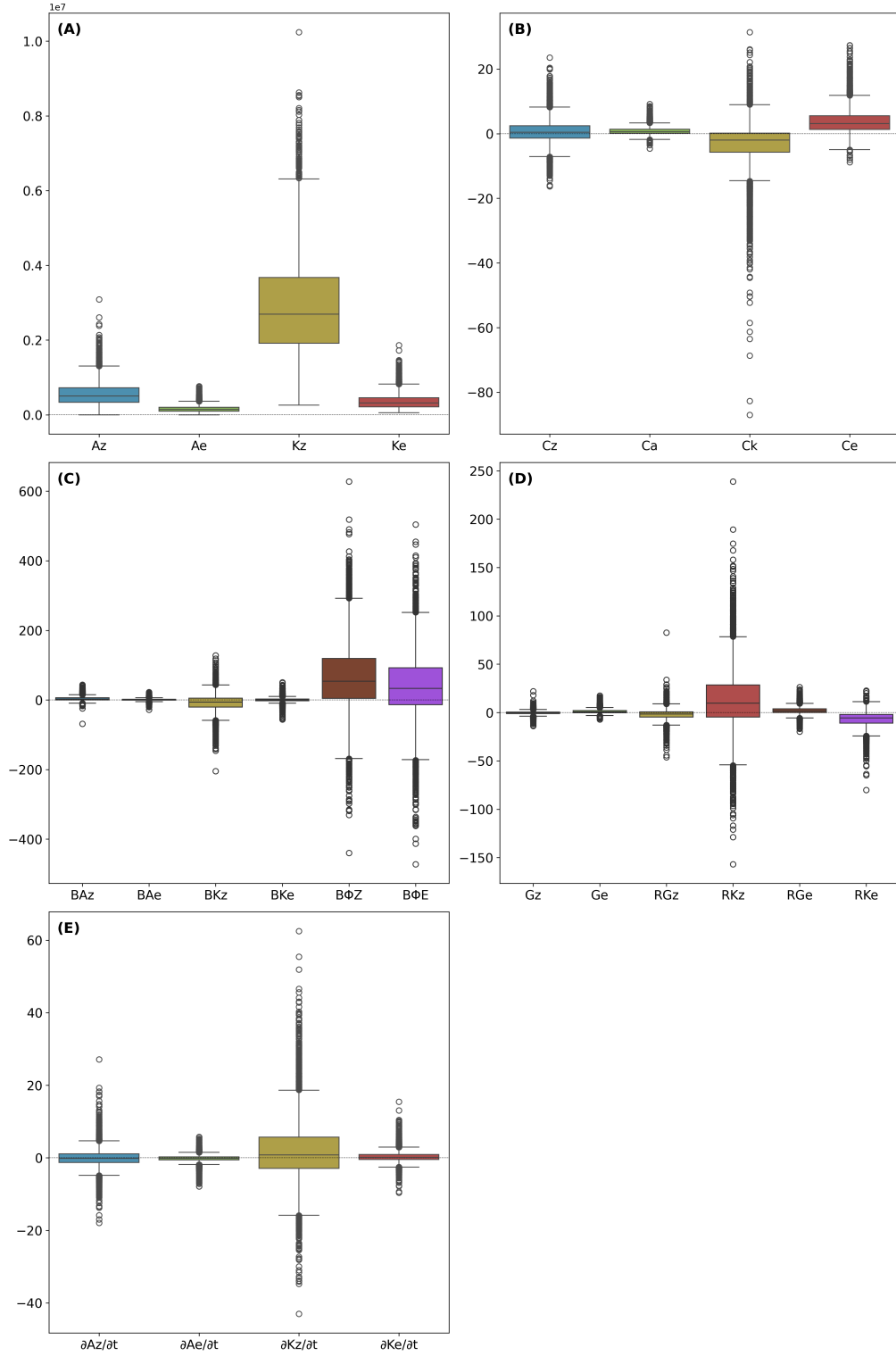


Figure 5.1: Box plots of each group of energetic terms, for the systems complete lifecycle. Each subplot represents a different group of terms: (A) Energy Terms, (B) Conversion Terms, (C) Boundary Terms, (D) Generation/Dissipation Terms, (E) Budgets. The box plots display the distribution of values for each term within the specified group, with the horizontal line indicating the median, the box representing the interquartile range (IQR), and the whiskers extending to 1.5 times the IQR. Outliers are shown as individual points.

Overall, the eddy energy terms (A_E and K_E) exhibit less variability and fewer outliers compared to the zonal energy terms (A_Z and K_Z) (Figure 5.1a). They also have smaller mean and median values (Table 5.1). Although both eddy energy terms peak close to each other, the distribution of A_E is more concentrated around the median (Figure 5.2b), with a narrower interquartile range (IQR) and lower standard deviation, suggesting it is more stable and consistent over time. In contrast, K_E presents a more right-skewed distribution than A_E (Figure 5.2d).

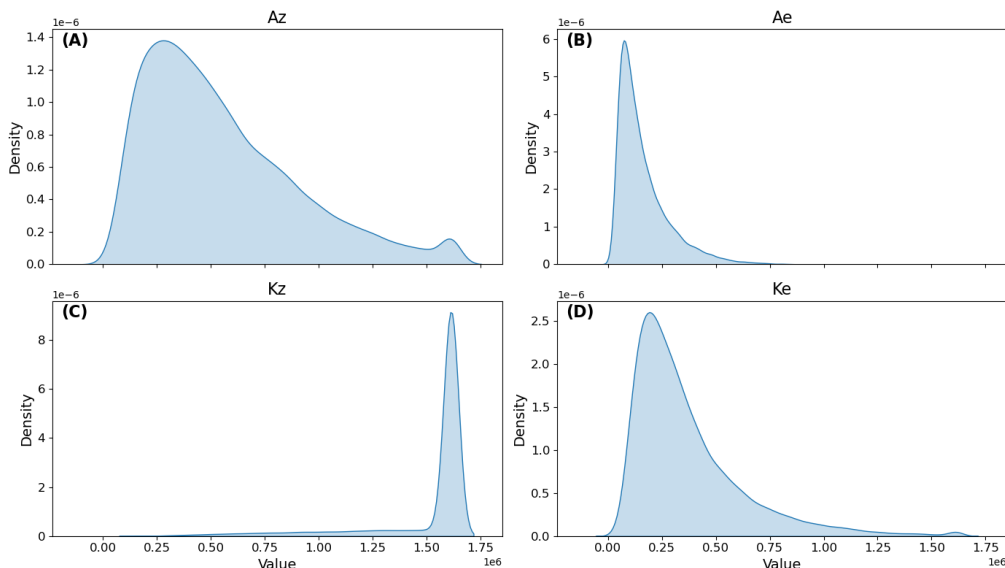


Figure 5.2: Density plots for energy terms A_Z (A), A_E (B), K_Z (C), and K_E (D). Each subplot represents the distribution of values for the specified energy term, showing the density across different value ranges.

While the mean values of A_E and K_E are generally in agreement with previous studies, the values of K_Z and A_Z differ significantly (Michaelides et al., 1999; Veiga et al., 2008; Dias Pinto and Rocha, 2011; Pezza et al., 2014, e.g.). Li et al. (2007) and Veiga et al. (2013), analyzing global LEC values, found mean K_Z values for the Southern Hemisphere of approximately 10 and $15.8 \times 10^5 J m^{-2}$ and mean A_Z values of approximately 40 and $16 \times 10^5 J m^{-2}$, respectively. Analyzing the LEC of extratropical cyclones primarily in the Northern Hemisphere, Smith (1980) found mean K_Z and A_Z values of 15 and $25 \times 10^5 J m^{-2}$, respectively. Meanwhile, Black and Pezza (2013), for explosive cyclogenesis in the Northwest Pacific region, found mean A_Z and K_Z values of approximately 30 and $48 \times 10^5 J m^{-2}$, respectively. Here, K_Z and A_Z presented mean values of 28.55 and $5.55 \times 10^5 J m^{-2}$, respectively.

The scarcity of results for a comprehensive set of systems hinders drawing decisive

Table 5.1 - Summary Statistics of Lorenz Energetics Components: mean, median, standard deviation (std), 20th percentile (Q20), 80th percentile (Q80), interquartile range (IQR), and range. The IQR measures the range within which the central 50% of the values fall, while the range is computed as the difference between the maximum and minimum values. The units for the energy terms (A_Z , A_E , K_Z , and K_E) are 10^5 J m^{-2} and W m^{-2} for the remaining terms.

Term	Mean	Median	Std	Q20	Q80	IQR	Range
Az	5.55	4.68	3.71	2.41	8.30	5.89	36.46
Ae	1.62	1.24	1.20	0.69	2.37	1.68	11.07
Kz	28.55	26.19	15.10	15.52	40.16	24.64	114.55
Ke	3.70	2.95	2.62	1.73	5.22	3.49	24.81
Cz	0.52	0.38	4.85	-2.69	3.72	6.41	86.70
Ca	0.93	0.46	1.57	-0.06	1.79	1.84	19.78
Ck	-3.56	-1.63	9.51	-7.41	1.11	8.52	206.43
Ce	3.84	2.47	4.92	0.33	6.97	6.64	54.74
BAz	3.54	2.03	7.67	-1.35	8.23	9.57	175.05
BAe	0.58	0.16	4.40	-1.62	2.75	4.37	75.72
BKz	-7.93	-5.53	31.75	-29.51	12.06	41.57	445.63
BKe	0.47	0.08	8.59	-3.67	4.40	8.07	146.87
BΦZ	63.87	49.25	128.05	-24.60	156.65	181.25	1419.08
BΦE	39.66	31.19	126.50	-46.44	132.10	178.54	1353.99
Gz	-0.31	-0.17	2.66	-1.82	1.14	2.96	68.74
Ge	1.17	0.56	3.14	-0.47	2.79	3.26	58.39
$\frac{\partial A_Z}{\partial t}$	-0.07	-0.14	4.46	-2.66	2.31	4.97	106.39
$\frac{\partial A_E}{\partial t}$	-0.23	-0.10	1.92	-1.14	0.74	1.88	48.19
$\frac{\partial K_Z}{\partial t}$	1.59	0.75	13.38	-7.13	10.40	17.53	251.24
$\frac{\partial K_E}{\partial t}$	0.28	0.12	3.18	-1.53	2.09	3.62	61.50
RGz	-2.17	-1.00	7.60	-6.69	2.31	9.01	220.06
RKz	12.56	8.69	40.49	-13.89	40.08	53.96	561.24
RGe	2.10	1.20	5.15	-0.84	5.28	6.12	97.25
RKe	-7.59	-4.63	10.62	-13.68	-0.45	13.23	138.42

conclusions about the behavior of the A_Z and A_E terms in cyclonic occurrences, while individual cases offer high variability, as indicated by case studies (Brennan and Vincent, 1980; Dias Pinto and Rocha, 2011; Pezza et al., 2014, e.g.,) and the higher variability in the data (Table 5.1). However, several observations can be made: 1) When compared to global energetics, cyclonic systems present higher K_Z values. This is expected because K_Z involves a zonal average of the wind components (Equation 2.34), and global averages would yield smaller values than those for limited areas closer to the cyclonic center, often associated with high-level jets; 2) Limited areas provide smaller A_Z values than hemispheric averages, due to the reduced meridional temperature and static stability gradients (Equation 2.32). These effects are even more evident in the current study, as the computational domain following the system focuses on the environmental dynamics surrounding it, thus capturing overall higher wind speeds through the atmosphere and smaller meridional temperature gradients. A similar effect is noted in Michaelides et al. (1999); 3) Furthermore, the literature shows that the magnitude and sign of the conversion, boundary, generation, and dissipation terms exhibit high variability across different systems and development phases (Brennan and Vincent, 1980; Smith, 1980; Michaelides, 1987; Bulic, 2006; Dias Pinto and Rocha, 2011; Black and Pezza, 2013, e.g.,), complicating comparisons of the overall values presented here with individual cases.

For the conversion terms, while C_Z , C_A , and C_E are positive on average and in median values, C_K is negative (Table 5.1). For C_A and C_E , there is a relatively narrow spread around the median, with some significant outliers (Figure 5.1b). C_A , showing a distribution centered around zero with both negative and positive values (Figure 5.3b), indicates alternating periods of energy transfer in both directions, predominantly from A_Z to A_E . Meanwhile, C_E has a left-skewed distribution (Figure 5.3d) and higher Q20 and IQR values, suggesting a more consistent positive net conversion.

The C_K term exhibits a wide distribution peaking at negative values (Figure 5.3c), with a significant negative mean and median, indicating a dominant net conversion from K_Z to K_E . The large range and standard deviation, along with the presence of significant outliers, suggest substantial variability in this conversion process. Lastly, C_Z presents the most distinctive behavior, with values centered around zero but peaking at both positive and negative values (Figure 5.3a). However, the higher peak at positive values along with the positive mean and median values indicate a preference for conversion from A_Z to K_Z .

The overall values presented here indicate that, throughout the systems' complete lifecycle, K_E tends to receive energy from A_E and, in most cases, from K_Z as well, although there are instances where C_K tends to be positive. There is also a general tendency for A_Z to be converted to A_E , albeit with a lower magnitude. Meanwhile, although C_Z can be positive, negative, or neutral, the predominant tendency is for conversion from A_Z to K_Z .

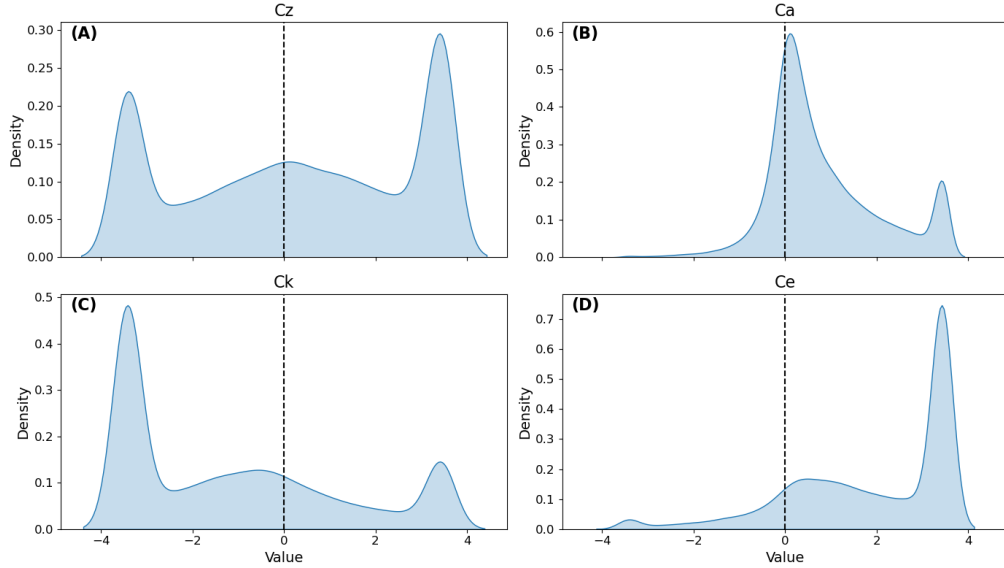


Figure 5.3: Density plots for conversion terms C_Z (A), C_A (B), C_K (C), and C_E (D). Each subplot represents the distribution of values for the specified energy term, showing the density across different value ranges.

There is a notable difference between the boundary flux terms (BA_Z , BA_E , BK_Z , BK_E) and the boundary pressure work terms ($B\Phi Z$ and $B\Phi E$) (Table 5.1). For the boundary flux terms, BA_Z presents the highest mean and median values, while BK_Z has the lowest. BA_E and BK_E have mean and median values closer to zero. The BA_Z term exhibits moderate variability, with a wide distribution around the median (Figure 5.4a) and few outliers (Figure 5.1c), a similar pattern to BK_E (Figure 5.4d). BA_E , in turn, displays the lowest variability among the boundary terms, with most values peaking near zero (Figure 5.4b). Meanwhile, BK_Z presents the most distinctive behavior, exhibiting high variability, with a wide distribution (Figure 5.4c) and numerous outliers. Its values range from the most negative to the most positive among the boundary terms, indicating an overall tendency for the exportation of zonal kinetic energy, supported by its negative mean and median values.

On the other hand, the boundary pressure work terms present similar behavior, with

very high mean and median values, especially $B\Phi Z$, and displaying two peaks: one on negative values (with a higher peak for the $B\Phi E$ term) and another, which displays higher densities, on positive values (Figure 5.4e and 5.4f). Both terms present low Q20 and high Q80 values, indicating that although they generally contribute to the appearance of energy in the K_Z and K_E terms, there are instances where they contribute negatively. For all metrics presented, they exhibit the highest values in magnitude across all terms. As Brennan and Vincent (1980) argued, these high values are associated with minor errors in the geopotential height field that can escalate. Although ERA5 presents the most modern reanalysis product offering homogeneous high-resolution data, systematic errors might be present, especially in regions with low data coverage, such as over the oceans and high altitudes (Hersbach et al., 2020). As most studies do not compute these terms as residuals and thus do not present the values (for instance, none of the studies presented in Section 2.4.3 do so), direct comparison of the values obtained here with the literature is hindered.

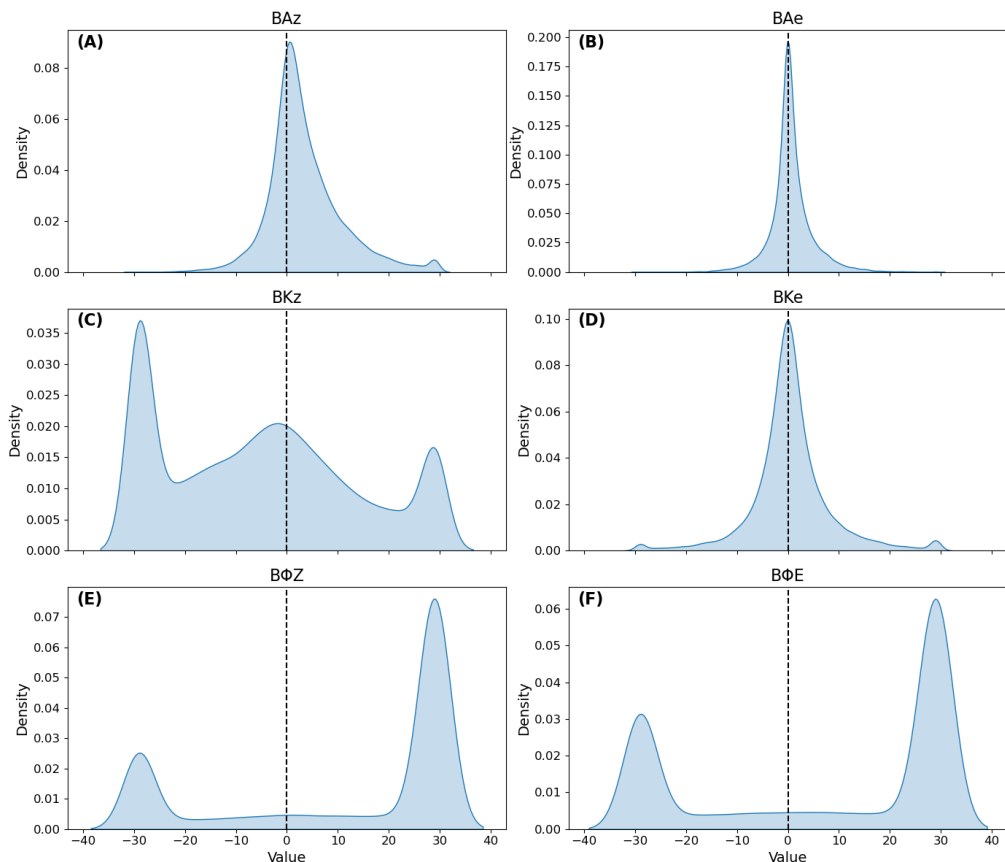


Figure 5.4: Density plots for boundary terms BA_Z (A), BA_E (B), BK_Z (C), BK_E (D), $B\Phi Z$ (E), and $B\Phi E$ (F). Each subplot represents the distribution of values for the specified energy term, showing the density across different value ranges.

Although the energy budgets are computed using residuals (which include the boundary pressure work terms), the generation terms are also analyzed as they serve both as an overall evaluation of the generation residual terms and because, in future sections, they will be used for understanding the systems' dynamics. Both G_Z and G_E present a similar distribution, displaying low variability (Figure 5.4), with most values peaking near zero and with minor peaks on both positive and negative values (Figures 5.5a and 5.5b). However, G_E presents a higher density of positive values, which is reflected in its higher mean and median values than G_Z and higher Q80 values (Table 5.1).

For the generation residual terms, both present three peaks - at positive, neutral, and negative values - but while RG_Z has the highest density around negative values, RG_E peaks at positive values (Figures 5.5c and 5.5e). This results in RG_E presenting positive mean and median values, despite a minor peak at negative values - which reflects in a negative Q20 value - indicating that its contribution to $\frac{\partial A_E}{\partial t}$ is mainly positive, with situations where this term contributes negatively. For RG_Z , the opposite is noted, with negative mean and median values, but a minor peak at positive values - reflected in a positive Q80 - indicating it mainly contributes negatively to $\frac{\partial A_Z}{\partial t}$, with situations where this term contributes positively.

Furthermore, while RK_Z presents higher positive mean and median values, it also shows high variability and numerous outliers (Figure 5.1d). It presents a distinctive density distribution, with two marked peaks, one for positive and the other for negative values (Figure 5.5d). This is reflected in its negative Q20 and positive Q80 values, with a high IQR. Therefore, although it mostly contributes positively to $\frac{\partial K_Z}{\partial t}$, there are also significant instances where it contributes negatively. RK_E , on the other hand, presents mean and median values peaking at negative values (Figure 5.5f). Therefore, it mostly contributes negatively to $\frac{\partial K_E}{\partial t}$, acting as a sink for K_E .

Among the budget terms, APE terms ($\frac{\partial A_Z}{\partial t}$ and $\frac{\partial A_E}{\partial t}$) present negative mean and median values, while the kinetic energy terms ($\frac{\partial K_Z}{\partial t}$ and $\frac{\partial K_E}{\partial t}$) are positive, although all of them exhibit negative Q20 values and positive Q80 values, indicating variability among the analyzed systems (Table 5.1). $\frac{\partial A_E}{\partial t}$ has the lowest variability, with the smallest IQR and range values, fewest outliers (Figure 5.1), and the highest peak density centered around zero (Figure 5.6b). This indicates that while in most cases there is an overall tendency for A_E to be neutral, there are also occurrences of positive and negative increments.

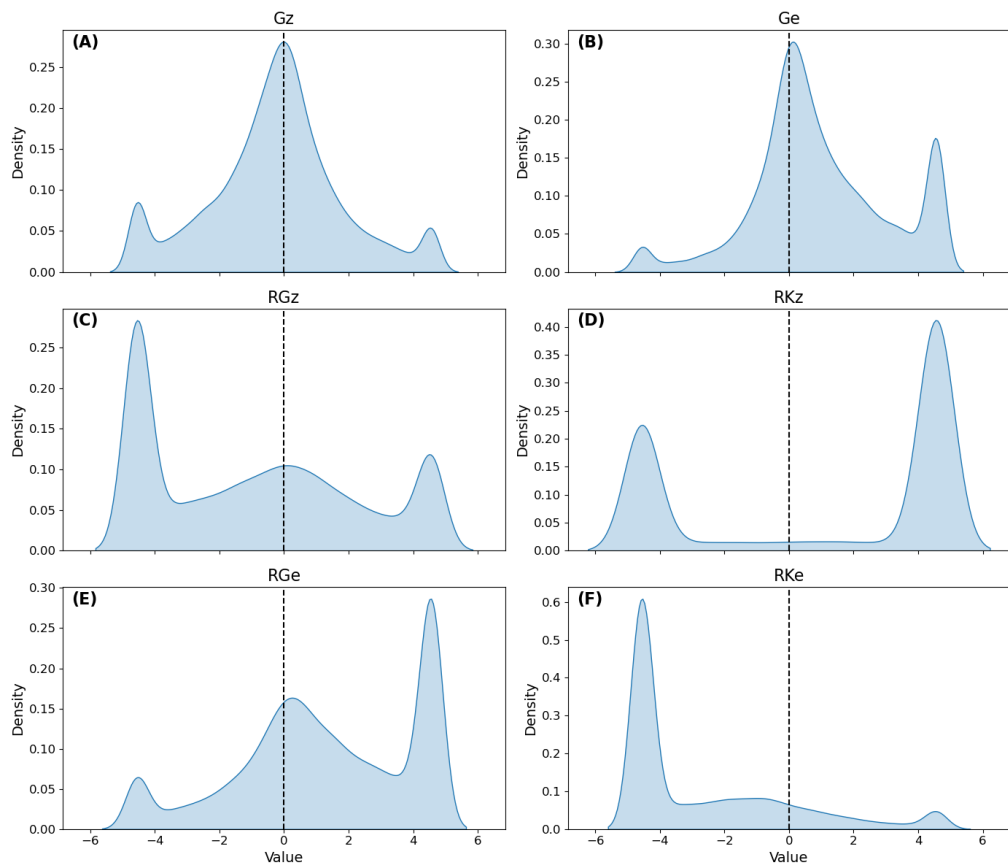


Figure 5.5: Density plots for generation terms G_Z (A) and G_E (B); and residual terms RG_Z (C), RK_Z (D), RG_E (E), and RK_E (F). Each subplot represents the distribution of values for the specified energy term, showing the density across different value ranges.

In contrast, $\frac{\partial A_Z}{\partial t}$ and $\frac{\partial K_E}{\partial t}$ display similar density distributions (Figure 5.6a and 5.6d), with peaks at negative, neutral, and positive values. $\frac{\partial A_Z}{\partial t}$ has a higher peak at negative values, indicating a tendency for A_Z to decrease, while $\frac{\partial K_E}{\partial t}$ peaks at positive values, reflecting a tendency for K_E to increase. However, both terms also show instances of neutrality and opposite trends.

Lastly, $\frac{\partial K_Z}{\partial t}$ exhibits a unique behavior with two prominent peaks at opposite extremes (Figure 5.6c). This term has the lowest Q20 and the highest Q80, IQR, and range values, indicating that K_Z tends to exhibit extreme changes — either significant increases or decreases — with a smaller tendency to remain neutral.

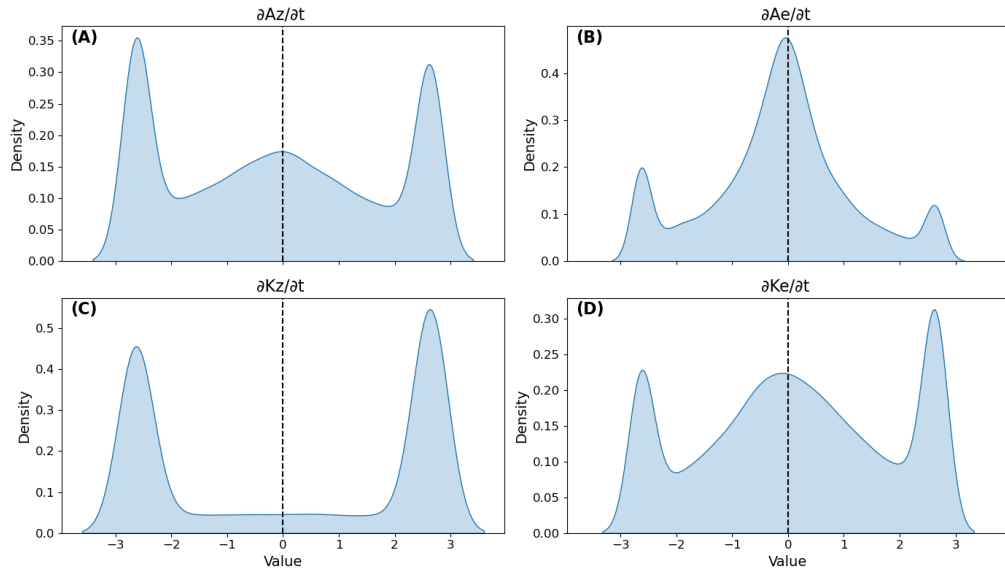


Figure 5.6: Density plots for budget terms $\frac{\partial A_Z}{\partial t}$ (A) and $\frac{\partial A_E}{\partial t}$ (B); $\frac{\partial K_Z}{\partial t}$ (C), and $\frac{\partial K_E}{\partial t}$ (D). Each subplot represents the distribution of values for the specified energy term, showing the density across different value ranges.

5.1.2 EOFs

The results presented in Section 5.1.1 demonstrate that the LEC terms exhibit high variability: each term spans a wide range of possible values, often with varying signs. Therefore, delineating an overall picture of the LEC for the analyzed systems is not a trivial task. To address this issue, an EOF analysis is used (Figure 5.7). It is important to note that the values represent anomalies rather than actual magnitudes of the energy cycle components. Additionally, G_Z and G_E terms are used for a more physically based interpretation, although the budgets were computed using their respective residuals. Since

the residual terms integrated these components, the presented budgets may not perfectly balance positive and negative energy fluxes due to the finite differences method used, which also incorporates numerical errors.

The first EOF (EOF1, Figure 5.7b) indicates an overall tendency for A_Z to decrease over time, primarily due to conversions to A_E ($C_A > 0$, Figure 2.24), which is an expected result. As discussed in Section 3.2.1, most cyclones in the dataset are extratropical, which have the final cause of diminishing Equator-Pole temperature gradients (Section 2.1.4), i.e., reducing A_Z . Additionally, there are losses of A_Z due to the G_Z term, indicating either anomalous heating in cool regions or anomalous cooling in warm regions caused by the eddy's meridional heat transport. Significant imports of A_Z are also observed through the BA_Z term. For the A_E term, there are only negligible increases over time. Despite influxes from C_A and diabatic processes ($G_E > 0$), most of its energy is converted to K_E ($C_E > 0$) due to enhanced zonal temperature gradients, while some of it is exported from the domain ($BA_E < 0$).

EOF1 indicates K_E increasing over time. This increase primarily stems from influxes from the residual term ($RK_E > 0$). Although the inclusion of numerical errors hinders the interpretation of the residual term, Section 5.1 indicates that $B\Phi_Z$ often presents large values, suggesting that this energy influx might be related to the generation of kinetic energy towards the cyclone's central low pressure. Meanwhile, part of K_Z energy is exported outside the domain ($BK_Z < 0$) or converted to K_E through the barotropic conversion term ($C_K < 0$). Only negligible amounts are converted into A_Z . Finally, K_E displays increases over time, driven mostly by conversion from A_E , but also with significant contributions from K_E . Notably, RK_E presents a similar magnitude to C_E , possibly indicating the dissipation of this energy. The importation of K_E is almost negligible.

Overall, in terms of the mechanisms related to the eddy growth, it can be seen that for EOF1 both the baroclinic and barotropic chains were active. This indicates that the eddy was gaining energy from both meridional temperature gradients as well as from horizontal wind shear. Moreover, diabatic processes were contributing to increasing the eddy APE, thus contributing to the moist baroclinic chain. Finally, the main sink for eddy energy was the residual term, possibly associated with dissipation by frictional forces.

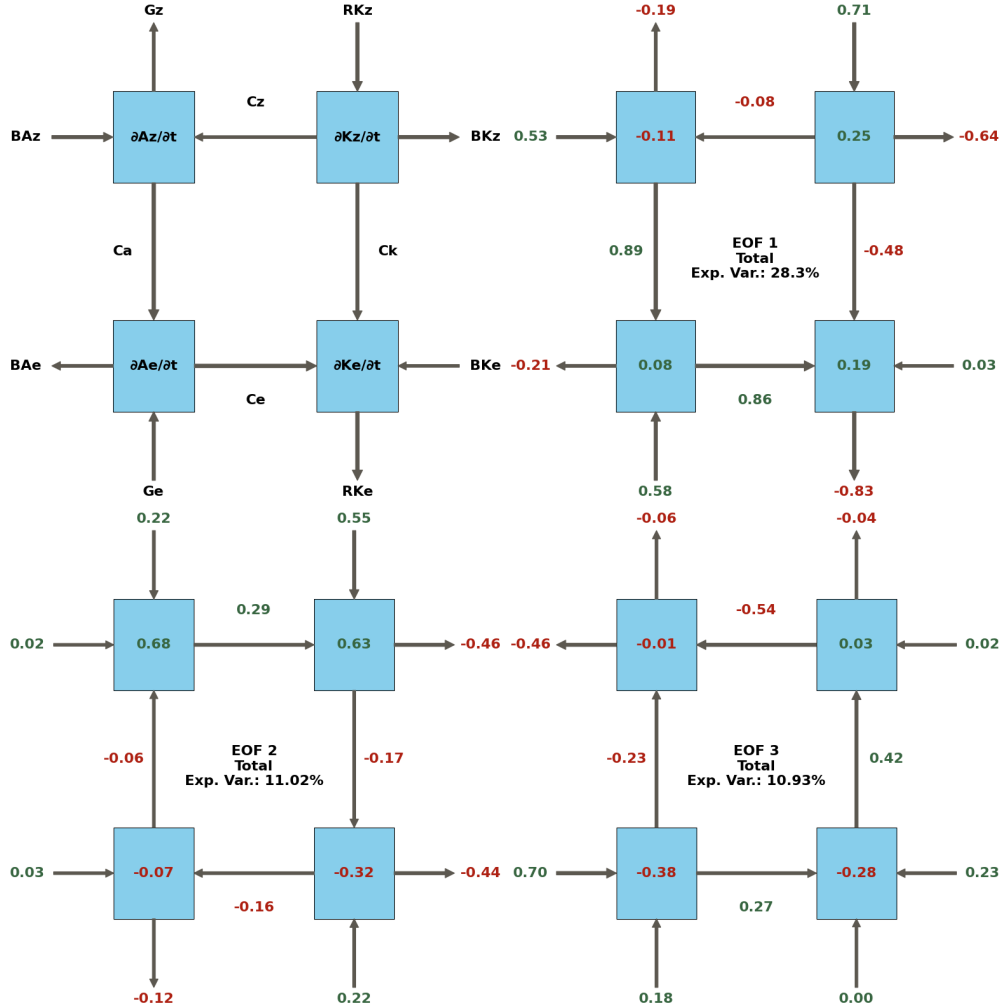


Figure 5.7: EOF Analysis of Lorenz Energy Cycle (LEC) Terms. The first diagram represents the LEC components, with each blue box indicating a specific energy component, with arrows showing the direction of energy flow. Meanwhile, the other diagrams represent the first three Empirical Orthogonal Functions (EOFs) of the energy cycle components, illustrating the anomalies in energy fluxes. The numbers adjacent to the arrows denote the magnitude and direction of the anomaly, with green indicating positive values and red indicating negative values.

Chapter 6

Modelagem numérica

6.1 Testes de sensibilidade: estudo de caso com Furacão Catarina

- Objetivos: 1) determinar qual conjunto de parametrizações de microfísica e cumulus apresentam os melhores resultados para o Catarina 2) determinar o impacto de diferentes escolhas na energética dos sistemas

6.1.1 Comparação da pressão mínima em superfície e posição do sistema

6.1.2 Precipitação acumulada

6.1.3 Ventos em superfície

6.1.4 Energética

6.2 Experimentos com perturbações no campo de SST

6.2.1 Interação oceano-atmosfera

6.2.2 Ciclo energético

Chapter 7

Conclusões

Conclusões do trabalho e/ou perspectivas

Bibliography

- Acevedo O. C., Pezzi L. P., Souza R. B., Anabor V., Degrazia G. A., Atmospheric boundary layer adjustment to the synoptic cycle at the Brazil-Malvinas Confluence, South Atlantic Ocean, *Journal of Geophysical Research: Atmospheres*, 2010, vol. 115
- American Meteorological Society, 2012 Cyclone <https://glossary.ametsoc.org/wiki/Cyclone>
- Aristotle A., Aristotle Metaphysics. vol. 1, Harvard University Press Cambridge, MA, 1933
- Azad R., Sorteberg A., The vorticity budgets of North Atlantic winter extratropical cyclone life cycles in MERRA reanalysis. Part I: Development phase, *Journal of the Atmospheric Sciences*, 2014a, vol. 71, p. 3109
- Azad R., Sorteberg A., The vorticity budgets of North Atlantic winter extratropical cyclone life cycles in MERRA reanalysis. Part II: Decaying phase, *Journal of the Atmospheric Sciences*, 2014b, vol. 71, p. 3129
- Bebenek E., Merlis T. M., Straub D. N., Influence of latitude and moisture effects on the barotropic instability of an idealized ITCZ, *Journal of the Atmospheric Sciences*, 2021, vol. 78, p. 2677
- Bengtsson L., Hodges K. I., Keenlyside N., Will extratropical storms intensify in a warmer climate?, *Journal of Climate*, 2009, vol. 22, p. 2276
- Bjerknes J., On the structure of moving cyclones, *Monthly Weather Review*, 1919, vol. 47, p. 95

Bjerknes J., Holmboe J., On the theory of cyclones, Journal of Atmospheric Sciences, 1944, vol. 1, p. 1

Bjerknes J., Solberg H., Life cycle of cyclones and the polar front theory of atmospheric circulation. Grondahl, 1922

Black M. T., Pezza A. B., A universal, broad-environment energy conversion signature of explosive cyclones, Geophysical Research Letters, 2013, vol. 40, p. 452

Bluestein H. B., Synoptic-dynamic Meteorology in Midlatitudes: Observations and theory of weather systems. vol. 2, Taylor & Francis, 1992

Booth J. F., Naud C. M., Jeyaratnam J., Extratropical cyclone precipitation life cycles: A satellite-based analysis, Geophysical Research Letters, 2018, vol. 45, p. 8647

Brennan F. E., Vincent D. G., Zonal and eddy components of the synoptic-scale energy budget during intensification of hurricane Carmen (1974), Monthly Weather Review, 1980, vol. 108, p. 954

Brown Jr J. A., A diagnostic study of tropospheric diabatic heating and the generation of available potential energy, Tellus, 1964, vol. 16, p. 371

Bulic I., Limited area energy budget during a life cycle of Genoa cyclone (18-21 November 1999), NUOVO CIMENTO-SOCIETA ITALIANA DI FISICA SEZIONE C, 2006, vol. 29, p. 167

Burpee R. W., The origin and structure of easterly waves in the lower troposphere of North Africa, Journal of the Atmospheric Sciences, 1972, vol. 29, p. 77

Cao X., Huang P., Chen G., Chen W., Modulation of western North Pacific tropical cyclone genesis by intraseasonal oscillation of the ITCZ: A statistical analysis, Advances in Atmospheric Sciences, 2012, vol. 29, p. 744

Cardoso A. A., da Rocha R. P., Crespo N. M., Synoptic Climatology of Subtropical Cyclone Impacts on Near-Surface Winds Over the South Atlantic Basin, Earth and Space Science, 2022, vol. 9, p. e2022EA002482

Cavicchia L., Dowdy A., Walsh K., Energetics and dynamics of subtropical australian east coast cyclones: Two contrasting cases, Monthly Weather Review, 2018, vol. 146, p. 1511

Chan J. C. L., Kepert J. D., eds, Global Perspectives on Tropical Cyclones: From Science to Mitigation. vol. 4 of World Scientific Series on Asia-Pacific Weather and Climate, World Scientific Singapore, 2010

Chang E. K., Lee S., Swanson K. L., Storm track dynamics, Journal of climate, 2002, vol. 15, p. 2163

Charney J. G., The dynamics of long waves in a baroclinic westerly current, Journal of the Atmospheric Sciences, 1947, vol. 4, p. 136

Charney J. G., Eliassen A., On the growth of the hurricane depression, Journal of the Atmospheric Sciences, 1964, vol. 21, p. 68

Craig G. C., Gray S. L., CISK or WISHE as the mechanism for tropical cyclone intensification, Journal of Atmospheric Sciences, 1996, vol. 53, p. 3528

Crespo N. M., da Rocha R. P., Sprenger M., Wernli H., A potential vorticity perspective on cyclogenesis over centre-eastern South America, International Journal of Climatology, 2021, vol. 41, p. 663

Crespo N. M., Reboita M. S., Gozzo L. F., de Jesus E. M., Torres-Alavez J. A., Lagos-Zúñiga M. Á., Torrez-Rodriguez L., Reale M., da Rocha R. P., Assessment of the RegCM4-CORDEX-CORE performance in simulating cyclones affecting the western coast of South America, Climate Dynamics, 2023, vol. 60, p. 2041

Da C., Shen B., Yan P., Ma D., Song J., The shallow water equation and the vorticity equation for a change in height of the topography, Plos one, 2017, vol. 12, p. e0178184

da Rocha R. P., Reboita M. S., Gozzo L. F., Dutra L. M. M., de Jesus E. M., Subtropical cyclones over the oceanic basins: a review, Annals of the New York Academy of Sciences, 2019, vol. 1436, p. 138

da Silva Dias P. L., da Silva Dias M. A. F., Seluchi M., de Assis Diniz F., O ciclone Catarina: Análise preliminar da estrutura, dinâmica e previsibilidade. In CONGRESSO BRASILEIRO DE METEOROLOGIA , 2004

Dacre H. F., Gray S. L., The spatial distribution and evolution characteristics of North Atlantic cyclones, Monthly Weather Review, 2009, vol. 137, p. 99

de Jesus E. M., da Rocha R. P., Crespo N. M., Reboita M. S., Gozzo L. F., Future climate trends of subtropical cyclones in the South Atlantic basin in an ensemble of global and regional projections, *Climate Dynamics*, 2022, vol. 58, p. 1221

de Souza D., da Silva R. R., Ocean-Land Atmosphere Model (OLAM) performance for major extreme meteorological events near the coastal region of southern Brazil, *Climate Research*, 2021, vol. 84, p. 1

de Souza D. C., Ramos da Silva R., Gomes da Silva P., Fetter Filho A. F. H., Mendez F. J., Werth D., A hybrid regional climate downscaling for the southern Brazil coastal region, *International Journal of Climatology*, 2022, vol. 42, p. 6753

Deveson A., Browning K., Hewson T., A classification of FASTEX cyclones using a height-attributable quasi-geostrophic vertical-motion diagnostic, *Quarterly Journal of the Royal Meteorological Society: A journal of the atmospheric sciences, applied meteorology and physical oceanography*, 2002, vol. 128, p. 93

Dias Pinto J. R., Reboita M. S., da Rocha R. P., Synoptic and dynamical analysis of subtropical cyclone Anita (2010) and its potential for tropical transition over the South Atlantic Ocean, *Journal of Geophysical Research: Atmospheres*, 2013, vol. 118, p. 10

Dias Pinto J. R., Rocha R. P., The energy cycle and structural evolution of cyclones over southeastern South America in three case studies, *Journal of Geophysical Research: Atmospheres*, 2011, vol. 116

Donald Ahrens C., Henson R., *Meteorology Today: An introduction to weather, climate and the environment*. Brooks/Cole, 2015

Duchon C. E., Lanczos filtering in one and two dimensions, *Journal of Applied Meteorology and Climatology*, 1979, vol. 18, p. 1016

Dutra L. M. M., da Rocha R. P., Lee R. W., Peres J. R. R., de Camargo R., Structure and evolution of subtropical cyclone Anita as evaluated by heat and vorticity budgets, *Quarterly Journal of the Royal Meteorological Society*, 2017, vol. 143, p. 1539

Dutton J. A., Johnson D. R., The theory of available potential energy and a variational approach to atmospheric energetics, *Advances in geophysics*, 1967, vol. 12, p. 333

- Eady E. T., Long waves and cyclone waves, Tellus, 1949, vol. 1, p. 33
- Edmon H. J., Vincent D. G., Large-scale atmospheric conditions during the intensification of Hurricane Carmen (1974) II. Diabatic heating rates and energy budgets, Monthly Weather Review, 1979, vol. 107, p. 295
- Emanuel K. A., An air-sea interaction theory for tropical cyclones. Part I: Steady-state maintenance, Journal of Atmospheric Sciences, 1986, vol. 43, p. 585
- Emanuel K. A., The dependence of hurricane intensity on climate, Nature, 1987, vol. 326, p. 483
- Emanuel K. A., Rotunno R., Polar lows as arctic hurricanes, Tellus A: Dynamic Meteorology and Oceanography, 1989, vol. 41, p. 1
- Evans J. L., Braun A., A climatology of subtropical cyclones in the South Atlantic, Journal of Climate, 2012, vol. 25, p. 7328
- Evans J. L., Hart R. E., Objective indicators of the life cycle evolution of extratropical transition for Atlantic tropical cyclones, Monthly Weather Review, 2003, vol. 131, p. 909
- Ferreira R. N., Schubert W. H., Barotropic aspects of ITCZ breakdown, Journal of the Atmospheric Sciences, 1997, vol. 54, p. 261
- Flaounas E., Kotroni V., Lagouvardos K., Flaounas I., CycloTRACK (v1. 0)—tracking winter extratropical cyclones based on relative vorticity: sensitivity to data filtering and other relevant parameters, Geoscientific Model Development, 2014, vol. 7, p. 1841
- Ford R., Ford R. P., Moore G. W. K., Moore G. W. K., Moore G. W. K., Secondary Cyclogenesis—Comparison of Observations and Theory, Monthly Weather Review, 1990
- Frank N. L., Atlantic tropical systems of 1969, Monthly Weather Review, 1970, vol. 98, p. 307
- Frank W. M., The structure and energetics of the tropical cyclone I. Storm structure, Monthly Weather Review, 1977a, vol. 105, p. 1119

Frank W. M., The structure and energetics of the tropical cyclone II. Dynamics and energetics, *Monthly Weather Review*, 1977b, vol. 105, p. 1136

Gall R., The effects of released latent heat in growing baroclinic waves, *Journal of the Atmospheric Sciences*, 1976, vol. 33, p. 1686

Gan M. A., Rao V. B., Surface cyclogenesis over south America, *Monthly Weather Review*, 1991, vol. 119, p. 1293

Gan M. A., Rao V. B., The influence of the Andes Cordillera on transient disturbances, *Monthly Weather Review*, 1994, vol. 122, p. 1141

Gibbs J. W., Fourier's series, *Nature*, 1898, vol. 59, p. 200

Gordon A. L., Brazil-malvinas confluence—1984, *Deep Sea Research Part A. Oceanographic Research Papers*, 1989, vol. 36, p. 359

Gozzo L., Da Rocha R., Gimeno L., Drumond A., Climatology and numerical case study of moisture sources associated with subtropical cyclogenesis over the southwestern Atlantic Ocean, *Journal of Geophysical Research: Atmospheres*, 2017, vol. 122, p. 5636

Gozzo L. F., da Rocha R. P., Reboita M. S., Sugahara S., Subtropical cyclones over the southwestern South Atlantic: Climatological aspects and case study, *Journal of Climate*, 2014, vol. 27, p. 8543

Gramcianinov C., Campos R., De Camargo R., Hodges K., Soares C. G., da Silva Dias P., Analysis of Atlantic extratropical storm tracks characteristics in 41 years of ERA5 and CFSR/CFSv2 databases, *Ocean Engineering*, 2020, vol. 216, p. 108

Gramcianinov C., Campos R., Soares C. G., de Camargo R., Extreme waves generated by cyclonic winds in the western portion of the South Atlantic Ocean, *Ocean Engineering*, 2020, vol. 213, p. 107745

Gramcianinov C., Hodges K., Camargo R. d., The properties and genesis environments of South Atlantic cyclones, *Climate Dynamics*, 2019, vol. 53, p. 4115

Gramcianinov C. B., Campos R. M., de Camargo R., Hodges K. I., Guedes Soares C., da Silva Dias P. L., Atlantic extratropical cyclone tracks in 41 years of ERA5 and CFSR/CFSv2 databases, *Mendeley Data*, 2020, vol. V4

Gramcianinov C. B., de Camargo R., Campos R. M., Guedes Soares C., da Silva Dias P. L., Impact of extratropical cyclone intensity and speed on the extreme wave trends in the Atlantic Ocean, *Climate dynamics*, 2023, vol. 60, p. 1447

Gray S. L., Dacre H. F., Classifying dynamical forcing mechanisms using a climatology of extratropical cyclones, *Quarterly Journal of the Royal Meteorological Society: A journal of the atmospheric sciences, applied meteorology and physical oceanography*, 2006, vol. 132, p. 1119

Gray W. M., Global view of the origin of tropical disturbances and storms, *Monthly Weather Review*, 1968, vol. 96, p. 669

Gray W. M., The formation of tropical cyclones, *Meteorology and atmospheric physics*, 1998, vol. 67, p. 37

Grise K. M., Son S.-W., Gyakum J. R., Intraseasonal and interannual variability in North American storm tracks and its relationship to equatorial Pacific variability, *Monthly Weather Review*, 2013, vol. 141, p. 3610

Gutowski W. J., Branscome L. E., Stewart D. A., Life cycles of moist baroclinic eddies, *Journal of the atmospheric sciences*, 1992, vol. 49, p. 306

Hadley G., VI. Concerning the cause of the general trade-winds, *Philosophical Transactions of the Royal Society of London*, 1735, vol. 39, p. 58

Hamming R. W., *Digital Filters*. Prentice Hall, 1989

Harris F. J., On the use of windows for harmonic analysis with the discrete Fourier transform, *Proceedings of the IEEE*, 1978, vol. 66, p. 51

Harrold T., Browning K., The polar low as a baroclinic disturbance, *Quarterly Journal of the Royal Meteorological Society*, 1969, vol. 95, p. 710

Hart R. E., A cyclone phase space derived from thermal wind and thermal asymmetry, *Monthly weather review*, 2003, vol. 131, p. 585

Held I. M., The macroturbulence of the troposphere, *Tellus A*, 1999, vol. 51, p. 59

Hersbach H., Bell B., Berrisford P., Hirahara S., Horányi A., Muñoz-Sabater J., Nicolas J., Peubey C., Radu R., Schepers D., et al., The ERA5 global reanalysis, Quarterly Journal of the Royal Meteorological Society, 2020, vol. 146, p. 1999

Hodges K., Feature tracking on the unit sphere, Monthly Weather Review, 1995, vol. 123, p. 3458

Hodges K. I., A general method for tracking analysis and its application to meteorological data, Monthly Weather Review, 1994, vol. 122, p. 2573

Holopainen E. O., Investigation of friction and diabatic processes in the atmosphere. vol. 29, na, 1964

Holton J. R., An introduction to dynamic meteorology. vol. 41, American Association of Physics Teachers, 1973, 752

Hoskins B. J., Theory of extratropical cyclones. Springer, 1990, 63

Hoskins B. J., Hodges K. I., New perspectives on the Northern Hemisphere winter storm tracks, Journal of the Atmospheric Sciences, 2002, vol. 59, p. 1041

Hoskins B. J., Hodges K. I., A new perspective on Southern Hemisphere storm tracks, Journal of Climate, 2005, vol. 18, p. 4108

Hoskins B. J., Valdes P. J., On the existence of storm-tracks, Journal of Atmospheric Sciences, 1990, vol. 47, p. 1854

Jensen C. E., Energy transformation and vertical flux processes over the northern hemisphere, Journal of Geophysical Research, 1961, vol. 66, p. 1145

Johnson D. R., The available potential energy of storms, Journal of Atmospheric Sciences, 1970, vol. 27, p. 727

Jorgensen D. P., Zipser E. J., LeMone M. A., Vertical motions in intense hurricanes, Journal of the atmospheric sciences, 1985, vol. 42, p. 839

Knutson T. R., McBride J. L., Chan J., Emanuel K., Holland G., Landsea C., Held I., Kossin J. P., Srivastava A., Sugi M., Tropical cyclones and climate change, Nature geoscience, 2010, vol. 3, p. 157

- Kuo H.-l., Dynamic instability of two-dimensional nondivergent flow in a barotropic atmosphere, *Journal of Atmospheric sciences*, 1949, vol. 6, p. 105
- Li L., Ingersoll A. P., Jiang X., Feldman D., Yung Y. L., Lorenz energy cycle of the global atmosphere based on reanalysis datasets, *Geophysical Research Letters*, 2007, vol. 34
- Lorenz E., The nature and theory of the general circulation of the atmosphere, World meteorological organization, 1967, vol. 161
- Lorenz E. N., Available Potential Energy and the Maintenance of the General Circulation, *Tellus*, 1955, vol. 7, p. 157
- McLennan N., , 1988 Technical report Marine Bombs Program: Phase II. Pacific Weather Centre
- McTaggart-Cowan R., Bosart L. F., Davis C. A., Atallah E. H., Gyakum J. R., Emanuel K. A., Analysis of hurricane Catarina (2004), *Monthly Weather Review*, 2006, vol. 134, p. 3029
- Mailier P., Mailier P. J., Stephenson D. B., Stephenson D. B., Ferro C. A. T., Ferro C. A. T., Hodges K. I., Hodges K. I., Serial Clustering of Extratropical Cyclones, *Monthly Weather Review*, 2006
- Maloney E. D., Hartmann D. L., The Madden–Julian oscillation, barotropic dynamics, and North Pacific tropical cyclone formation. Part I: Observations, *Journal of the atmospheric sciences*, 2001, vol. 58, p. 2545
- Margules M., Uber die Energie der Sturme, *Jahrb. kair-kon Zent*, 1903
- Marquet P., On the concept of exergy and available enthalpy: Application to atmospheric energetics, *Quarterly Journal of the Royal Meteorological Society*, 1991, vol. 117, p. 449
- Marquet P., The last paper”On the theory of storm”(Zur Sturmtheorie) published by Max Margules in 1906, arXiv preprint arXiv:1704.06128, 2017
- Marrafon V. H., Reboita M. S., da Rocha R. P., de Jesus E. M., Classificação dos tipos de ciclones sobre o Oceano Atlântico Sul em projeções com o RegCM4 E MCGs, *Revista Brasileira de Climatologia*, 2022, vol. 30, p. 1

Mendes D., Souza E. P., Marengo J. A., Mendes M. C., Climatology of extratropical cyclones over the South American–southern oceans sector, *Theoretical and applied climatology*, 2010, vol. 100, p. 239

Michaelides S. C., Limited area energetics of Genoa cyclogenesis, *Monthly Weather Review*, 1987, vol. 115, p. 13

Michaelides S. C., A spatial and temporal energetics analysis of a baroclinic disturbance in the Mediterranean, *Monthly weather review*, 1992, vol. 120, p. 1224

Michaelides S. C., Prezerakos N. G., Flocas H. A., Quasi-Lagrangian energetics of an intense Mediterranean cyclone, *Quarterly Journal of the Royal Meteorological Society*, 1999, vol. 125, p. 139

Mitra S. K., *Digital Signal Processing: A Computer-Based Approach*. McGraw-Hill, 2001

Molinari J., Knight D., Dickinson M., Vollaro D., Skubis S., Potential vorticity, easterly waves, and eastern Pacific tropical cyclogenesis, *Monthly weather review*, 1997, vol. 125, p. 2699

Molinari J., Vollaro D., Skubis S., Dickinson M., Origins and mechanisms of eastern Pacific tropical cyclogenesis: A case study, *Monthly Weather Review*, 2000, vol. 128, p. 125

Montgomery M. T., Persing J., Smith R. K., Putting to rest WISHE-ful misconceptions for tropical cyclone intensification, *Journal of Advances in Modeling Earth Systems*, 2015, vol. 7, p. 92

Montgomery M. T., Smith R. K., Paradigms for tropical cyclone intensification, *Australian Meteorological and Oceanographic Journal*, 2014, vol. 64, p. 37

Muench H. S., On the dynamics of the wintertime stratosphere circulation, *Journal of Atmospheric Sciences*, 1965, vol. 22, p. 349

Murray R. J., Simmonds I., A numerical scheme for tracking cyclone centres from digital data. Part II: Application to January and July general circulation model simulations, *Australian Meteorological Magazine*, 1991, vol. 39, p. 167

Nordeng T. E., Rasmussen E. A., A most beautiful polar low. A case study of a polar low development in the Bear Island region, *Tellus A*, 1992, vol. 44, p. 81

- Norquist D. C., Recker E. E., Reed R. J., The energetics of African wave disturbances as observed during phase III of GATE, *Monthly Weather Review*, 1977, vol. 105, p. 334
- Novak L., Tailleux R., On the local view of atmospheric available potential energy, *Journal of the Atmospheric Sciences*, 2018, vol. 75, p. 1891
- Okajima S., Nakamura H., Kaspi Y., Cyclonic and anticyclonic contributions to atmospheric energetics, *Scientific reports*, 2021, vol. 11, p. 13202
- Oort A. H., On estimates of the atmospheric energy cycle, *Monthly Weather Review*, 1964, vol. 92
- Ooyama K. V., Conceptual evolution of the theory and modeling of the tropical cyclone, *Journal of the Meteorological Society of Japan. Ser. II*, 1982, vol. 60, p. 369
- Oppenheim A. V., *Discrete-time signal processing*. Pearson Education India, 1999
- Oppenheim A. V., Schafer R. W., *Discrete-Time Signal Processing*. Prentice Hall, 2009
- Ozawa H., Shimokawa S., Thermodynamics of a tropical cyclone: Generation and dissipation of mechanical energy in a self-driven convection system, *Tellus A: Dynamic Meteorology and Oceanography*, 2015, vol. 67, p. 24216
- Palmén E. H., Newton C. W., Atmospheric circulation systems: their structure and physical interpretation. vol. 13, Academic press, 1969
- Pereira Filho A. J., Pezza A. B., Simmonds I., Lima R. S., Vianna M., New perspectives on the synoptic and mesoscale structure of Hurricane Catarina, *Atmospheric Research*, 2010, vol. 95, p. 157
- Petterssen S., Smebye S., On the development of extratropical cyclones, *Quarterly Journal of the Royal Meteorological Society*, 1971, vol. 97, p. 457
- Pezza A. B., Garde L. A., Veiga J. A. P., Simmonds I., Large scale features and energetics of the hybrid subtropical low ‘Duck’ over the Tasman Sea, *Climate dynamics*, 2014, vol. 42, p. 453
- Pezza A. B., Simmonds I., The first South Atlantic hurricane: Unprecedented blocking, low shear and climate change, *Geophysical Research Letters*, 2005, vol. 32

Pezza A. B., Simmonds I., Pereira Filho A. J., Climate perspective on the large-scale circulation associated with the transition of the first South Atlantic hurricane, International Journal of Climatology: A Journal of the Royal Meteorological Society, 2009, vol. 29, p. 1116

Pezza A. B., Veiga J. A. P., Simmonds I., Keay K., Mesquita M. d. S., Environmental energetics of an exceptional high-latitude storm, Atmospheric Science Letters, 2010, vol. 11, p. 39

Pinto J. G., Spangehl T., Ulbrich U., Speth P., Sensitivities of a cyclone detection and tracking algorithm: individual tracks and climatology, Meteorologische Zeitschrift, 2005, vol. 14, p. 823

Plumb R. A., A new look at the energy cycle, Journal of Atmospheric Sciences, 1983, vol. 40, p. 1669

Proakis J. G., Manolakis D. G., Digital Signal Processing: Principles, Algorithms, and Applications. Prentice Hall, 2006

Ramage C. S., Hurricane development, Journal of Atmospheric Sciences, 1959, vol. 16, p. 227

Rasmussen E., The polar low as an extratropical CISK disturbance, Quarterly Journal of the Royal Meteorological Society, 1979, vol. 105, p. 531

Rasmussen E., A case study of a polar low development over the Barents Sea, Tellus A, 1985, vol. 37, p. 407

Rasmussen E. A., A comparative study of tropical cyclones and polar lows. vol. 47, A. Deepak Publishing, 1989, 80

Reboita M., Crespo N., Dutra L., Silva B., Capucin B., da Rocha R., Iba: the first pure tropical cyclogenesis over the western South Atlantic Ocean, Journal of Geophysical Research: Atmospheres, 2021, vol. 126, p. e2020JD033431

Reboita M. S., Da Rocha R. P., Ambrizzi T., Sugahara S., South Atlantic Ocean cyclogenesis climatology simulated by regional climate model (RegCM3), Climate Dynamics, 2010, vol. 35, p. 1331

Reboita M. S., Da Rocha R. P., Oliveira D. M. d., Key features and adverse weather of the named subtropical cyclones over the Southwestern South Atlantic Ocean, *Atmosphere*, 2018, vol. 10, p. 6

Reboita M. S., Gan M. A., Rocha R. P. d., Ambrizzi T., Regimes de precipitação na América do Sul: uma revisão bibliográfica, *Revista brasileira de meteorologia*, 2010, vol. 25, p. 185

Reboita M. S., Gan M. A., Rocha R. P. d., Custódio I. S., Ciclones em superfície nas latitudes austrais: Parte I-revisão bibliográfica, *Revista Brasileira de Meteorologia*, 2017, vol. 32, p. 171

Reboita M. S., Gozzo L. F., Crespo N. M., Custodio M. d. S., Lucyrio V., de Jesus E. M., da Rocha R. P., From a Shapiro–Keyser extratropical cyclone to the subtropical cyclone Raoni: An unusual winter synoptic situation over the South Atlantic Ocean, *Quarterly Journal of the Royal Meteorological Society*, 2022, vol. 148, p. 2991

Reboita M. S., Oliveira D., Da Rocha R., Dutra L., Subtropical cyclone Anita's potential to tropical transition under warmer sea surface temperature scenarios, *Geophysical Research Letters*, 2019, vol. 46, p. 8484

Reed R. J., Norquist D. C., Recker E. E., The structure and properties of African wave disturbances as observed during phase III of GATE, *Monthly Weather Review*, 1977, vol. 105, p. 317

Reed R. J., Wolfe J. L., Nishimoto H., A spectral analysis of the energetics of the stratospheric sudden warming of early 1957, *Journal of the Atmospheric Sciences*, 1963, vol. 20, p. 256

Rennick M. A., The generation of African waves, *Journal of Atmospheric Sciences*, 1976, vol. 33, p. 1955

Riehl H., On the formation of typhoons, *Journal of the Atmospheric Sciences*, 1948, vol. 5, p. 247

Rivals H., Rivals H., Cammas J., Cammas J.-P., Renfrew I. A., Renfrew I. A., Secondary cyclogenesis: The initiation phase of a frontal wave observed over the eastern Atlantic, *Quarterly Journal of the Royal Meteorological Society*, 1998

Robertson F., Smith P., The impact of model moist processes on the energetics of extra-tropical cyclones, *Monthly Weather Review*, 1983, vol. 111, p. 723

Rudeva I., Gulev S. K., Climatology of cyclone size characteristics and their changes during the cyclone life cycle, *Monthly Weather Review*, 2007, vol. 135, p. 2568

Saltzman B., Fleisher A., Further statistics on the modes of release of available potential energy, *Journal of Geophysical Research*, 1961, vol. 66, p. 2271

Sanders F., Gyakum J. R., Synoptic-dynamic climatology of the “bomb”, *Monthly Weather Review*, 1980, vol. 108, p. 1589

Savitzky A., Golay M. J., Smoothing and differentiation of data by simplified least squares procedures., *Analytical chemistry*, 1964, vol. 36, p. 1627

Schemm S., Sprenger M., Wernli H., When during their life cycle are extratropical cyclones attended by fronts?, *Bulletin of the American Meteorological Society*, 2018, vol. 99, p. 149

Schneider T., The general circulation of the atmosphere, *Annu. Rev. Earth Planet. Sci.*, 2006, vol. 34, p. 655

Schultz D. M., Keyser D., Bosart L. F., The effect of large-scale flow on low-level frontal structure and evolution in midlatitude cyclones, *Monthly weather review*, 1998, vol. 126, p. 1767

Shapiro M. A., Doyle J., Zou X., Jorgensen D. P., Jorgensen D. P., Jorgensen D. P., Extratropical Secondary Cyclones: Simulations and Observations,, null, 1997

Shapiro M. A., Keyser D., Fronts, jet streams and the tropopause. Springer, 1990

Shea D. J., Gray W. M., The hurricane’s inner core region. I. Symmetric and asymmetric structure, *Journal of the Atmospheric Sciences*, 1973, vol. 30, p. 1544

Silva Dias P. L., Gan M., Beven J. L., Pezza A., Holland G., Pereira A., McTaggart-Cowan R., Diniz F. d. A., Seluchi M., Braga H. J., The Catarina Phenomenon. In *Proceedings of the Sixth International Workshop on Tropical Cyclones*, São Paulo, Brazil, 2004

- Simmonds I., Size changes over the life of sea level cyclones in the NCEP reanalysis, *Monthly Weather Review*, 2000, vol. 128, p. 4118
- Simmonds I., Keay K., Mean Southern Hemisphere extratropical cyclone behavior in the 40-year NCEP–NCAR reanalysis, *Journal of Climate*, 2000, vol. 13, p. 873
- Simmonds I., Murray R. J., Southern extratropical cyclone behavior in ECMWF analyses during the FROST special observing periods, *Weather and forecasting*, 1999, vol. 14, p. 878
- Simpson R. H., Evolution of the Kona storm a subtropical cyclone, *Journal of Atmospheric Sciences*, 1952, vol. 9, p. 24
- Sinclair M. R., An objective cyclone climatology for the Southern Hemisphere, *Monthly Weather Review*, 1994, vol. 122, p. 2239
- Sinclair M. R., A climatology of cyclogenesis for the Southern Hemisphere, *Monthly Weather Review*, 1995, vol. 123, p. 1601
- Smith P. J., On the contribution of a limited region to the global energy budget, *Tellus*, 1969, vol. 21, p. 202
- Smith P. J., The energetics of extratropical cyclones, *Reviews of Geophysics*, 1980, vol. 18, p. 378
- Smith P. J., Vincent D. G., Edmond Jr H. J., The time dependence of reference pressure in limited region available potential energy budget equations, *Tellus*, 1977, vol. 29, p. 476
- Smith S. W., *The Scientist and Engineer's Guide to Digital Signal Processing*. California Technical Publishing, 1997
- Spiridonov V., Ćurić M., *Fundamentals of meteorology*. Springer, 2021
- Starr V. P., Note concerning the nature of the large-scale eddies in the atmosphere, *Tellus*, 1953, vol. 5, p. 494
- Starr V. P., Further statistics concerning the general circulation, *Tellus*, 1959, vol. 11, p. 481

Steele C., Dorling S., von Glasow R., Bacon J., Modelling sea-breeze climatologies and interactions on coasts in the southern North Sea: implications for offshore wind energy, *Quarterly Journal of the Royal Meteorological Society*, 2015, vol. 141, p. 1821

Stoll P. J., Spengler T., Terpstra A., Graversen R. G., Polar lows–moist-baroclinic cyclones developing in four different vertical wind shear environments, *Weather and Climate Dynamics*, 2021, vol. 2, p. 19

Stull R. B., Practical meteorology: an algebra-based survey of atmospheric science. University of British Columbia, 2015

Sutcliffe R., A contribution to the problem of development, *Quarterly Journal of the Royal Meteorological Society*, 1947, vol. 73, p. 370

Swart N. C., Fyfe J. C., Gillett N., Marshall G. J., Comparing trends in the southern annular mode and surface westerly jet, *Journal of Climate*, 2015, vol. 28, p. 8840

Terry J. P., Tropical cyclones: climatology and impacts in the South Pacific. Springer Science & Business Media, 2007

Tibaldi S., Buzzi A., Malguzzi P., Orographically induced cyclogenesis: Analysis of numerical experiments, *Monthly Weather Review*, 1980, vol. 108, p. 1302

Trenberth K. E., On the interpretation of the diagnostic quasi-geostrophic omega equation, *Mon. Wea. Rev.*, 1978, vol. 106, p. 131

Trigo I. F., Climatology and interannual variability of storm-tracks in the Euro-Atlantic sector: a comparison between ERA-40 and NCEP/NCAR reanalyses, *Climate Dynamics*, 2006, vol. 26, p. 127

Veiga J. A. P., Ambrizzi T., et al., A global and hemispherical analysis of the Lorenz energetics based on the representative concentration pathways used in CMIP5, *Advances in Meteorology*, 2013, vol. 2013

Veiga J. A. P., Pezza A. B., Simmonds I., Silva Dias P. L., An analysis of the environmental energetics associated with the transition of the first South Atlantic hurricane, *Geophysical Research Letters*, 2008, vol. 35

- Vera C. S., Vigliarolo P. K., Berbery E. H., Cold season synoptic-scale waves over subtropical South America, *Monthly Weather Review*, 2002, vol. 130, p. 684
- Vianna M., Menezes V., Pezza A., Simmonds I., Interactions between Hurricane *Catarina* (2004) and warm core rings in the South Atlantic Ocean, *Journal of Geophysical Research: Oceans*, 2010, vol. 115
- Vincent D., Chang L., Some further considerations concerning energy budgets of moving systems, *Tellus*, 1973, vol. 25, p. 224
- Virtanen P., Gommers R., Oliphant T. E., Haberland M., Reddy T., Cournapeau D., Burovski E., Peterson P., Weckesser W., Bright J., et al., SciPy 1.0: fundamental algorithms for scientific computing in Python, *Nature methods*, 2020, vol. 17, p. 261
- Wahab M. A., Bassett H. A., Lasheen A., On the mechanism of winter cyclogenesis in relation to vertical axis tilt, *Meteorology and Atmospheric Physics*, 2002, vol. 81, p. 103
- Walsh K., Tropical cyclones and climate change: unresolved issues, *Climate Research*, 2004, vol. 27, p. 77
- Walsh K. J., Camargo S. J., Knutson T. R., Kossin J., Lee T.-C., Murakami H., Patricola C., Tropical cyclones and climate change, *Tropical Cyclone Research and Review*, 2019, vol. 8, p. 240
- Walsh K. J., McBride J. L., Klotzbach P. J., Balachandran S., Camargo S. J., Holland G., Knutson T. R., Kossin J. P., Lee T.-c., Sobel A., et al., Tropical cyclones and climate change, *Wiley Interdisciplinary Reviews: Climate Change*, 2016, vol. 7, p. 65
- Wang D., Lin Y., Chavas D. R., Tropical cyclone potential size, *Journal of the Atmospheric Sciences*, 2022, vol. 79, p. 3001
- Weatherford C. L., Gray W. M., Typhoon structure as revealed by aircraft reconnaissance. Part I: Data analysis and climatology, *Monthly Weather Review*, 1988, vol. 116, p. 1032
- Whitaker J. S., Davis C. A., Cyclogenesis in a saturated environment, *Journal of the atmospheric sciences*, 1994, vol. 51, p. 889
- Whittaker L., Horn L., Northern Hemisphere extratropical cyclone activity for four mid-season months, *Journal of Climatology*, 1984, vol. 4, p. 297

Wiin-Nielsen A., A study of energy conversion and meridional circulation for the large-scale motion in the atmosphere, *Monthly Weather Review*, 1959, vol. 87, p. 319

Wiin-Nielsen A., Brown J. A., Drake M., On atmospheric energy conversions between the zonal flow and the eddies, *Tellus*, 1963, vol. 15, p. 261

Willoughby H. E., Marks F. D., Feinberg R. J., Stationary and moving convective bands in hurricanes, *Journal of the Atmospheric Sciences*, 1984, vol. 41, p. 3189

Wu M.-L. C., Reale O., Schubert S. D., Suarez M. J., Thorncroft C. D., African easterly jet: Barotropic instability, waves, and cyclogenesis, *Journal of Climate*, 2012, vol. 25, p. 1489

Yanai M., A detailed analysis of typhoon formation, *Journal of the Meteorological Society of Japan. Ser. II*, 1961, vol. 39, p. 187

Yanase W., Niino H., Hodges K., Kitabatake N., Parameter spaces of environmental fields responsible for cyclone development from tropics to extratropics, *Journal of Climate*, 2014, vol. 27, p. 652

Yano J.-I., Emanuel K., An improved model of the equatorial troposphere and its coupling with the stratosphere, *Journal of Atmospheric Sciences*, 1991, vol. 48, p. 377

Zehr R. M., , 1992 Technical Report 61 Tropical cyclogenesis in the western North Pacific. National Environmental Satellite, Data, and Information Service (NESDIS), NOAA USA

Appendix

Appendix A ---

título do apêndice 01

A.1 *subtítulo 01*

Appendix B _____

título do apêndice 02